Imperial College London
Department of Earth Science and Engineering

Numerical modelling of impact-generated seismic waves on Mars

Natalia Wójcicka

Supervised by: Prof. Gareth S. Collins and Dr Ian D. Bastow

Submitted in part fulfilment of the requirements for the degree of
Doctor of Philosophy in Planetary Science at Imperial College London.

December 2022

Declaration of Originality

I certify that all work presented in this thesis, other than where clearly stated and referenced, is entirely my own and was conducted throughout the duration of this PhD at Imperial College London. All results presented were interpreted jointly by me and my supervisors, Gareth Collins and Ian Bastow.

Natalia Wójcicka

Copyright Declaration

Abstract

Seismology is a powerful tool for understanding planetary interiors. On Earth, the seismicity is dominated by tectonic earthquakes, with the atmosphere protecting us from meteorite impacts. However, on Mars, impacts are one of the key processes generating seismic waves. Despite nominal pre-landing estimates of 1–3 impacts detected per Earth year, recognising impacts in the InSight seismic data has proven challenging. This thesis focuses on filling the current gaps in knowledge of impact-generated seismic waves, specifically in the context of the InSight mission, using numerical modelling.

Firstly, 13 small impacts onto martian regolith, forming craters 1–30 m, are simulated using iSALE-2D. Their seismic source properties are characterised in terms of impactor properties. In this size range scalar seismic moment increases almost linearly with impact momentum. Seismic efficiencies are $\sim 10^{-6}$, dependent on target material properties and impact velocity. The relatively low seismic efficiency and moment suggest that impact detectability on Mars is lower than previously assumed.

Secondly, a momentum-based amplitude-distance scaling relationship is derived based on a dataset containing the artificial impacts on the Moon, the Carancas impact on Earth, and impacts detected by InSight on Mars. Impacts producing craters <30 m in diameter are less detectable that pre-landing estimates suggested, whilst larger impacts are more detectable. A subset of marsquakes recorded by InSight is used to derive a new estimate of the impact rate on Mars to be $\sim$3–5 times higher than the estimates based on orbital observations, but consistent with crater chronology models.

Finally, a further suite of iSALE-2D simulations is used to record displacement seismograms generated by impacts and compute their power spectra. The frequency content of the signals decreases with increasing impactor size and velocity, and target porosity. The low-frequency content of seismic waves generated scales well with impactor momentum, but is also sensitive to target material properties.

Acknowledgements

Firstly, I would like to thank my wonderful supervisors Gareth Collins and Ian Bastow, for all the support and encouragement over the past four years, which helped to make this thesis a reality. Thank you for always making the time to discuss my research and providing endless advice. I would also like to thank Tom Davison for helping me solve many computational problems.

A big thank you to the members of the InSight Science team and especially the Impacts Theme Group, for discussions that helped guide the contents of this thesis. I would like to especially thank Ben Fernando, Andrea Rajšić and Géraldine Zenhäusern for many fruitful collaborations and discussions, but also for the numerous ECR coffee breaks. Thank you to all my friends, both at Imperial and outside, especially Zsófia and Sarah, for the numerous coffee and lunch chats, that got me through the long days in the office. I also want to thank my oldest friend Mia, for always being there for me.

A special thank you to Michał, for being the best partner I could have hoped for. All your love, support and delicious home-cooked dinners kept me sane throughout this journey. The past four years have been a roller-coaster and I could not have done it without you.

A massive thank you to my parents and my brother for being by my side and always supporting me in pursuing my passions. Finally, a special thank you to our family dog, Fela, who sadly passed away during the final stages of my PhD. You have given us so much love over the 11 years you were with us and you will be greatly missed.

Thank you.

Contents

List of Figures

List of Tables

List of Symbols

M_0	Seismic scalar moment
$\mathbf{M}$	Seismic moment tensor
M_W	Seismic moment magnitude
k_s	Seismic efficiency
t_c	Duration of contact and compression stage of the impact process
τ	Seismic source duration
d_i	Impactor diameter
v_i	Impactor velocity
δ	Impactor density
D	Crater diameter
π_2	Gravity-scaled impactor size
π_3	The strength group
π_4	Ratio of target and projectile densities
π_V	Cratering efficiency
π_D	Scaled crater diameter
ϕ	Displacement potential
D_1	Residual radial displacement
K	Bulk modulus
G	Shear modulus
γ	Spericity of source
S	Ejecta amplification factor

p_i	Impactor momentum
p_z	Momentum transferred to target during impact
E_s	Seismic energy
E_i	Impactor's kinetic energy
c_B	Bulk sound speed
c_P	P-wave speed
c_S	S-wave speed
c	Seismic moment correction factor
f_c	Corner frequency
v_{max}	Peak P-wave amplitude

List of Abbreviations

InSight Interior Exploration using Seismic Investigations Geodesy and Heat Transport

MQS Marsquake Service

LMST Local Mean Solar Time

SEIS Seismic Experiment for Internal Structure

VBB Very Broad Band

SP Short Period

LF Low Frequency

BB Broadband

HF High Frequency

VF Very High Frequency

HP^3 Heat flow and Physical Properties Package

MRO Mars Reconnaissance Orbiter

CTX MRO Context Camera

MARCI Mars Color Imager

HiRISE High Resolution Imaging Experiment

iSALE impact-Simplified Arbitrary Lagrangian Eulerian

CPPR cells per projectile radius

EoS Equation of State

Chapter 1

Introduction

1.1 Motivation and Aims

Meteorite impact is one of the most common processes in the Solar System, which over time shapes the morphology of planetary surfaces. During crater formation, there are several other processes taking place that are not immediately visible to the eye. One of those processes is the generation of strong shock waves, which eventually decay into seismic (elastic) waves. These signals can be detected by seismometers at large distances, as shown previously on the Moon (McGarr et al., 1969), or even felt by people nearby, as was the case following the Carancas impact in Peru (Brown et al., 2008; Le Pichon et al., 2008; Tancredi et al., 2009). Therefore, while they can present a hazard, meteorite impacts recorded seismically provide a unique opportunity to expand our understanding of celestial bodies' interiors.

Our understanding of the Earth's internal structure has been established primarily by studying seismograms from many seismic stations. Central to such analyses is accurate knowledge of an earthquake's location, which is achieved relatively easily in instances where there are multiple seismograph stations. On other planets, without a working seismograph network, locating seismic sources accurately has proven more difficult. An impact-generated signal can provide a very well localised source location because it produces a visible crater on a planet's surface. Impacts are therefore particularly valuable in planetary seismology.

At the time of writing, the InSight lander is the only active seismic station on Mars. It has been recording seismic signals since early 2019 and to date it has recorded over a thousand marsquakes. However, unambiguously identifying impact-generated signals has proven more challenging than previously expected. During the first 2 years of operations, no impacts were identified in the seismic data, which can be partially attributed to lack of understanding of how impact properties influence the seismic signals generated. Further modelling work was therefore needed to address this issue. In the final year of the InSight's operations, five local impacts were detected (Garcia et al., 2022). The signals were identified by a frequency-dependent 'chirp' following the main seismic arrival, attributed to an atmospheric wave generated during the impact. This part of the signal also aided the location of corresponding impact craters. Two very large (D>100 m) distant impacts were also detected both seismically and orbitally (Posiolova et al., 2022), offering a unique opportunity to test and refine existing models.

Two key seismic source parameters of interest are seismic moment and seismic efficiency. Seismic moment is a measure of the 'size' of a seismic event, and can be related to seismic amplitudes (Aki and Richards, 2002). It is one of the most useful concepts in seismology for comparing earthquakes and developing seismic magnitude scales, and is used extensively in the process of cataloguing seismic events detected by InSight (Böse et al., 2021). It is, however, poorly constrained for impacts. Teanby and Wookey (2011) proposed that seismic moment scales as a power law with impact energy. Other previous studies have proposed that seismic moment is directly proportional to impact momentum (Lognonné et al., 2009; Gudkova et al., 2011; Gudkova et al., 2015), suggesting it should scale easily with crater diameter. However, that relationship has not been well defined. Such a relationship would aid searches for both an impact crater corresponding to a suspected impact event recorded by InSight, and for an seismic event corresponding to a newly-discovered crater.

Seismic efficiency, defined here as the proportion of energy converted from the impactor's kinetic energy into seismic waves, has been studied in more detail than seismic moment in various impact and explosion experiments (e.g: Latham et al., 1970a; McGarr et al., 1969; Richardson and Kedar, 2013; Güldemeister and Wünnemann, 2017). The resulting values of seismic efficiency range from 10^{-6} for artificial planetary impacts (Latham et al., 1970a), to 10^{-1} for

underground nuclear explosions (Patton and Walter, 1993), with no clear indication of dependence on specific impactor or target properties. More recently, the InSight team attempted to record seismically the impacts of balance masses released during the landing of Mars2020 (Fernando et al., 2021a). Whilst the landing was not detected, the experiment placed an upper limit on the seismic efficiency of Martian regolith, consistent with previous experiments (Fernando et al., 2021b). It is unclear how seismic efficiency scales with crater size, but it is thought to vary considerably with target material properties (Güldemeister and Wünnemann, 2017), making it more difficult to use in the context of InSight, where subsurface properties may not be well known. Whilst seismic efficiency is a more intuitive concept in the context of the impact process, it is difficult to relate to seismic source parameters and hence to compare to other seismic events.

Another issue is the scarcity of impact data available. Laboratory impact experiments in unconsolidated sand were conducted on a much smaller scale than natural impacts (e.g., Richardson and Kedar, 2013; Yasui et al., 2015), which makes them difficult to apply to scenarios expected on Mars. The cohesionless target material used in these experiments is more representative of a lunar surface, than the martian regolith. Documentation of natural impacts observed seismically on the Moon and Earth is limited (Brown et al., 2008), and in most cases the initial conditions, such as impactor velocity, angle and mass, are unknown, obscuring the true influence of these parameters on the seismic signal. Artificial impacts on the Moon and Mars (Latham et al., 1970a; Fernando et al., 2021a) provide an alternative approach, where the impact conditions are well known. However, the impactors are usually metal objects, poor analogs for natural meteorites.

Numerical modelling experiments provide another means to investigate impact-generated seismic waves for impact scenarios relevant for InSight. Wünnemann et al. (2016) used laboratory impact experiments in quartz sand to validate the numerical models performed in iSALE2D, specifically in terms of ejecta distributions. Güldemeister and Wünnemann (2017) showed that iSALE2D simulations can be used to calculate seismic efficiency and quality factors for impacts onto several porous and non-porous targets. They showed that seismic efficiency for quartzite and sandstone targets is of the order of 10^{-3} and is sensitive to target material poros-

ity. Presence of water inside pores significantly decreased the seismic efficiency of the impact also resulting in much smaller seismic magnitudes. Chapter 3 of this thesis aims to fill the gaps in current knowledge using numerical modelling of the shock wave generation and decay for impact scenarios most relevant for InSight. The modelling results are used to better constrain the relationships between seismic source parameters and impact properties.

Seismic detection of meteorite impacts is also crucial to constraining the impact rate on the Mars. This is especially relevant to the wider planetary science community, since impact rates are often used to determine ages of planetary surfaces (Neukum et al., 2001). They are also important when considering risks from impact-generated seismic waves to future crewed space missions. Specifically on Mars, theoretically predicted impact rates (Hartmann, 2005) are consistently higher than those determined from repeated orbital imaging (Malin et al., 2006; Daubar et al., 2013). Seismology provides an alternative means of impact detection, and can be used to better understand current crater production rates by eliminating detection biases in orbital imagery as well as the uncertainty resulting from extrapolation of chronology models. A major goal of this thesis aims to help constrain the seismic detectability of impacts on Mars and the impact rate on its surface implied by events detected by InSight (Chapter 4).

A key property used to differentiate seismic signals generated by different sources is the frequency content. It largely depends on the geometry of the source but is also affected by the material properties along the waves travel path. The frequency content of impact-generated waves has been studied using natural impacts detected on the Moon (Gudkova et al., 2011; Gudkova et al., 2015), where it was found to be sensitive to the target material properties at the impact site. More recently, Schmerr et al. (2019) concluded that crater clusters are likely to produce higher frequency seismic waves than single crater-events, suggesting that the frequency content is linked to impactor size, although its dependence on other impact parameters is unclear. This is addressed in Chapter 5 of this thesis.

In summary, this thesis aims to fill the gaps in the current understanding of impacts as seismic sources and their implications for impact detectability and rate on the surface of Mars, specifically in the context of impact scenarios relevant to the InSight mission. The key research

questions addressed in this thesis are:

- What is the relationship between impact parameters and seismic moment?
- What is the relationship between impact parameters and seismic efficiency?
- What is the detectability of small impacts on Mars in the context of InSight?
- What do events detected by InSight imply about the impact rate on Mars?
- How does the frequency content of seismic waves vary for different impact scenarios?

1.2 Thesis Outline

This thesis is structured in 6 Chapters, as follows:

- Chapter 2 presents a literature review of meteorite impacts as seismic sources and a description of impact cratering process. It also introduces to the InSight mission and its goals, predictions and results to date.
- Chapter 3 focuses on constraining seismic source properties of small impacts onto martian regolith and their dependence on impact parameters. The main parameters studied are seismic moment, seismic efficiency and source time function. The results of this chapter are used to update seismic detectability estimates of impacts by InSight.
- Chapter 4, discusses the application of the modelling described in the previous chapter to recently discovered impacts on the surface of Mars. Semi-empirical scaling relationships for predicting seismic amplitudes generated by impacts are derived and used to update the seismic detectability estimates. Finally, an estimate of impact rate on Mars is derived from a subset of seismic events detected by InSight with similar properties.
- Chapter 5 uses an alternative simulation setup to calculate the near field seismograms for a number of impact scenarios. These seismograms are used to constrain the signal's frequency content as a function of impact properties.

- Chapter 6 summarises the key findings of this thesis and describes potential future work.

1.3 Statement of Originality and Contribution

The work presented this thesis was completed during my PhD at Imperial College London. Everything included in this thesis is entirely my own, except where clearly stated or referenced. Large parts of the work presented in Chapters 3 and 4 have been published in a peer-reviewed journal. All numerical iSALE-2D simulations were performed by me. Prof. Gareth Collins conducted atmospheric entry models to guide input conditions. The post-processing scripts used to analyse and generate figures in this thesis were written by me. A large part of Chapter 4 contains work currently in preparation for publication in a peer-reviewed journal, in collaboration with members of the InSight Science Team: Géraldine Zenhäusern, Dr Simon C. Stähler and Dr Ingrid Daubar. All results presented in this thesis were interpreted jointly by me and my supervisors Prof. Gareth Collins and Dr Ian Bastow.

1.4 Publications

First author papers:

- **Wójcicka, N.**, Collins, G. S., Bastow, I. D., Teanby, N. A., Miljković, K., Rajšić, A., Daubar, I., & Lognonné, P. (2020). The Seismic Moment and Seismic Efficiency of Small Impacts on Mars. *Journal of Geophysical Research: Planets*, **125**(10). `https://doi.org/10.1029/2020JE006540`

Contributed papers:

- Garcia, R. F., Daubar, I. J., Beucler, É., Posiolova, L. V., Collins, G. S., Lognonné, P., Rolland, L., Xu, Z., **Wójcicka, N.**, Spiga, A., Fernando, B., Speth, G., Martire, L.,

Rajšić, A., Miljković, K., Sansom, E. K., Charalambous, C., Ceylan, S., Menina, S., ... Banerdt, W. B. (2022). Newly formed craters on Mars located using seismic and acoustic wave data from InSight. *Nature Geoscience*, **10**(11), 1–7. https://doi.org/10.1038/s41561-022-01014-0

- Rajšić, A., Miljković, K., **Wójcicka, N.**, Collins, G. S., Onodera, K., Kawamura, T., Lognonné, P., Wieczorek, M. A., & Daubar, I. J. (2021). Numerical Simulations of the Apollo S-IVB Artificial Impacts on the Moon. *Earth and Space Science*, **8**(12), e2021EA001887. https://doi.org/10.1029/2021EA001887

- Fernando, B., **Wójcicka, N.**, Maguire, R., Stähler, S. C., Stott, A. E., Ceylan, S., Charalambous, C., Clinton, J., Collins, G. S., Dahmen, N., Froment, M., Golombek, M., Horleston, A., Karatekin, O., Kawamura, T., Larmat, C., Nissen-Meyer, T., Patel, M. R., Plasman, M., ... Daubar, I. J. (2021). Seismic constraints from a Mars impact experiment using InSight and Perseverance. *Nature Astronomy*, **1**–**6**. https://doi.org/10.1038/s41550-021-01502-0

- Fernando, B., **Wójcicka, N.**, Han, Z., Stott, A., Ceylan, S., Charalambous, C., Collins, G. S., Estèvez, D., Froment, M., Golombek, M., Gülzow, P., Horleston, A., Karatekin, O., Kawamura, T., Larmat, C., Maguire, R., Nissen-Meyer, T., Plasman, M., Qia, Y., ... Daubar, I. J. (2021). Questions to Heaven. *Astronomy & Geophysics*, **62**(6), 22-25. https://doi.org/10.1093/astrogeo/atab103

- Fernando, B., **Wójcicka, N.**, Froment, M., Maguire, R., Stähler, S. C., Rolland, L., Collins, G. S., Karatekin, O., Larmat, C., Sansom, E. K., Teanby, N. A., Spiga, A., Karakostas, F., Leng, K., Nissen-Meyer, T., Kawamura, T., Giardini, D., Lognonné, P., Banerdt, B., & Daubar, I. J. (2021). Listening for the Landing: Seismic Detections of Perseverance's Arrival at Mars With InSight. *Earth and Space Science*, **8**(4). https://doi.org/10.1029/2020ea001585

- Rajšić, A., Miljković, K., Collins, G. S., Wünnemann, K., Daubar, I. J., **Wójcicka, N.**, & Wieczorek, M. A. (2021). Seismic Efficiency for Simple Crater Formation in the

Martian Top Crust Analog. *Journal of Geophysical Research: Planets*, **126**(2). https://doi.org/10.1029/2020JE006662

- Daubar, I. J., Lognonné, P., Teanby, N. A., Collins, G. S., Clinton, J., Stähler, S., Spiga, A., Karakostas, F., Ceylan, S., Malin, M., McEwen, A. S., Maguire, R., Charalambous, C., Onodera, K., Lucas, A., Rolland, L., Vaubaillon, J., Kawamura, T., Böse, M., Horleston, A., van Driel, M., Stevanović, J., Miljković, K., Fernando, B., Huang, Q., Giardini, D., Larmat, C. S., Leng, K., Rajšić, A., Schmerr, N., **Wójcicka, N.**, Pike, T., Wookey, J., Rodriguez, S., Garcia, R., Banks, M. E., Margerin, L., Posiolova, L., Banerdt, B. (2020). A New Crater Near InSight: Implications for Seismic Impact Detectability on Mars. *Journal of Geophysical Research: Planets*, **125**(8). https://doi.org/10.1029/2020JE006382

First author conference abstracts:

- **Wójcicka, N.**, Collins, G. S., Bastow, I. D., Teanby, N. A., Miljković, K., & Rajšić, A. (2022) Frequency Content of Impact-generated Seismic Waves. *53rd Lunar and Planetary Science Conference 2022*, (LPI Contrib. No. 2678), Abstract 2237.

- **Wójcicka, N.**, Collins, G. S., Bastow, I. D., Miljković, K., & Rajšić, A. (2021) Seismic Source Time Function and Frequency Content of Impact-Generated Seismic Waves. *Lunar and Planetary Science Conference 2021*, (LPI Contrib. No. 2548), Abstract 2134.

- **Wójcicka, N.**, Collins, G. S., Bastow, I. D., Teanby, N. A., Miljković, K., Rajšić, A., Daubar, I., Lognonné, P. H. (2020) The seismic moment and seismic efficiency of small impacts on Mars. *AGU Fall Meeting*.

- **Wójcicka, N.**, Collins, G. S., Bastow, I., Teanby, N. A., Miljković, K., Rajšić, A. (2020) Seismic Moment and Efficiency of Small Impacts on Mars. *2nd British Planetary Science Conference.*

- **Wójcicka, N.**, Collins, G. S., Bastow, I. (2019) Seismic efficiency and scalar seismic

moment of metre-scale impacts on Mars. *British Geophysical Association Postgraduate Research in Progress.*

- **Wójcicka, N.**, Collins, G. S., Bastow, I., Miljković, K., Teanby, N. A., Karakostas, F., & Lognonné, P. (2019) Investigating the Relationship Between the Seismic Efficiency and Seismic Moment and Impactor Properties on Mars. *50th Lunar and Planetary Science Conference 2019* (LPI Contrib. No. 2132), Abstract 2633.

Chapter 2

Background and Theory

This chapter presents theory concerning the impact process and the measures used to characterise impacts as seismic sources. The InSight mission is also introduced including its goals and instruments, which recorded the first impact-generated seismic signals on Mars.

2.1 Impact cratering processes

Crater formation is a continuous process, which can be nominally divided into three main stages: contact and compression, excavation and modification (Melosh, 1989). Whilst it is difficult to clearly define the end of one stage and beginning of the next, this division is useful for understanding the many different physical processes occurring during an impact. This section summarises briefly the three main stages of crater formation.

2.1.1 Contact and compression

As the impactor strikes the surface at high speed, a supersonic compression wave (a shock wave) is sent through both the target and impactor, causing pressure and temperature to rise sharply. These changes are localised to a small volume near the impact point. The behaviour on either side of the shock front, defined as the advancing edge of the shock wave, is governed

by the Hugoniot continuity equations. As the impactor penetrates the target, it is decelerated, causing the target material to be accelerated. A small amount of material is forced out from the interface between the impactor and target in a process called jetting. During this stage a large portion of the impactor's kinetic energy and momentum is transferred to the target. Once the shock wave reaches the back of the impactor, a rarefaction (release) wave travels back down to the target, followed by decompression of the material. The contact and compression stage ends once the high pressures diminish.

The duration of the contact and compression stage depends on several impact properties: impactor size, materials involved and impact velocity, hence it is difficult to precisely define. It can be approximated as the time the shock wave takes to travel to twice the diameter of the projectile $\tau = 2d_i/U$, where d_i is the impactor diameter and U the shock velocity. Typically this stage last a short time, of the order of $10^{-5} - 10^{-4}$ s for sub-metre-scale impacts, most relevant for this work.

2.1.1.1 Shock wave propagation and decay

As the shock wave propagates further away from the impact location, its velocity decays to subsonic values. The amplitude of the wave also continues to drop as it spreads away from the impact point. The wave then decays into a plastic and eventually an elastic wave. The plastic wave, travelling much slower than the shock and elastic waves, permanently deforms the target material and its kinetic energy diminishes rapidly. On the other hand, once it decays into an elastic wave, it does not cause permanent deformation in the target and conserves kinetic energy (in a perfectly elastic medium). The elastic wave is what continues to propagate across large distances as a seismic wave. From this point onward, its amplitude is diminished by geometric spreading and attenuation.

2.1.2 Excavation stage

The waves generated during the previous stage cause the material underneath and around the impact point to start moving, producing an 'excavation flow' of material. Material is forced out

of the crater becoming ejecta. The material deeper under the pre-impact surface is compressed and displaced in an outward direction.

The further compression and ejection of material from the crater results in formation of a bowl-shaped "transient crater". Its depth is the maximum depth achieved during the crater formation process, before it undergoes collapse and modification. When the excavation flow has stopped and this maximum depth has been reached, then the excavation stage ends. In large craters this is caused by the force of gravity, whilst in smaller craters by the strength of the target material. This stage lasts much longer than the contact and compression stage, of the order of seconds of even minutes for the largest impactors.

2.1.3 Modification stage

The final stage of crater formation begins when the transient crater has been formed. Depending on the size of the transient crater, the final shape of the crater varies.

For small transient craters, peaks formed by ejecta around the rim as well as the sides of the crater collapse due to gravity, sliding down to the floor of the crater. This results in a bowl-shaped, 'simple crater'. The floor of these crater is often covered in a breccia lens and loose debris. The depth to diameter ratio of simple craters ranges from 1:5 to 1:3 (Melosh, 1989). For large transient craters, the modification stage results in a 'complex crater'. The material below the transient crater rises, producing a central uplift. The following collapse of the crater rim and, in the largest craters the central peak itself, forms a wreath of terraces or a peak ring. Complex craters are characterised by a significantly smaller depth to diameter ratio than simple craters.

The duration of the modification stage is linked to the transient crater size, lasting up to several minutes for the largest craters.

2.2 Impact crater scaling relationships

The final size and shape of an impact crater are determined by a combination of impactor and target material properties as well as physical impact parameters such as impactor's speed and mass. A number of empirical scaling relationships exist to aid the process of predicting the impact crater properties for known impact scenarios.

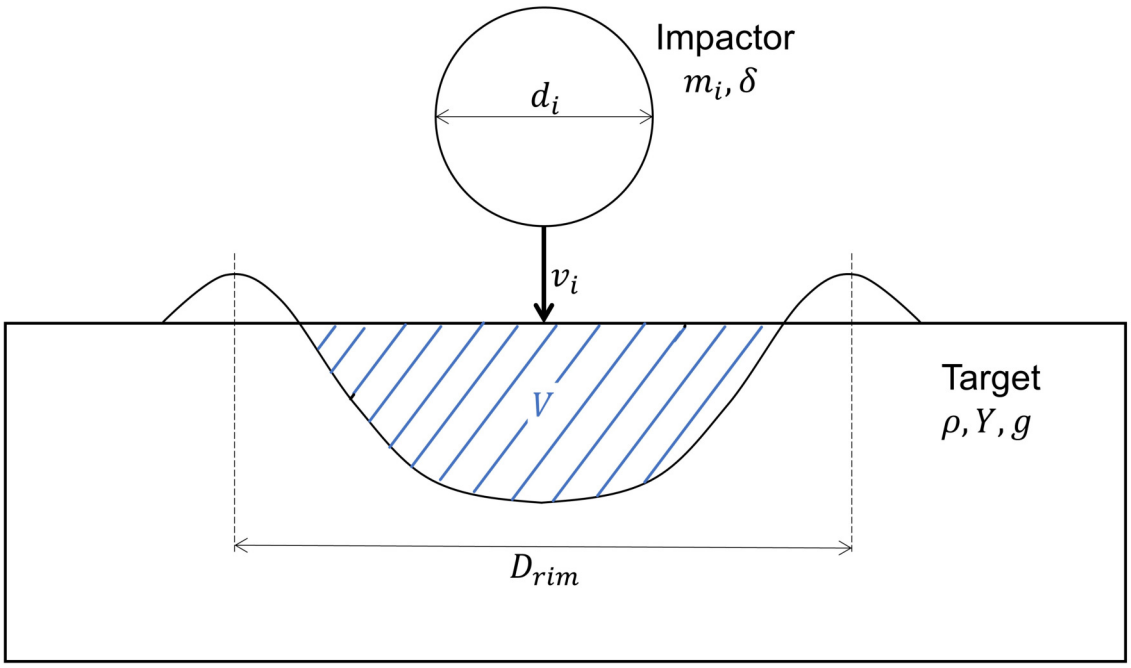

Figure 2.1: An illustration of an impact scenario of an impactor of diameter d_i, mass m_i and density δ striking the target of strength Y and density ρ, at velocity v_i and under gravity g, as used in π-group scaling. The resulting crater of diameter D_{rim} is produced when a volume V of target material has been excavated.

A widely used approach describes the cratering process using a number of dimensionless π-scaling parameters (Holsapple, 1993). When considering a generic impact scenario (see Fig. 2.1), where an impactor of diameter d_i, mass m and density δ strikes a target of density ρ at vertical impact velocity v_i, there are three key dimensionless parameters that describe the impact cratering process:

- the 'gravity-scaled impactor size':

$$\pi_2 = \frac{g d_i}{v_i^2}, \tag{2.1}$$

- the 'strength group':

$$\pi_3 = \frac{Y}{\rho v_i^2}, \tag{2.2}$$

- and the ratio of target and projectile densities:

$$\pi_4 = \frac{\rho}{\delta}. \tag{2.3}$$

Experimental studies often report the volume (V in Fig. 2.1) excavated during an impact. Therefore, a ratio between the mass displaced from the crater and the mass of the impactor, often referred to as cratering efficiency, can be defined as:

$$\pi_V = \frac{\rho V}{m}. \tag{2.4}$$

For the example impact scenario shown in Fig. 2.1, the scaled crater rim diameter (π_D, related to the absolute crater rim radius D_{rim}) can be computed as:

$$\pi_D = \left(\frac{\rho}{m}\right)^{1/3} D_{rim} = 1.3 \times 2K_1 \left[\pi_2 \pi_4^{\frac{6\nu-2-\mu}{3\mu}} + \left[K_2 \pi_3 \pi_4^{\frac{6\nu-2}{3\mu}}\right]^{\frac{2+\mu}{2}}\right]^{\frac{-\mu}{2+\mu}}, \tag{2.5}$$

where K_1, K_2, μ and ν are empirically determined constants. A factor of 1.3 is added to convert the crater diameter from pre-impact level to crater rim level (Holsapple, 1993).

For small (metre-scale) impacts, the strength of the target is large compared to the gravity of excavated material ($\pi_3 >> \pi_2$). The gravity-scaled size can hence be neglected when determining the crater size. This defines the 'strength regime' of crater formation (blue region in Fig. 2.2). In this regime the crater size is independent of π_2 and is instead determined by π_3 and π_4. Equation 2.5 becomes:

$$\pi_{D,strength} = \left(\frac{\rho}{m}\right)^{1/3} D_{rim} = 1.3 \times 2K_1 \left[K_2 \pi_3 \pi_4^{\frac{6\nu-2}{3\mu}}\right]^{\frac{-\mu}{2}}. \tag{2.6}$$

On the other hand for large impacts, the gravity effect is larger than the strength of the target material ($\pi_2 >> \pi_3$). This defines the 'gravity regime' or crater formation (the orange region in Fig. 2.2). In this regime the crater diameter is determined by π_2 and π_4 and equation 2.5 becomes:

$$\pi_{D,gravity} = \left(\frac{\rho}{m}\right)^{1/3} D_{rim} = 1.3 \times 2K_1 \left[\pi_2 \pi_4^{\frac{6\nu-2-\mu}{3\mu}}\right]^{\frac{-\mu}{2+\mu}}. \tag{2.7}$$

The transition between the gravity and strength regime occurs when the gravitational and cohesive forces are of the same order of magnitude, i.e. when $Y \sim g\rho d_i$ (grey region in Fig. 2.2).

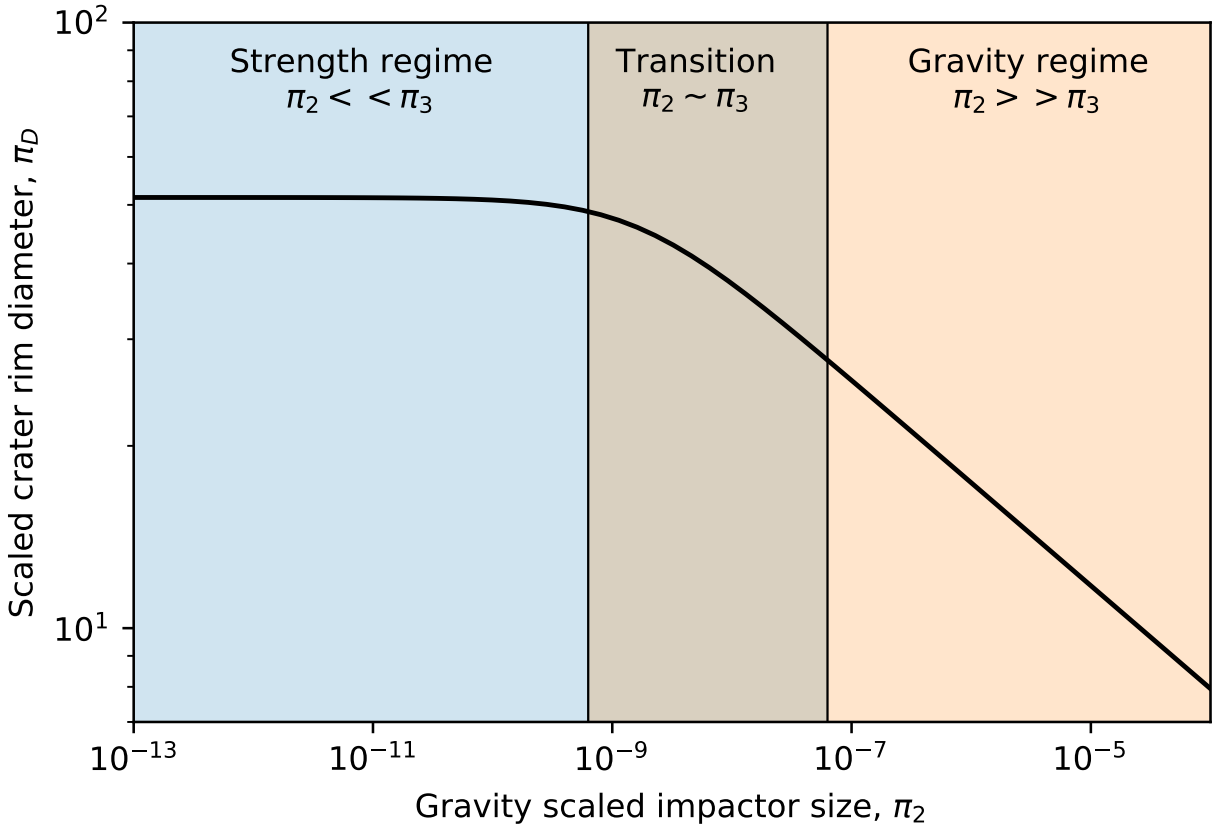

Figure 2.2: The scaled crater diameter π_D as a function of gravity scaled impactor size π_2, for a range of impactor sizes striking target at vertical velocity of 10 kms^{-1}. For small impactors, the resulting crater size is independent of the gravity scaled impactor size, which indicates the strength regime of crater formation. For large impacts, the weight of excavated material during crater formation reduces the crater size as a power law of the gravity scaled size (Holsapple, 1993).

2.3 Impacts as seismic sources

As described in the previous sections, the impact cratering process involves large amounts of energy being transferred into the target material. A portion of that energy is radiated away in the form of seismic waves, which can be detected using seismometers. The characteristics of these waves vary with impact conditions and constraining this dependence forms a large part of this thesis.

This section introduces three key parameters used to characterise seismic waves generated by impacts: seismic moment, seismic efficiency and source time function.

2.3.1 Seismic moment, M

Seismic moment, **M**, is one of the key parameters used to characterise seismic events. **M** is a tensor used in seismology to describe the geometry and magnitude of forces acting at the seismic source. The tensor consists of 9 elements: three force dipoles (the diagonal components) and six force couples (the off-diagonal components) and can be expressed as follows:

$$\boldsymbol{M} = \begin{pmatrix} M_{11} & M_{12} & M_{13} \\ M_{21} & M_{22} & M_{23} \\ M_{31} & M_{32} & M_{33} \end{pmatrix} \tag{2.8}$$

The form of the seismic moment tensor describes the seismic source mechanism, whilst the magnitude of the tensor (seismic scalar moment) provides information on the 'size' of the seismic event. The seismic magnitude, M_W is defined as a function of seismic scalar moment M_0 as follows:

$$M_W = \frac{2}{3}(\log(M_0) - 9.1) \tag{2.9}$$

and serves as a simple way of comparing the amount of work done during the ground motions at a seismic source (Hanks and Kanamori, 1979). A separate magnitude scale has been recently

developed for Mars using the marsquake data collected by InSight (Böse et al., 2021).

The following subsections explore the different interpretations of seismic moment of impacts.

2.3.1.1 Seismic moment of a buried explosion

A common approximation for explosions and impacts is a point source mechanism. In this case, the force couples can be neglected the moment tensor consists of the three mutually perpendicular force dipoles acting in opposing directions parallel to the dipole (Müller, 1973).

An explosive point source in an unbounded medium can be defined in terms of its displacement potential:

$$\phi(R,t) = \frac{F(t - R/c_P)}{R}, \tag{2.10}$$

where c_P is the P-wave speed, R is the (spherical) radial distance from the source, t is time after the explosion and $F(t)$ is the reduced displacement potential (Müller, 1973; Shishkin, 2007; Haskell, 1967). An equivalent radiation of seismic waves by three dipoles occurs if their moment function is:

$$M_e(t) = -4\pi\rho c_P^2 F(t), \tag{2.11}$$

where ρ is the target density. The final value of this dipole moment function, $M_e(t)$, defines the scalar moment of the explosion M_1 (Müller, 1973; Shishkin, 2007):

$$M_1 = M_e(\infty) = -4\pi\rho c_P^2 F(\infty). \tag{2.12}$$

M_1 can be defined in terms of the average residual radial displacement $\langle D_1 \rangle = -\langle F(\infty) \rangle / R_1^2$ at any distance $R_1 \geq R_e$, where R_e is the elastic radius at which plastic deformation stops and linear elasticity laws begin to hold. Taking S_1 as the surface area of a sphere of radius R_1 surrounding the explosion, M_1 can be expressed in term of S_1, D_1 and the elastic moduli of the target:

$$M_1 = \rho c_P^2 S_1 \langle D_1 \rangle = \left(K + \frac{4G}{3} \right) S_1 \langle D_1 \rangle , \tag{2.13}$$

where K and G are the bulk and shear modulus of the target material, respectively. This implies that the seismic moment is proportional to the displaced volume $V_1 = S_1 \langle D_1 \rangle$ (Shishkin, 2007).

Considering stress as a function of radius from a buried explosion also allows the seismic moment to be defined in terms of the shear strength of the deformed ground σ_s and the volume of fractured (or plastically deformed) material $V_f = 4\pi R_e^3/3$ (Shishkin, 2007):

$$M_1 = \frac{4\pi}{3} R_e^3 \sigma_s \left(\frac{c_P}{c_S} \right)^2, \tag{2.14}$$

where c_S is the S-wave speed. Equivalence between these definitions implies the following relationship between the residual displacement at the elastic limit and the ratio of shear strength to shear modulus:

$$\frac{\langle D_e \rangle}{R_e} \approx \frac{\sigma_s}{3G}. \tag{2.15}$$

The radiated seismic energy from a buried explosion E_s can be defined in a similar manner (Haskell, 1967) and expressed as a function of the work done to overcome the strength forces to produce the displaced volume:

$$E_s = b \sigma_s S_1 \langle D_1 \rangle, \tag{2.16}$$

where b is a constant that depends on the target material (Shishkin, 2007). Comparison of this equation with equation 2.13 leads to:

$$\frac{E_s}{M_1} = c \frac{\sigma_s}{G}, \tag{2.17}$$

where c is another material-dependent constant that is also expected to depend on the source mechanism.

2.3.1.2 Seismic moment of an impact

An impact differs from an explosion, as considered by Müller (1973), in that it occurs at the free-surface boundary of a half-space and is therefore spherically asymmetric (Shishkin, 2007). However, by analogy with a buried explosion the seismic moment of an impact should still

depend on both the displaced volume (beyond the elastic limit), according to equation 2.13, and the volume of permanently deformed material, according to equation 2.14, provided the average R_e, and the surface area S_1 and the average residual displacement $\langle D_1 \rangle$ at this limit, are defined appropriately.

Walker (2003) presented an alternative definition for the seismic moment of a vertical impact: a force couple tensor, with the terms of the tensor given by a force multiplied by the couple distance. For an axially-symmetric wave, the horizontal force couple at the wave front is proportional to the change in horizontal momentum across the wave divided by the time of arrival (force) times the cylindrical wave-front radius r (distance). This implies that the horizontal moment should be approximately proportional to the horizontal momentum transfer times the wave speed. While this force couple can be defined for the two horizontal directions within the target, the presence of the free surface implies a vertical component for the moment cannot be defined similarly because the downward component of momentum is not balanced in the other direction as a force couple. Instead, Walker (2003) showed that by analogy with a spherically symmetric explosion, the horizontal seismic moment components $M_{rr} + M_{\theta\theta}$ can be defined as:

$$M_{rr} + M_{\theta\theta} = \frac{1}{t} \int \rho v_r r \mathrm{d}V, \tag{2.18}$$

where v_r is the particle velocity in the radial (cylindrical geometry) direction, r is the (cylindrical) radial distance from the symmetry axis and t is time since the impact. For a spherically-symmetric explosion, the vertical moment M_{zz} can be defined similarly and the scalar moment $M_1 = M_{zz} = (M_{rr} + M_{\theta\theta})/2$, implying:

$$M_1 = \frac{1}{2}\frac{1}{t} \int \rho v_r r \mathrm{d}V. \tag{2.19}$$

Although there is no net horizontal momentum transferred in a vertical impact, owing to axial symmetry, horizontal motion is still imparted to the target. Walker (2003) also showed that in the absence of a definable vertical seismic moment M_{zz} for an impact, the sphericity (isotropy)

of loading could be measured by the term:

$$\gamma = \frac{M_{rr} + M_{\theta\theta}}{2p_z c_P}, \tag{2.20}$$

where p_z is the vertical momentum transferred to the target. A sphericity of loading $\gamma > 1$, which Walker (2003) considers typical for impact loading, implies that more force is delivered in the outward, radial direction than is delivered vertically.

Assuming an impact-generated signal is similar to one generated by a point force density, Gudkova et al. (2015) proposed the vertical component of the seismic moment $M_{zz} = p_z c_P$, as another definition of the seismic moment of an impact. Extending the approach of Lognonné et al. (2009) and Gudkova et al. (2011) of defining the impact seismic source-time function, this model relates seismic scalar moment to impactor momentum via:

$$M_1 = S p_i c_P, \tag{2.21}$$

where p_i is impactor momentum and S is an amplification factor to account for additional momentum imparted to the target by ejecta-debris expelled from the growing crater. S depends on impact velocity as: $S = 1 + \eta(v/\ 1\ \mathrm{km/s})^{0.22}$. For a vertical impact, Sp_i is essentially the vertical momentum, p_z, transferred to the target during impact:

$$p_z = \int_{V_t} \rho v_z \mathrm{d}V, \tag{2.22}$$

where ρ is target density, v_z is vertical material velocity due to impact. V_t is the integration volume representing the target that is not ejected.

2.3.2 Seismic efficiency, k_s

Another parameter often used to characterise the seismic properties of an impact is the seismic efficiency. Seismic efficiency k_s is defined as the portion of impactor's kinetic energy E_i that is converted into seismic (elastic) wave energy E_s:

$$k_s = \frac{E_s}{E_i}. \tag{2.23}$$

During the impact process only a small portion is converted into seismic waves, with the majority of initial kinetic energy going into heat and excavation of the crater. In the case of numerical experiments, the total energy of a wave can be calculated by computing the kinetic energy of the material inside the wave region (of density ρ, moving at speed v), defined as the region of high pressure behind the wave front. This can be written as follows:

$$E_s = \frac{1}{2} \int \rho v^2 dV. \tag{2.24}$$

A popular approximation for the energy, E_s, radiated as seismic waves from an impact (Schultz and Gault, 1975; Güldemeister and Wünnemann, 2017) assumes the seismic wave is symmetric across a hemispherical shell and calculates the seismic energy by integrating the power transferred to the target at radius R in the elastic domain over the duration of the wave pulse (Rinehart, 1960). Assuming a triangular wave pulse of pressure amplitude $P_{\max}$ and half-width Δt, E_s can be defined as:

$$E_s = \frac{P_{\max}^2 \pi R^2 \Delta t}{3\rho c_P}, \tag{2.25}$$

where c_P is the P-wave speed.

Data compiled from numerical simulations of impacts (Güldemeister and Wünnemann, 2017), laboratory experiments (Richardson and Kedar, 2013), underground explosions and artificial planetary impacts (Latham et al., 1970a; Latham et al., 1970b), produced a range of values for k_s spanning 6 orders of magnitude between $10^{-7} - 10^{-1}$ (Fig. 2.3). The main differences between the seismic efficiency values arise from the different materials involved. Weaker, more

porous target materials produce generally lower values of k_s than stronger, non-porous targets. This can be attributed to some energy being used to collapse the pores in porous materials. Additionally, underground nuclear explosions have a stronger coupling to the ground and hence the highest seismic efficiency.

Teanby and Wookey (2011) estimated the most appropriate seismic efficiency value for Mars to be 2×10^{-5}. Teanby (2015) later revised this value to 5×10^{-4} (marked as solid black line on Fig. 2.3).

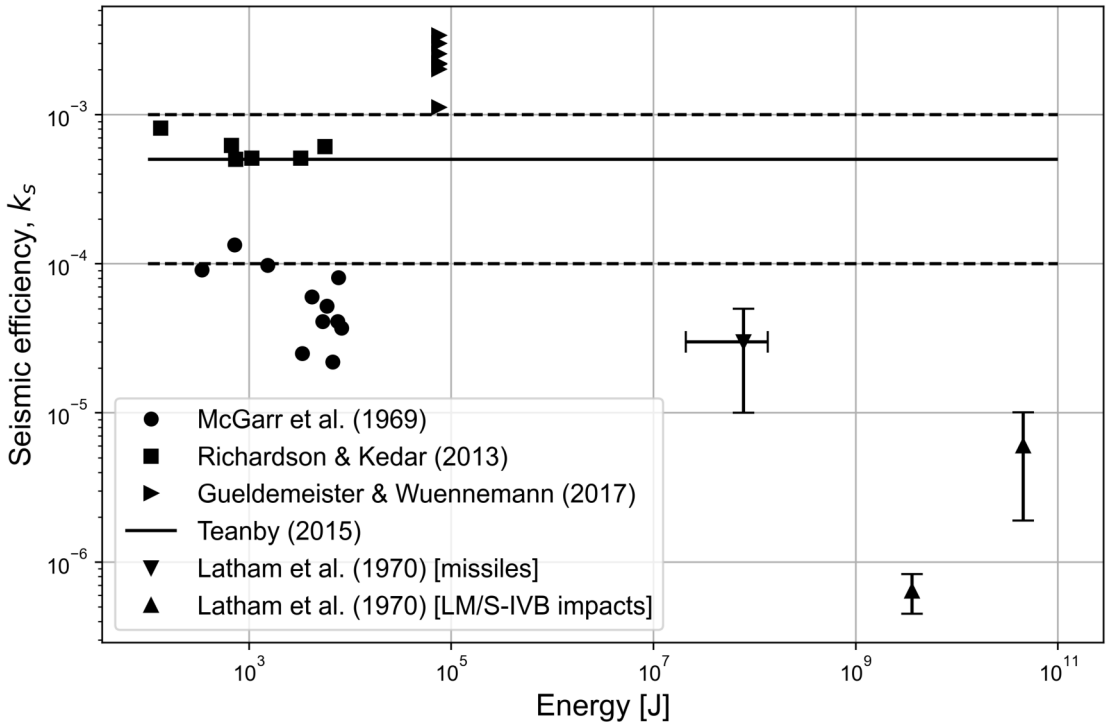

Figure 2.3: Seismic efficiency values (k_s) for a number of impact experiments in literature. This dataset includes laboratory experiments (Richardson and Kedar, 2013; McGarr et al., 1969), numerical modelling results (Güldemeister and Wünnemann, 2017), artificial impacts on the Moon (Latham et al., 1970a) and terrestrial missile impacts (Latham et al., 1970b). The solid black line is the value of 5×10^{-4} proposed as an appropriate value to be used for natural impacts on Mars by Teanby (2015). The dashed lines show the uncertainty on this proposed value.

2.3.3 Source-time function

The source time function in seismology is a representation of the forces acting on the surface and subsurface at the source during a seismic event, as a function of time (Daubar et al., 2018). The duration of the seismic source provides a measure of the rate of seismic wave generation and is often defined as the rate of change of seismic moment. In the case of an impact, this duration can be related to the shock wave propagation time through the target material, until it decays into a subsonic wave. On the other hand, the magnitude of the source time function is linked to the seismic energy released during the event. The source time function is often used in wave propagation modelling to produce synthetic seismograms that could be recorded at large distances from source. This approach is similar to modelling of synthetic seismograms for earthquakes, typically represented by a double-couple source. The source duration is also a key parameter linked to the frequencies generated at a seismic source as well as the source region boundary, as demonstrated by Gudkova et al. (2015) and Daubar et al. (2018). The frequency content generated at the source also depends on the material properties at the source (Gudkova et al., 2011). In addition, the seismic waveform recorded at the receiver will also be influenced by subsurface structure along the wave propagation path.

Several models have been proposed for the source time function of an impact source, such as the GL model (based on momentum transfer during impact Lognonné et al., 2009; Gudkova et al., 2011; Gudkova et al., 2015) and the SWH model (based on scaling laws derived from explosion surface tests Shishkin, 2007; Werth and Herbst, 1963; Haskell, 1967).

Using a definition of vertical component of seismic moment of the GL model, the source time function can also be considered as the rate of momentum transfer (see Sec. 2.3.1, equation 2.21), equivalent to the vertical force acting at the source location:

$$F(t) = \frac{\mathrm{d}p_z}{\mathrm{d}t}, \tag{2.26}$$

where p_z is the vertical momentum transferred to the target during impact. The value of p_z can be determined for an impact by evaluating the integral in equation 2.22 over the source

region. The source time function derived using equation 2.26 can be represented by a simple and integrable mathematical function, following the method used in Helmberger and Hadley (1981). The source time function has a shape of a pulse, and can be approximated with Jeffrey's pulse expression (as described in Daubar et al., 2018):

$$F_{JP} = p_i \alpha t e^{-\alpha t}, \tag{2.27}$$

where p_i is the impact momentum and α is a time constant, which determines the peak amplitude and duration of the pulse. Daubar et al. (2018) showed that Jeffrey's pulse closely matches the source time function measured in small laboratory impact experiments from (Richardson and Kedar, 2013).

2.4 Numerical modelling approach

2.4.1 iSALE shock physics code

iSALE is a multi-material, multi-rheology shock physics code based on the SALE hydrocode (Simplified Arbitrary Lagrangian Eulerian; Amsden et al., 1980). An early version of SALE only allowed modelling of a single Newtonian fluid. The code was developed to include an elasto-plastic constitutive model, viscosity model, fragmentation model, several equations of state (Melosh et al., 1992). Further improvements made by (Ivanov et al., 1997) included advancing material interface tracking in Eulerian mode, incorporating damage accumulation and strain weakening as well as implementation of semi-analytical equation of state ANEOS. These developments were released as SALEB hydrocode, highly capable of simulating impact events. Collins et al. (2002) improved upon this version by implementing several rheologic models. This was released as SALES-2. Wünnemann et al. (2002) substantially rewrote large parts of SALE, implementing addition of third target material (Wünnemann et al., 2003). More recently, several strength models describing geologic materials were added to iSALE (Collins et al., 2004) as well as the $\epsilon-\alpha$ compaction model for representing porous materials (Wünnemann et al., 2006; Collins et al., 2011).

Two-dimensional simulation domain In iSALE-2D simulations, the simulation domain is subdivided into smaller rectangular cells with 4 vertices (Fig. 2.4). The simulation mesh usually comprises a high resolution zone and an extension zone. In the high resolution zone, cells have a constant, pre-defined size. This part of the mesh usually contains the impactor and stretches around the impact point, where the materials likely experience the most extreme pressures and accelerations. In the extension zone on the other hand, cell width increases by a pre-defined scaling factor (grid extension parameter) away from the high resolution zone. This approach allows the simulation mesh to cover areas far away from the crater at a lower computational cost. In addition it can help minimise reflection effects from mesh boundary. Because simulations in this work focus on tracking the seismic waves generated during impact

across the mesh, it is important that high resolution is maintained across the entire domain. Therefore extension zones are not employed in this work. Typically, impact simulations use an axially symmetric cylindrical geometry, with the symmetry axis on the left side of the mesh.

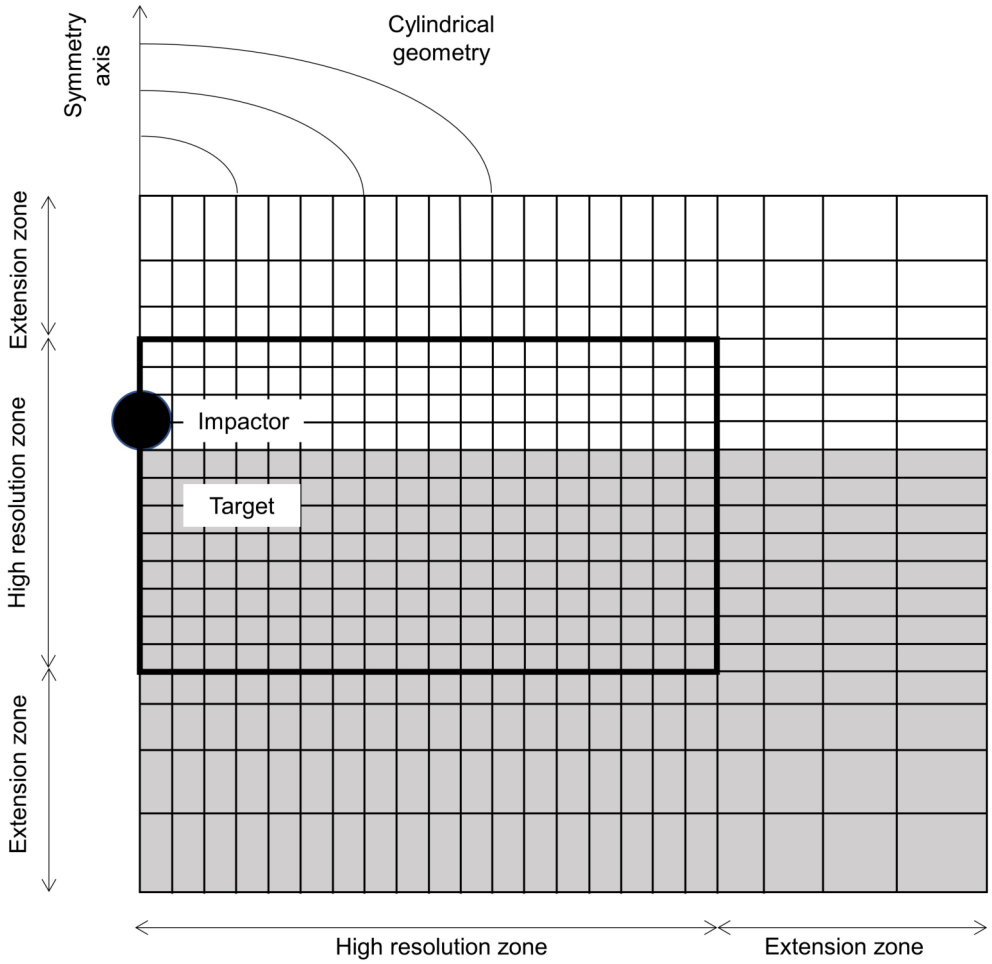

Figure 2.4: Schematic representation of cylindrical mesh geometry in iSALE-2D. The mesh is divided into cells and consists of high resolution zone surrounding the impact point (where cell size remains constant) and an extension zones (where cell size increases by a constant factor).

As described above, the simulation domain is subdivided into smaller units, called cells. A set of differential equations is then used to describe the deformation introduced to the material by the impact. There are two key approaches of describing those deformations: Eulerian, where the reference frame is fixed and the material is allowed to move across it, and Lagrangian, where the reference frame moves along with the material. In practice this means that in Eulerian mode, the simulation mesh dimensions will remain static throughout the simulation, and the material can move between cells. In a Lagrangian mode however, the material remains inside the original cell, whilst the simulation mesh deforms. Whilst iSALE is capable of using either description, in

simulations where strong material deformations are expected, such as hyper-velocity impacts, using the Lagrangian reference frame can lead to problems such as nonphysically small cell dimensions. Therefore all simulations in this thesis used the Eulerian mode.

Fundamental equations The three laws forming the basis of shock physics codes, including iSALE, are: conservation of mass, momentum and energy. In the Eulerian descriptions those equations can be expressed as:

$$\text{Conservation of mass} \qquad \frac{\partial \rho}{\partial t} + v_i \frac{\partial \rho}{\partial x_i} = -\frac{\partial v_i}{\partial x_i}, \tag{2.28}$$

$$\text{Conservation of momentum} \qquad \rho \frac{\partial v_i}{\partial t} = F_i + \frac{\partial \sigma_{ij}}{\partial x_j}, \tag{2.29}$$

$$\text{Conservation of energy} \qquad \rho \frac{\partial E}{\partial t} = -P \frac{\partial v_i}{\partial x_i} + s_{ij} \dot{\epsilon}'_{ij}, \tag{2.30}$$

where ρ is density, x is position in space, t is time, v_i is velocity, σ_{ij} is the stress tensor (consisting of the hydrostatic pressure P, and the deviatoric part, s_{ij}), F_i is the force per unit volume and $\dot{\epsilon}'_{ij}$ is the strainrate. In the Lagrangian descriptions those equations take the foloowing form:

$$\text{Conservation of mass} \qquad \frac{\mathrm{D}\rho}{\mathrm{D}t} = -\frac{\partial v_i}{\partial x_i}, \tag{2.31}$$

$$\text{Conservation of momentum} \qquad \rho \frac{\mathrm{D}v_i}{\mathrm{D}t} = F_i + \frac{\partial \sigma_{ij}}{\partial x_j}, \tag{2.32}$$

$$\text{Conservation of energy} \qquad \rho \frac{\mathrm{D}E}{\mathrm{D}t} = -P \frac{\partial v_i}{\partial x_i} + s_{ij} \dot{\epsilon}'_{ij}. \tag{2.33}$$

Two additional equations are needed to fully describe and solve the system: the equation of state (EoS) and the constitutive (strength) model. The EoS describes the relationship between pressure, deformation and internal energy ($P = f(\rho, E)$) and is discussed in more detail in Sec. 3.2.2. The strength model relates the deformation (defined by the stress tensor, σ_{ij}) as a function of strain ϵ_{ij}, strainrate $\dot{\epsilon}'_{ij}$, pressure P, energy E and damage D ($\sigma_{ij} = f(\epsilon_{ij}, \dot{\epsilon}'_{ij}, P, E, D)$). A more detailed discussion of the strength models used in this thesis is also presented in Sec. 3.2.2.

Lagrangian probes As described above, modelling hyper-velocity impact events necessitates the use of the Eulerian setup. Because it allows the material to move between cells, it is difficult to recover the history of the state of material. As a solution to this problem, Lagrangian probes that move with the flow can be used in iSALE simulations to record the history of particular part of material as a function of time. Probes can therefore be understood to behave as virtual seismometers. An additional advantage of using probes to record seismic waves in iSALE is the higher temporal resolution that can be achieved, in comparison to information saved in each cell. Cell variables are recorded at every save time of the simulation, whilst probes record information at every timestep. Typically, for simulations in this thesis, a save time contains 100s of timesteps.

Probes can be placed freely at any coordinate within the simulation domain. For example, in the problems simulated in Chapter 3, probes are placed in a a 'fan-shaped' arrangement, radially away from the impact point. This functionality is further used in Chapter 5 to record ground motion at high temporal resultion.

2.4.2 Material models

iSALE uses several key relationships to describe the material properties response to changes in variables such as pressure (P) or temperature (T).

Equation of State The Equation of State (EoS) is an equation that describes the relationship between pressure (P), density (ρ) and internal energy (E) of the material. The Tillotson EoS was derived specifically for hypervelocity impact simulations into metal targets, and takes two forms. The first form applies when the material considered is in a compressed state, where the density ρ is higher than the initial density ρ_0. The pressure is then given by:

$$P_c = \left[a + \frac{b}{E/(E_0\eta^2) + 1}\right] \rho E + A(\eta - 1) + B(\eta - 1)^2, \tag{2.34}$$

where $\eta = \rho/\rho_0$ is the ratio of compressed and reference densities, a, b, A and B are the material specific Tillotson parameters. The second form of the Tillotson EoS applies when the material is in an expanded state, where the density ρ is lower than reference density ρ_0. The pressure in this state is given by:

$$P_e = \alpha + \left[\frac{b}{E/(E_0\eta^2)+1} + A(\eta-1)e^{-\beta\frac{1-\eta}{\eta}}\right] e^{-\alpha\frac{(1-\eta)^2}{\eta^2}}, \tag{2.35}$$

where α and β are constants. A special case applies when the material considered is in the partial vaporisation regime, where $\rho/\rho_0 < 1$ and $E_{iv} < E < E_{cv}$. In order to create a smooth transition between the compressed and expanded regime, the pressure is computed using both forms of the EoS:

$$P = \frac{(E-E_{iv})P_e - (E_{cv}-E)P_c}{E_{cv}-E_{iv}}. \tag{2.36}$$

Strength model In addition to the EoS, a strength model is necessary to describe the materials behaviour when subjected to high stresses, such as during an impact. Strength model describes the relationship between stress σ, strain ϵ, strain rate $\dot{\epsilon}$, pressure P and temperature T. A measure of damage (or fracturing of the material) is also often included in various strength models.

The Lundborg strength model (referred to as LUNDD in iSALE) is a simple pressure-dependent strength model (Lundborg, 1968; Collins et al., 2004). The yield strength Y is defined as:

$$Y = Y_{d0} + \frac{\mu P}{1+\frac{\mu P}{Y_{dm}-Y_{d0}}}, \tag{2.37}$$

where P is pressure, μ is the coefficient of internal friction, Y_{d0} is the cohesion (yield strength at zero pressure) and Y_{dm} is the limiting strength at high pressure for a damaged material. The Lundborg strength model is used in this thesis for representing regolith-like materials.

The ROCK strength model is a more complex strength model, which depends on both damage

and pressure (Collins et al., 2004). The yield strength Y is defined here as:

$$Y = Y_d D + Y_i(1 - D) \tag{2.38}$$

where D is a measure of damage ranging from 0 (intact) to 1 (damaged). The behaviour of D is defined by a separate damage model. The work contained in this thesis used the Ivanov damage model, which defines D as a function of plastic strain:

$$D = \min\left(\frac{\epsilon_p}{\epsilon_f}, 1\right), \tag{2.39}$$

where ϵ_p is the accumulated plastic strain and ϵ_f is the plastic strain at failure. ϵ_f is defined as a function of pressure:

$$\epsilon_f = \max\left(\epsilon_{fb}, B(P - p_c)\right), \tag{2.40}$$

where ϵ_{fb} is the minimum failure strain for low pressure state, p_c is the pressure above which compressional failure occurs, and B is a constant.

The damaged material strength Y_d is defined as:

$$Y_d = \min(Y_{d0} + \mu_d P, Y_{dm}), \tag{2.41}$$

where μ_d is the internal friction coefficient for damaged material and Y_{dm} is the limiting strength of the damaged material at high pressure. The strength of the intact material is given by:

$$Y_i = Y_{i0} + \frac{\mu_i P}{1 + \frac{\mu_i P}{Y_{im} - Y_{i0}}}, \tag{2.42}$$

where μ_i is the internal friction coefficient for intact material and Y_{im} is the limiting strength of the intact material at high pressure. In this work, the ROCK model was used to model bedrock-like materials.

The $\epsilon - \alpha$ compaction model In order to describe the behaviour of porous materials in iSALE simulations, the $\epsilon - \alpha$ compaction model (Wünnemann et al., 2006; Collins et al., 2011)

is used. Porosity (ϕ) is represented in terms of the ratio of densities of the solid material (ρ_s) and the porous material (bulk density, ρ)

$$\alpha = \frac{1}{1-\phi} = \frac{\rho_s}{\rho}, \tag{2.43}$$

where α is distension. For a non-porous material $\alpha = 1$ and $\phi = 0$, and for a porous material $\alpha > 1$ and $0 < \phi < 1$. iSALE computes the properties of the porous material from the EoS of a solid (non-porous) material (Herrmann, 1969; Carroll et al., 1972; Holsapple, 2008). As such, the pressure in the porous material, P, is given by the pressure in the non-porous material, P_s, divided by distension, α:

$$P = \frac{1}{\alpha} P_s(\rho_s, E_s) = \frac{1}{\alpha} P_s(\alpha\rho, E_s). \tag{2.44}$$

Instead of a pressure-based approach, in order to compute distension iSALE uses a strain-based approach, referred to as the $\epsilon - \alpha$ porous compaction model (Wünnemann et al., 2006; Collins et al., 2011). Distension is here defined as a function of the volumetric strain ϵ_V, defined as the ratio between the change in volume and the initial volume of the material. The model consists of four regimes, defined as:

Elastic compaction	$0 > \epsilon > \epsilon_e$	$\alpha = \alpha_0$	(2.45)
Exponential compaction	$\epsilon_e > \epsilon > \epsilon_X$	$\alpha = \alpha_0 e^{\kappa(\epsilon - \epsilon_e)}$	(2.46)
Power-law compaction	$\epsilon_X > \epsilon > \epsilon_c$	$\alpha = 1 + (\alpha_x - 1)\left(\frac{\epsilon_c - \epsilon}{\epsilon_c - \epsilon_X}\right)^2$	(2.47)
Compression	$\epsilon_c > \epsilon$	$\alpha = 1$	(2.48)

where ϵ_e, ϵ_X and ϵ_c give the the volumetric strain at transition points between regimes. At $\epsilon > \epsilon_e$, compaction is elastic (reversible) and α is equal to the initial distension. When the volumetric strain increases beyond ϵ_e the material enters the exponential compaction regimes, where compaction is no longer elastic (i.e. irreversible). As the strain continues increasing, crushing of pore spaces eventually slows, transitioning into the power-law regime. Once ϵ reaches ϵ_c, all pore spaces are crushed and the porosity is 0.

Instead of computing the distension directly using equations 2.45–2.48, iSALE updates α using the following relationship based on compaction rate $\frac{\mathrm{d}\alpha}{\mathrm{d}\epsilon}$:

$$\alpha_{n+1} = \alpha_n + \frac{\mathrm{d}\alpha}{\mathrm{d}\epsilon}\frac{\mathrm{d}\epsilon}{\mathrm{d}t}\Delta t. \tag{2.49}$$

The original $\epsilon - \alpha$ compaction model derived by Wünnemann et al. (2006) used the assumption that distention in the elastic regime remains constant, at the value of initial distension. However, in reality, porosity decreases slightly as the volumetric strain is increased, even in the elastic regime, although it can be regained if the material is released. To quantify the change in porosity in the elastic regime, Collins et al. (2011) defined the elastic compaction rate as:

$$\frac{\mathrm{d}\alpha}{\mathrm{d}\epsilon_V} = \alpha\left[1 - \frac{c(\alpha)^2}{c_{s0}}\right], \tag{2.50}$$

where c_{s0} is the bulk sounds speed of the solid (non-porous) material at zero pressure, and $c(\alpha)$ is the bulk sound speed of the porous material also at zero pressure. Following Herrmann (1969), $c(\alpha)$ is assumed to vary linearly with α:

$$c(\alpha) = c_{c0} + \frac{\alpha - 1}{\alpha_0 - 1}(c_0 - c_{s0}). \tag{2.51}$$

2.5 InSight mission

The Interior Exploration using Seismic Investigations Geodesy and Heat Transport (InSight) mission (Banerdt and Russell, 2017) landed on Mars in November 2018, after a 6 month-long journey. The first few weeks on the surface were used to check the lander's condition, unravel the solar panels and gather information about the landing site including taking images of the surface. Imaging the surface around the lander was a crucial step to determine the ideal location to deploy the seismometer and heat probe.

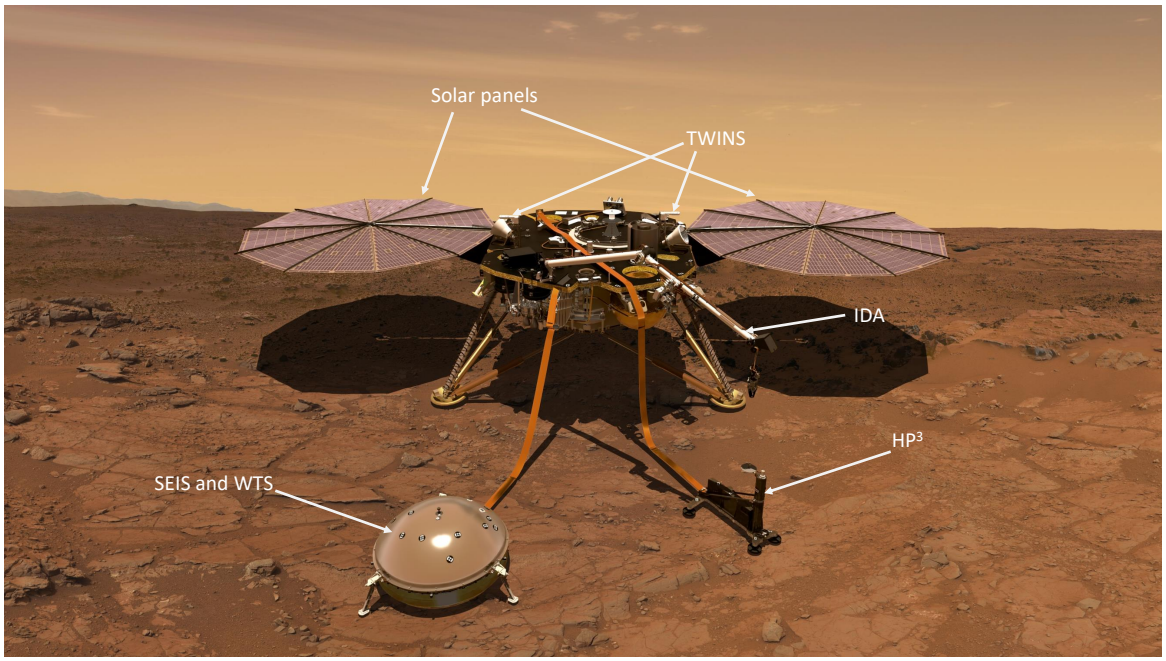

Figure 2.5: Artist's concept diagram of the InSight lander. The main instruments are labelled with white arrows: the seismic package SEIS (Seismic Experiment for Internal Structure) covered by a Wind and Thermal Shield (WTS), the heat probe HP^3 (Heat Flow and Physical Properties Package), the temperature and wind sensors (TWINS). Several other pieces of hardware are also labelled: the solar panels, the Instrument Deployment Arm (IDA) (image adapted from: NASA/JPL-Caltech).

The two main science objectives of the primary mission were to understand the formation and evolution of Mars in the past and to measure the current level of seismic activity on the planet.

In order to achieve those, the lander is equipped with a variety of instruments, including the most relevant for this work seismic package, named SEIS (Seismic Experiment for Internal Structure, shown in Fig. 2.5; Lognonné et al., 2019). SEIS consists of 2 three-component

seismometers: a short period (SP) and a very broad band (VBB) sensitive to frequencies 0.01–50 Hz. The instrument produces very low self-noise, lower than any seismometer placed on a planetary body to date. This allowed the daily and seasonal seismic noise variation on Mars to be very well characterised. At the landing site, low noise levels ($\sim 1.5 \times 10^{-10}$ ms^{-2}Hz$^{-1/2}$) are observed from early afternoon Local Mean Solar Time (LMST) until midnight. The noise levels are highest between early morning and late afternoon LMST (reaching accelerations of $\sim 1 \times 10^{-7}$ms^{-2}Hz$^{-1/2}$). Overall, the low noise levels on Mars are significantly lower than on Earth, and allow SEIS to detect marsquakes of moment magnitude 1.8 lower than is possible on Earth (Lognonné et al., 2020).

Over 1000 marsquakes were detected (Clinton and Euchner, 2021), many of them teleseismic (at distances $> 60°$). This has led to significant advances in our understanding of Mars' internal structure, including constraints on the structure of upper mantle (Khan et al., 2021). The thickness of the martian crust was determined to be between 24–72 km (Knapmeyer-Endrun et al., 2021). The core-mantle boundary (CMB) reflection (ScS phases) were detected in several marsquake signals, which led to the discovery of the planet's core being large (1830 km in radius) and liquid (Stähler et al., 2021). Regional marsquakes were used to constrain the shallow properties of the crust. Lognonné et al. (2020) also used the hammering of HP^3 to put constraints on the near-surface soil properties at the landing site.

Seismic detections of meteorite impacts are a valuable tool for determining the internal structure of the planet, central to more than half of the primary mission goals. Explicitly, one of the primary goals of the InSight mission was to measure the impact rate on the surface of Mars within a factor of 2. Meteorite impacts are known to occur more frequently on Mars than on Earth, due to its thinner atmosphere and proximity to the asteroid belt. Impact-generated seismic waves were therefore expected to significantly contribute to the seismicity of Mars. Because meteorite impacts usually form a visible crater on the surface of a planet, an advantage of an impact source is our ability to find its exact location using orbital imagery. This is in contrast to marsquakes of tectonic origin, which usually do not produce a visible disturbance on the surface. A seismically located impact can be used as a calibration for the other seismic events recorded and provide useful information on the martian internal structure. The properties of

the crater can also be used to constrain the impactor properties. Measuring the cratering rate on the planet is also relevant to the wider planetary science community as crater production rates are used for dating planetary surfaces. As human missions to Mars become reality in the future, an accurate measure of impact rate will prove to be a crucial element in assessing the risk to those missions.

2.5.1 Marsquake Classification

The seismic events are classified by Marsquake Service (MQS) based largely on their frequency content (Clinton et al., 2021), which is heavily linked to the source geometry, but is also influenced by the structure encountered along the waves' propagation paths. The two main marsquake families are: Low Frequency (LF) family, which have energy generally at long periods; and High Frequency (HF) family, which have energy at high frequencies (usually above 2.4 Hz). The low frequency event family is divided into two types:

- Low Frequency (LF) — characterised by energy on all 3 components below 2.4 Hz.
- Broadband (BB) — characterised by energy on all 3 components below 2.4 Hz but also at or above 2.4 Hz.

The high frequency family is subdivided into three sub-families:

- High Frequency (HF) — characterised by energy mostly at and above 2.4 Hz, usually up to 10 Hz, with possible energy below 2.4 Hz.
- '2.4 Hz events' — characterised by energy only at 2.4 Hz. These events are considered to be small HF events.
- Very High Frequency (VF) — characterised by higher energy at horizontal components and at frequencies above 2.4 Hz, up to 35 Hz.

Furthermore, seismic events recorded are also assigned a quality between A and D, which takes into account the visibility of distinct seismic phases and the ability to constrain the distance

to source (Clinton et al., 2021; Böse et al., 2021). More specifically, each quality is defined according to the following characteristics:

- Quality A ('high quality') — several clear phases and clear polarisation. Those events can be located both in distance and azimuth, using the approach described in Böse et al. (2017).
- Quality B ('medium quality') — several clear seismic phases, but no clear polarisation of the signal. Those events can be located in distance, but no back-azimuth can be determined.
- Quality C ('low quality') — no distinct seismic phases identifiable. Those events cannot be located, but they are clearly observable.
- Quality D ('suspicious') — unclear and weak signals, with no observed phases or polarisation. Those signals may not be attributable to seismic events.

2.6 Pre-landing predictions

Before the lander's arrival on Mars, the expected number of detectable impacts had been estimated using several methods (Teanby and Wookey, 2011; Teanby, 2015; Daubar et al., 2015; Lognonné and Johnson, 2015). Teanby and Wookey (2011) estimated detectable impact numbers by combining seismic wave-form modelling, observed cratering rates and an empirical relationship between crater size and seismic moment. For the most optimistic noise level, they predicted that a globally detectable large impact would occur once per year. For a nominal noise, such impacts occur once every 10 years, making it unlikely that one would occur during InSight's operations. Teanby (2015) updated the above predictions using a revised value of seismic efficiency of 5×10^{-4}, concluding that between 0.1–30 regional (at distances $< 1000\,\mathrm{km}$) impacts would be detectable by InSight every year, with nominal values between 1–3 per year.

Daubar et al. (2018) provided a comprehensive review of the present knowledge about impact-generated seismic signals, and the implications for the InSight mission. The predicted number of

impact detections was determined to be between few to few tens of impacts over the duration of the primary InSight mission (1 martian year), in agreement with Teanby (2015) above. Daubar et al. (2018) also reviewed a number of discriminators that could be used to identify impacts in the seismic data. These qualities are:

1. positive first motion away from the source,
2. higher P/S amplitude ratio compared to tectonic events,
3. presence of surface waves and high ratio of surface wave magnitude (M_S) to body wave magnitude (m_B),
4. frequency spectrum unusual for a tectonic source, such as a high frequency overshoot or very steep high frequency decay,
5. lack of phases characteristic of deep marsquakes, such as pP, indicating a wave reflected from the underside of the planet's surface.

All the above discriminators have been used in the past on Earth to discriminate between impulsive/explosive sources and tectonic events. Points 3 and 5 can be attributed to the shallow depth of seismic source in the case of an impact. Point 1, 2 and 4 are caused by the unique geometry of an impact source. However, because all of the above points can be properties of a shallow tectonic source, the discriminators can be used to exclude an impact source, rather than unambiguously confirm it.

2.7 Conclusions

Meteorite impacts provide a unique opportunity to probe and expand our understanding of planetary interiors using seismology. They can serve as a calibration for other seismic signals because they can be extremely well localised using orbital imagery. However, the effect of impact properties such as impactor velocity, size and the materials involved, on the seismic signal characteristics are poorly constrained. Data recorded from natural impacts on Earth (Brown

et al., 2008; Kenkmann et al., 2009) and the Moon (McGarr et al., 1969) suffers from unknown impact conditions. On the other hand, artificial impacts (Latham et al., 1970a; Fernando et al., 2021a) provide well constrained impact conditions but the often used metal projectiles are poor analogs for meteorites. Laboratory studies can offer a solution to both of the above downsides, but they usually focus on smaller scale impact (e.g. Richardson and Kedar, 2013). Numerical modelling approaches are therefore a key way in which impact-generated seismic waves on planetary scales can be studied, as shown by Güldemeister and Wünnemann (2017). This thesis aims to fill the gaps in current knowledge by deriving the relationships between impact properties and several key seismic signal characteristics, as presented in Chapter 3.

Seismic detections of meteorite impacts are also an opportunity to test our knowledge of the impact rate on Mars. Impact rates are crucial for determining the ages of planetary surfaces. They are also becoming increasingly relevant for assessing the risk to future human space missions. The crater production curves have been determined theoretically, by extrapolating the crater counts on the Moon over geologic rates (Hartmann, 2005). Current impact rates are being measured using repeated orbital imaging, where formation of fresh craters can be constrained to within months or years (Daubar et al., 2013; Daubar et al., 2022). Seismology offers a new independent way of measuring the impact rate on Mars. Chapter 4 uses a combination of numerical modelling and impact data recorded on Mars, Moon and Earth to determine the seismic detectability of impacts. A subset of marsquakes detected by InSight is then used to derive an implied impact rate.

The frequency content of seismic signals is expected to be linked to the source mechanism, and in pre-landing assessment it was determined to be one of the key characteristics that can be used to identify impacts in seismic data recorded by InSight (Daubar et al., 2018). However, the relationship between impact conditions and the frequency spectrum is unclear. This problem is addressed in Chapter 5.

The InSight mission is the first successful seismology-based mission on the surface of Mars. The data recorded during its operations resulted in significant advances in our understanding of the internal structure of Mars (e.g. Giardini et al., 2020; Stähler et al., 2021) as well as the

impact cratering process and the impact detectability (e.g. Daubar et al., 2019; Garcia et al., 2022). The success of the InSight mission paves the way for future seismology-based mission to Mars and other bodies in our Solar System.

Chapter 3

Seismic source properties of small impacts on Mars

This chapter is based on a study published in Journal of Geophysical Research: Planets, Wójcicka et al. (2020), and Lunar and Planetary Science Conference abstract, Wójcicka et al. (2021).

3.1 Introduction

The InSight lander began measuring seismic signals on Mars in early 2019, providing the first measurements of martian seismicity (Banerdt et al., 2020). InSight's seismometer is outperforming its design requirements, with a lower noise floor than any previous seismometer deployed on a terrestrial body (Lognonné et al., 2020). However, during the first martian year of operations, no InSight signals have been unequivocally attributed to meteorite impacts (Banerdt et al., 2020; Giardini et al., 2020). Nominal pre-landing predictions estimated that in one martian year between a few and tens of small impacts (forming craters of diameter 0.5–20 m) would be detectable by InSight, the majority of which would be occurring on a regional scale (Daubar et al., 2018; Teanby and Wookey, 2011; Teanby, 2015). While the uncertainty on these detection estimates is large (ranging 0.1–30/Earth year), the discrepancy between predic-

tions and observations during the first year of operations suggests that some of the assumptions relating to impact detectability required revision.

Seismic detectability estimates for small impacts on Mars make assumptions about the seismic moment and seismic efficiency (the proportion of the impact energy radiated as seismic waves) of impacts that are likely to occur during InSight's lifespan. However, neither quantity has been well constrained for impacts of relevant scale, primarily due to lack of observational and experimental data. Several scaling relationships relating seismic moment to impactor properties have been proposed (Shishkin, 2007; Lognonné et al., 2009; Teanby and Wookey, 2011; Gudkova et al., 2015), but their seismic moment predictions differ by more than an order of magnitude for small impacts (Daubar et al., 2018).

Seismic efficiency has been measured in laboratory-scale impact experiments (McGarr et al., 1969; Richardson and Kedar, 2013; Yasui et al., 2015), artificial or missile impact experiments on the Moon and Earth (Latham et al., 1970a; Latham et al., 1970b), in numerical simulations (Güldemeister and Wünnemann, 2017), and via theoretical scaling relationships (Shishkin, 2007; Lognonné et al., 2009). However, the resulting seismic efficiency estimates span four orders of magnitude (10^{-3}–10^{-7}). This is likely due to variations in target and impactor properties, but a thorough understanding of their influence on seismic efficiency is lacking. Additionally, up-scaling the results of small scale laboratory experiments to the relevant momentum range is difficult. Teanby and Wookey (2011) suggested a reference seismic efficiency value for Mars of 2×10^{-5}, and used that to estimate the detectability of teleseismic impacts; more recent work has proposed a nominal value of 5×10^{-4} (Teanby, 2015; Daubar et al., 2018). Improved understanding of seismic moment and seismic efficiency would enhance impact detectability models on Mars and provide more robust initial conditions for seismic wave propagation modelling, and perhaps help explain the current lack of definitive impact detections from InSight.

This chapter uses the iSALE-2D (impact Simplified Arbitrary Lagrangian Eulerian) shock physics code (Amsden et al., 1980; Collins et al., 2004; Wünnemann et al., 2006) to simulate vertical impacts onto martian regolith in the size range of events expected during the

InSight mission. For each simulation, the impact is characterised as a seismic source by calculating the scalar seismic moment and seismic efficiency. The results are also used to examine the anisotropy of the seismic moment tensor for vertical impacts and hence probe the analogy between impacts and underground explosions. A smaller subset of simulations is used to constrain the dependence of impact conditions on the source time function.

3.2 Methods

3.2.1 Modelling approach

The iSALE shock physics code was used to simulate seismic wave generation by small impacts on Mars. In this first investigation of seismic signals generated by impacts on Mars a range of typical impact scenarios likely to be detected by InSight was considered, including the size range of the newly occurring nearby crater.

3.2.1.1 Impact scenario selection

Following pre-landing impact detection estimates (Teanby, 2015) this study focuses on impacts most likely to be detected during the InSight mission: those that produce craters of diameter 1–30 m, which occur across Mars ∼1000–10 times per Earth year. Accounting for uncertainty in target strength (Daubar et al., 2020) and applying well-established impactor crater scaling equations (Holsapple, 1993), this corresponds to a range in vertical impactor momentum, radius and mass of 10^3-10^7 kg ms^{-1}, 0.03-0.5 m and 0.5-10^3 kg, respectively (Fig. 3.1).

As the smallest impactors in this size range are likely to be substantially retarded by atmospheric entry, the ground impact velocity and post-ablation mass for each impactor size was chosen by solving the standard equations of meteoroid entry dynamics (McMullan and Collins, 2019). These calculations assumed a pre-entry impactor speed of 10 kms^{-1}, the average impact speed on Mars (Le Feuvre and Wieczorek, 2011), an initial impact angle to the horizontal of 45° (the most probable impact angle) and an impactor density of 2860 kgm^{-3} (to be consistent with the impactor material model, see Section 3.2.2). To simulate seismic wave generation following ground impact the oblique impact is approximated as a vertical impact, whose associated calculations are significantly less computationally demanding, allowing wave propagation tracking much further from the impact site than would otherwise be possible. To account for the difference in crater size between a vertical and oblique impact, this study adopted the widely used convention of taking the vertical component of the oblique ground impact velocity as the impact

speed in simulations of vertical impact scenarios (Chapman and McKinnon, 1986; Elbeshausen et al., 2009). The expected crater size, vertical impact momentum and vertical component of the impact velocity are shown as a function of impactor radius in Fig. 3.1; the impactor size, vertical impact speed at the ground and crater size estimates are given in Table 3.1. Of those considered, scenarios 1 and 2 represent plausible candidates for the 1.5-m crater discovered ∼40 km from InSight (Daubar et al., 2020).

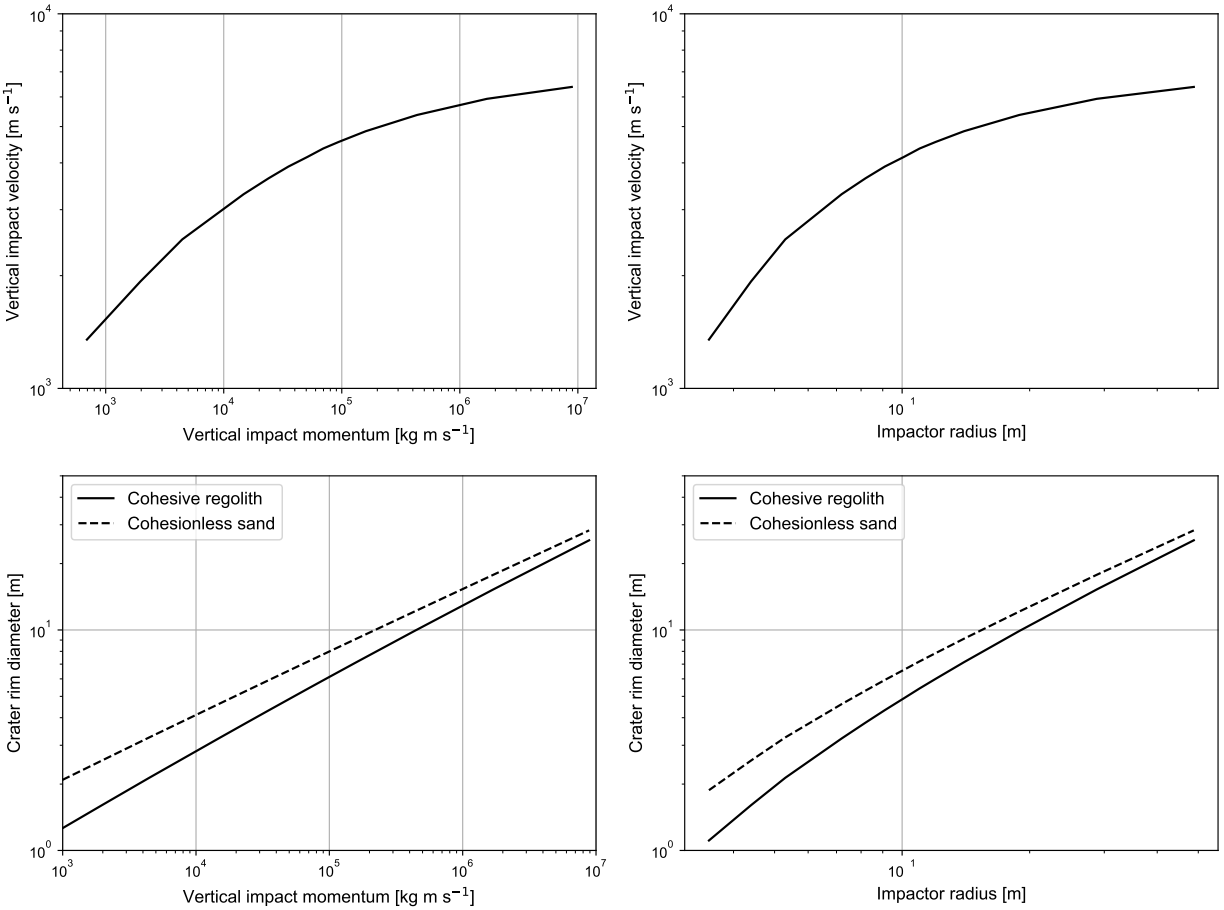

Figure 3.1: The expected crater size, vertical impact momentum and vertical component of the impact velocity (for an atmospheric entry velocity of 10 kms^{-1}) are shown as a function of impactor radius. Crater rim diameter estimates used π-group scaling (Holsapple, 1993) for cohesionless dry sand and for a porous cohesive regolith with a nominal strength $Y = 50$ kPa, with a target density of 1590 kgm^{-3}, an impactor density of 2860 kgm^{-3} and a surface gravity 3.71 ms^{-2} (see Section 3.2.2 for detailed material model justification). A 30% enlargement factor is applied to convert from preimpact-level to rim-level diameter and to account for rim collapse (Holsapple, 1993).

Table 3.1: Impactor radius (r_i), vertical velocity (v_i) and predicted crater diameters for simulations in this work. Listed scenarios were simulated using the large simulation mesh, until the shock wave decayed into an elastic wave.

Simulation number	Impactor radius, r_i [m]	Vertical velocity, v_i [ms^{-1}]	Rim diameter (sand) [m]	Rim diameter (regolith) [m]
1	0.035	1350	1.88	1.11
2	0.044	1930	2.56	1.60
3	0.053	2500	3.26	2.14
4	0.072	3300	4.61	3.22
5	0.082	3640	5.31	3.80
6	0.091	3910	5.93	4.33
7	0.10	4150	6.60	4.90
8	0.11	4370	7.21	5.43
9	0.12	4550	7.85	6.00
10	0.14	4860	9.13	7.15
11	0.19	5370	12.1	9.89
12	0.29	5930	17.8	15.3
13	0.49	6380	28.3	25.5

Table 3.2: Impactor radius (r_i), vertical velocity (v_i) and target material for simulations used to measure the source time function in this work. These scenarios were only simulated at very short time scales in order to explore the source time function's response to individual impact parameters.

Simulation number	Impactor radius, r_i [m]	Vertical velocity, v_i [ms^{-1}]	Target material
2_{v1000}	0.044	1000	regolith
2_{v3000}	0.044	3000	regolith
2_{v4000}	0.044	4000	regolith
$2_{r0.082}$	0.082	1930	regolith
$2_{r0.12}$	0.12	1930	regolith
$2_{r0.49}$	0.49	1930	regolith
$2_{\text{fractured bedrock}}$	0.044	1930	fractured bedrock
2_{bedrock}	0.044	1930	intact bedrock
$5_{\text{fractured bedrock}}$	0.082	3640	fractured bedrock
5_{bedrock}	0.082	3640	intact bedrock
$9_{\text{fractured bedrock}}$	0.12	4550	fractured bedrock
9_{bedrock}	0.12	4550	intact bedrock
$13_{\text{fractured bedrock}}$	0.49	6380	fractured bedrock
13_{bedrock}	0.49	6380	intact bedrock

3.2.1.2 Simulation mesh

Vertical impacts were simulated using a two-dimensional mesh in cylindrical (r-z) geometry. To capture the impact process and stress wave propagation from the moment of impact until

the stress wave transitioned well into the elastic regime, a computational domain extending to >10 times the expected crater radius, >100 times the impactor radius, was required. In most simulations, the required mesh extended 3000 cells in both horizontal and vertical directions, affording an impactor resolution of 10 cells per projectile radius (CPPR). Therefore, for a 4.4 cm impactor radius (model 2 in Table 3.1), the cell size was 4.4 mm and the simulation domain extended to 13.2 m across and below the surface. This spatial resolution has proven adequate previously to accurately capture stress-wave decay for determining seismic efficiency (Güldemeister and Wünnemann, 2017). To diagnose the propagation and decay of the impact-generated stress wave, the state of field variables in the mesh was saved at regular time intervals. In order to gain a higher temporal resolution record of wave propagation at specific points in the target material, Lagrangian probes were placed radially away from impact point (circular markers in Fig. 3.2). In particular, probes measured residual displacement for use in seismic moment calculations. They also measured pressure-time pulse amplitude and width for use in seismic energy and efficiency calculations.

A particularly challenging part of this work was tracking accurately the shock wave as it decayed in amplitude by six orders of magnitude into a very weak stress wave that induced displacements as small as 2×10^{-4} impactor radii. Therefore, in most simulations gravitational acceleration and hence the effect of overburden pressure were neglected. In iSALE's standard implementation, including gravity requires the construction of an initial vertical pressure (and density) gradient in the target that balances the gravitational acceleration to a prescribed tolerance. However, even a small, unavoidable imbalance can lead to nonphysical stress waves that, while very low amplitude, are sufficient to contaminate the far-field wave field and prevent accurate tracking of the impact wave to long distances.

The total number of cells in the simulation mesh employed renders the time taken to fully simulate the crater formation unreasonably long. This study therefore relies on crater scaling relationships (Holsapple, 1993) to determine the final crater size. This approach is justified here because previous work has demonstrated very good agreement between these scaling relationships and the results of iSALE vertical impact simulations in a range of target materials (Wünnemann et al., 2006; Güldemeister and Wünnemann, 2017; Prieur et al., 2017; Raducan

et al., 2019).

Of the scenarios in Table 3.1, scenarios 2, 5, 9 and 13 onto martian-like regolith were also simulated using a smaller simulation domain and high temporal resolution to measure the source time function of each scenario. The typical simulation mesh in this case comprised 500 cells in horizontal and vertical directions, with the impactor resolved at 10 CPPR, as above. The smaller mesh was necessary to capture the very sharp rise of force at the source at high enough temporal resolution of 1×10^{-6} s, without rendering data files unreasonably large. The generated shock wave was tracked for 1 ms after the impact. Fig. 3.3 shows three snapshots of such a simulation. In addition to the 4 initial impact scenarios, the velocity and impactor radius were varied individually between 1-4 kms^{-1} and 0.044-0.49 m, respectively, to investigate the effect of each parameter on the source time function. The four initial scenarios were also repeated in fractured and intact bedrock targets, to test the sensitivity of source time function to target material properties. The specific properties of each material model employed are described in the following section.

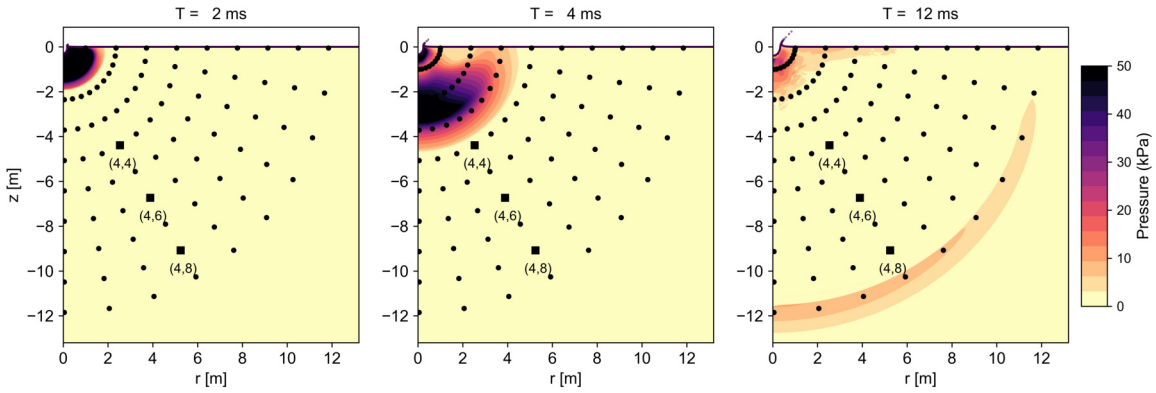

Figure 3.2: Three snapshots of impact-generated stress wave as it traverses the simulation mesh for a nominal vertical impact of a 1-kg basalt projectile striking the target at 1.93 kms^{-1}. Markers indicate locations of Lagrangian probes acting as virtual seismometers. Properties of the three probes highlighted by black squares are shown in more detail in later sections.

3.2.2 Material models

In this work, Tillotson equation of state for basalt was used to describe the impactor's and target's volumetric response (see Table 3.3 for a full list of parameters). Because the impact

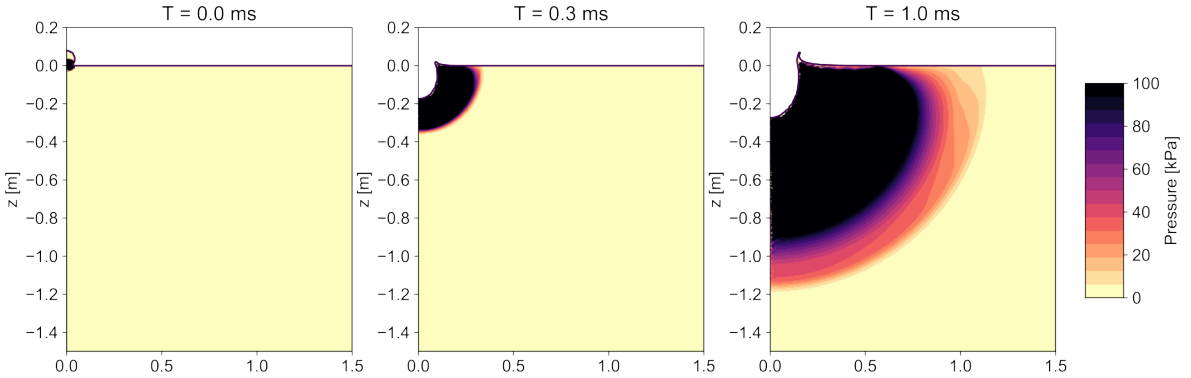

Figure 3.3: Three snapshots of the impact-generated stress wave at the very early stage of the impact process, for the nominal vertical impact of a 1-kg projectile striking the target at 1.93 kms^{-1}.

velocities considered here are <10 kms^{-1}, they do not necessitate a more sophisticated EoS, hence the Tillotson EoS is considered to be a reasonable approximation in this work.

Table 3.3: Assumed Tillotson EoS input parameters[a] for basalt.

Material	ρ_0 [kgm^{-3}]	a	b	A [GPa]	B [GPa]	E_0 [MJ/kg]	α [MJ/kg]	β [MJ/kg]	E_{iv}	E_{cv}
Basalt[b]	2860	0.5	0.8	19.3	29.3	4.87	5	5	4.72	18.2

[a] For parameter descriptions see Tillotson (1962)
[b] Based on parameters given in Benz and Asphaug (1999), but with revised reference density ρ_0, bulk modulus A, b and B parameters.

3.2.2.1 Impactor

In all simulations in this study, the impactor was represented as a nonporous basalt sphere of density 2860 kgm^{-3} and a nominal rock-like strength (Britt and Consolmagno, 2003). As mentioned in the previous section, because the impact speeds considered here are rather low and do not necessitate a complex multi-phase equation of state, the computationally-fast analytical Tillotson equation of state (Tillotson, 1962) is used here to describe the impactor's volumetric response (see Table 3.3). In this work the impactor's deviatoric strength was described using a simple pressure-dependent Lundborg strength model (Lundborg, 1968) (Table 3.4).

Other than the reference density and bulk modulus, the simulation results are expected to be insensitive to the exact equation of state and strength model used to represent the impactor

material. Fig. 3.4 compares the Hugoniot curve defined by this equation of state and shock wave data for non-porous basalt.

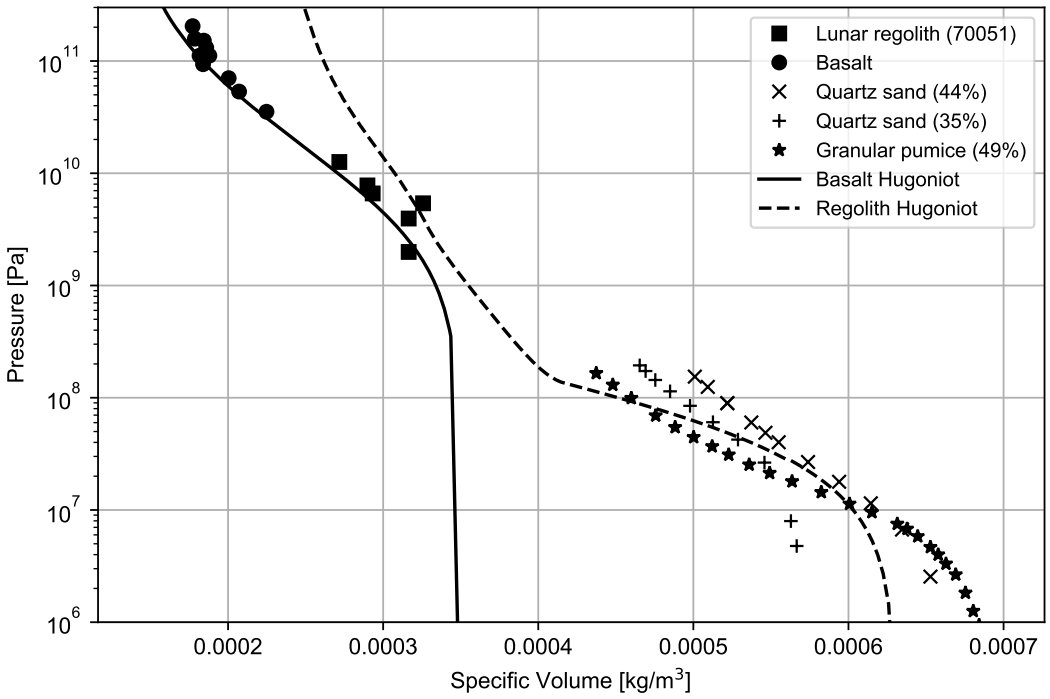

Figure 3.4: Hugoniot curves in pressure-specific volume space used to represent nonporous basalt impactor (solid line) and regolith target material (dashed line). Symbols show experimental shock (solid symbols) and crush (open symbols) data for analog materials for comparison. The porosity of the granular analog materials is given in parentheses. Shock Hugoniot for regolith and basalt data from Ahrens and Cole (1974) and Thiel (1977); quartz and pumice Hugoniot data from Luo et al. (2011) and Housen et al. (2018).

3.2.2.2 Target

The generation and propagation of seismic signals from an impact is likely to be sensitive to the nature of the martian surface at that location. The purpose of this study is to provide a baseline assessment of the seismic efficiency and moment of small impacts on Mars within hundreds of kilometers of InSight. Therefore this study considers a highly simplified target material model, broadly representative of the upper tens of meters of Mars near the lander. This shallow depth is most relevant because seismic waves from such nearby impacts will not penetrate deeper into Mars. The results presented here should therefore provide a general reference frame on which

future site-specific investigations at other locations with different geology can build.

Remote sensing, geological mapping and analysis of InSight observations (Golombek et al., 2017; Warner et al., 2017; Morgan et al., 2018; Golombek et al., 2020) shows that beneath a thin surficial layer of dust and sand is a layer of duricrust of variable thickness (≤10 cm) and a cohesion of a few to tens of kPa. This is underlain by a regolith of poorly-sorted, unconsolidated sand and rocks (Golombek et al., 2020). Beneath the landing site, the fine-grained, high-porosity impact generated regolith is ∼2 m thick (Lognonné et al., 2020) and is presumed (based on ejecta observations from nearby craters and a nearby scarp exposing a section of the subsurface) to grade with depth first into coarse, blocky ejecta and then over meters to tens of meters into fractured basalt flows (Golombek et al., 2017; Warner et al., 2017).

Seismic wave generation and near-field propagation will be most sensitive to changes in porosity, density and seismic velocity with depth. Initial seismic velocity estimates based on direct travel-time measurement of HP^3 mole hammering signals, and analysis of ground compliance, suggest a two-layer near-surface structure beneath the lander (Lognonné et al., 2020). The $\sim$ 2-m thick upper regolith has P-wave velocity $\sim$ 120 ms^{-1} and is underlain by a higher-impedance layer with P-wave velocity in the range 500-1500 ms^{-1} (Lognonné et al., 2020). For the meter-to-decameter scale impact craters of interest here, the wave generation region will be predominantly in the lower of these two layers. This study therefore adopts a one-layer target material model with a bulk density (ρ = 1589 kgm^{-3}), bulk porosity (ϕ = 44%), bulk sound speed (c_B = 857 ms^{-1}) and P-wave speed (c_P = 1088 ms^{-1}) that is likely representative of the upper tens of meters of Mars near InSight.

For simulations 1-3 with crater diameter $\leq$ 2 m, a material model with elastic moduli and seismic velocities closer to those of the shallowest subsurface would be the more appropriate. However, since the plastic and shock response of the target material is relatively insensitive to these material parameters, it is expected that the important nonlinear near-field effects, such as pore collapse and shear failure, are well described by the material model employed here. In the interest of consistency, the same target properties are used for all impact simulations, although these properties are most oversimplified for the three smallest impact scenarios. Although this

material is referred to here as regolith, it is emphasised that this material model approximates the bulk target stratigraphy from fine-grained regolith, through coarse ejecta to fractured basalt and not just the upper layer.

The target material strength is described with a simple pressure-dependent Lundborg strength model (Lundborg, 1968) with a shear strength of 5 kPa at zero pressure, an internal friction coefficient of 0.6 (approximately equivalent to a friction angle of 37° and a high-pressure shear strength limit of 250 MPa (Table 3.4). The $\epsilon-\alpha$ compaction model parameters that describe the crush behaviour of the target material were determined based on comparison of the Hugoniot curve of our simulated target material with crush data of analog target materials (granular pumice and quartz sand) and shock wave data for lunar regolith (Fig. 3.4).

To assess our simulation results' sensitivity to details of the target material crush curve we performed additional simulations with different ϵ-α model parameters. To achieve an effective crushing strength of ∼10 MPa we increased the value of ϵ_e to -1×10^{-2}, and kept other parameters for 'porous regolith' in Table 3.4 the same.

The simulations in Table 3.2, focusing on the first ms of the impact process, are significantly less computationally expensive. Hence, it is possible to adopt a wider range of target materials to investigate the response of the source time function to the target material. In total, three target material models are adopted: porous regolith (as described above), 25% porous fractured bedrock and non-porous bedrock (Rajšić et al., 2021). The analytical Tillotson equation of state for basalt (Tillotson, 1962) is used to describe the volumetric response of the target, combined with Lundborg strength model (Lundborg, 1968) in 'regolith', or ROCK strength model (Collins et al., 2004) in 'intact rock' and 'fractured rock'. The porous materials also include an $\epsilon - \alpha$ compaction model, with parameters specified in Table 3.4.

Table 3.4: Impactor and target material properties.

		Impactor	**Target**		
			Porous regolith	Fractured bedrock[b]	Intact bedrock[b]
Reference density [kgm^{-3}]	ρ_0	2860	1589	2150	2860
Bulk sound speed [ms^{-1}]	c_B	2598	857	1559	2598
Bulk modulus [GPa]	K_0	19.30	1.17	5.22	19.3
Shear modulus [GPa]	G_0	8.90	0.54	2.41	8.90
Poisson ratio	ν	0.3	0.3	0.3	0.3
LUNDD strength model parameters					
Internal friction coefficient	μ	0.7	0.6	-	-
Limiting strength [GPa]	Y_m	1	0.25	-	-
Cohesion [kPa]	Y_0	5	5	-	-
ROCK strength model parameters					
Internal friction coefficient (damaged)	μ_d	-	-	0.67	1.20
Limiting strength (damaged) [GPa]	Y_{dm}	-	-	0.17	3.5
Cohesion (damaged) [kPa]	Y_{d0}	-	-	0.2	10
Internal friction coefficient (intact)	μ_i	-	-	1.8	1.2
Limiting strength (intact) [GPa]	Y_{im}	-	-	0.17	3.5
Cohesion (intact) [kPa]	Y_{i0}	-	-	0.2	10
$\epsilon - \alpha$ **porosity model parameters**					
Initial distension	α_0	1.0	1.8	1.3	1.0
Initial porosity	ϕ_0	0	0.44	0.25	0
Elastic compaction threshold	ϵ_e	-	-2×10^{-4}	-4×10^{-4}	-
Transition distention	α_x	-	1.2	1.1	-
Exp. compaction rate	κ	-	0.98	0.98	-
Sounds speed ratio	χ	-	0.33	0.60	-

[a]Descriptions of material model parameters can be found in Collins et al. (2004), Wünnemann et al. (2006), and Collins et al. (2011).
[b]Material model derived in Rajšić et al. (2021).

3.2.3 Seismic source characterisation

The seismic source signature of the simulated impacts was characterised in simulation data post-processing. The next sections describe this methodology using the scenario of a 1-kg impactor striking the surface at $1.93\,\mathrm{kms}^{-1}$ (scenario 2 in Table 3.1).

3.2.3.1 Seismic moment

This study employed three scalar seismic moment calculation approaches, based on equations 2.13, 2.19 and 2.21. The theory behind each of the approaches is detailed in Chapter 2(Sec. 2.3.1).

The first approach is based on the analogy between an impact and an explosion. Here, the scalar moment was calculated at a given radial distance from the impact point using the residual radial displacement:

$$M_{1M}(R) = \left(K + \frac{4G}{3}\right) S(R) \left\langle D_R(R) \right\rangle , \tag{3.1}$$

where K and G are the (reference) bulk and shear moduli of the target material, respectively, $S(R) = 2\pi R^2$ is the surface area of a hemisphere of radius R, centred at the impact point, and $\langle D_R(R) \rangle$ is the average residual radial displacement of target material at radius R.

To calculate $\langle D_R(R, \theta) \rangle$ an array of Lagrangian probes was used (Fig. 3.2). The probes were positioned at regular intervals of radius R from the impact point and angle θ from vertical (note that the vertical and horizontal line of probes were shifted to the right and down, respectively, by a small amount to ensure that the probes were situated inside the computational domain, not on the boundary). These probes are indexed $i_R = 1 \ldots 10$ with increasing radius and $i_\theta = 1 \ldots 10$ in the azimuthal direction, from vertically down to horizontal.

Each probe's displacement in 2D cylindrical coordinates (d_r, d_z) was converted into displacement in the R and θ directions (d_R, d_θ). Radial displacements d_R as a function of time recorded by three Lagrangian probes are shown in Fig. 3.5. The residual radial displacement $D_R = d_R(\infty)$ for each of the probes was calculated at the time when the first impact-generated

stress wave reached the edge of the simulation domain. The mean residual radial displacement at a given range R was then computed by averaging the residual radial displacements at different azimuths $\langle D_R(R,\theta)\rangle$. The residual radial displacement at each azimuth was weighted by the fraction of $S(R)$ spanned by that azimuth. Section 3.2.3.4 details further how residual displacement was derived and used to constrain the elastic radius of impact.

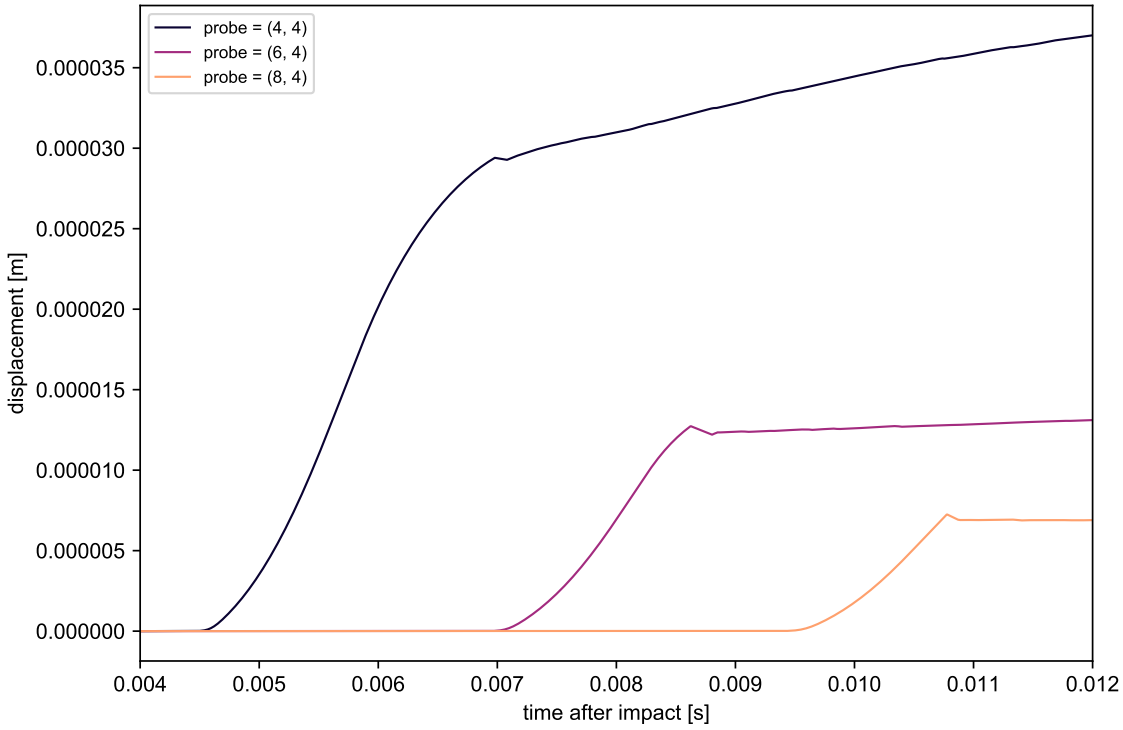

Figure 3.5: Radial displacements a function of time for three probes marked in Fig. 3.2.

The second method is based on an alternative definition of the seismic moment of an impact, proposed by Walker (2003). Here, the seismic moment in the horizontal direction was calculated as:

$$M_{rW}(t) = \frac{1}{2t}\sum_{i}^{n} \rho[i]\bar{v}_r[i]r[i]V[i], \tag{3.2}$$

where t is time after impact, $\rho[i]$ is material density in cell i, $V[i]$ is volume in cell i and $\bar{v}_r[i]$ is average (horizontal) radial velocity in cell i. Summation is over all n cells in the mesh, below the pre-impact target surface level; cells above the pre-impact surface were excluded, removing ejected material from the seismic moment calculation. $M_{rW}(t)$ was evaluated at the regular time intervals, at which mesh data were saved.

The third and final approach for computing the seismic moment of an impact is based on approximation of an impact as a point force density (Lognonné et al., 2009; Gudkova et al., 2011). In this approach, the vertical seismic moment is calculated as:

$$M_{zGL} = c_P p_z = c_P \sum_{i}^{n} \rho[i]\bar{v}_z[i]V[i], \tag{3.3}$$

where this summation is over the same target cells as above; $\bar{v}_z[i]$ is the average vertical velocity in cell i.

For the example simulation, plotting $M_{zGL}(t)$ and $M_{rW}(t)$ as a function of wave front radius $R = c_P t$ for comparison with $M_{1M}(R)$ shows that each measure of the seismic moment converges at ∼8 m (Fig. 3.6) as the wave transitions from plastic to elastic deformation. The seismic moment derived from residual displacement at radius R, $M_{1M}(R)$, converges to the true scalar seismic moment from above; the other two estimates of seismic moment converge to their final values from below (Fig. 3.6).

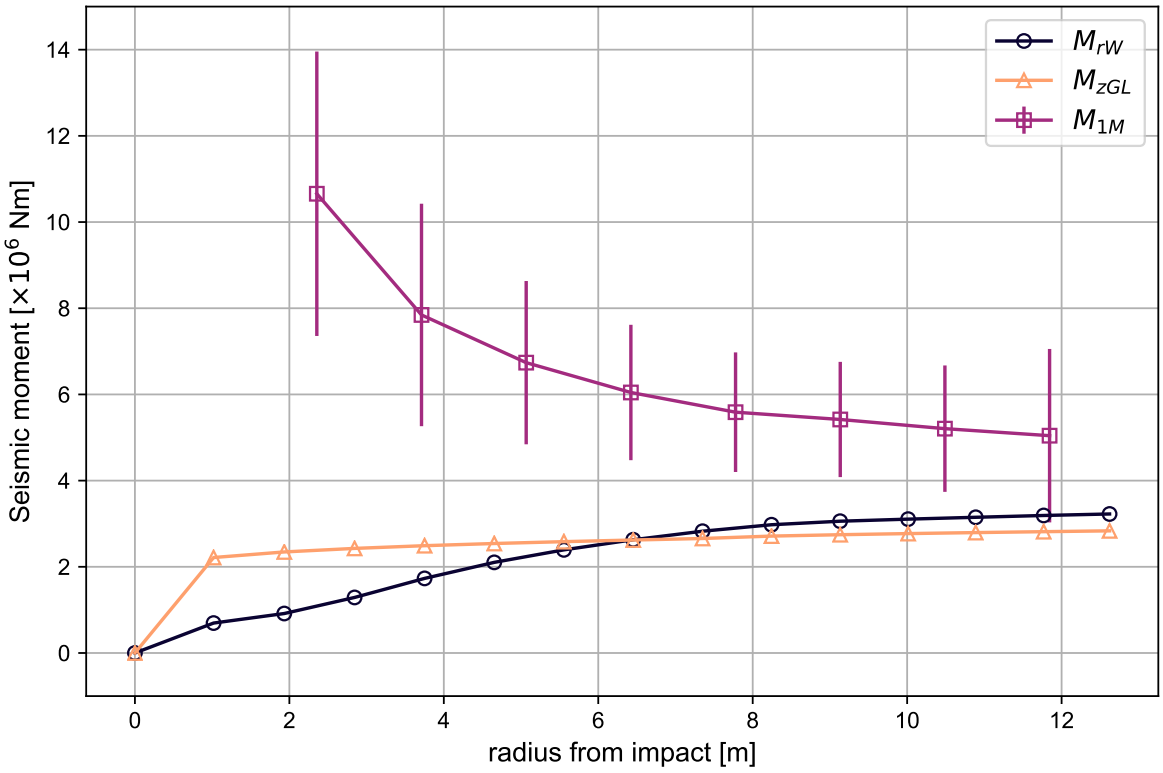

Figure 3.6: Three seismic scalar moment estimates as a function of radius from impact for a nominal model of a 1-kg impactor striking the target at 1.93 kms^{-1}.

The three estimates of the scalar seismic moment are consistent within a factor of two. M_{zGL} and M_{rW} are close to being within the uncertainty in M_{1M} that is attributed to the polar variation in residual radial displacement. The difference between M_{1M} and the other two estimates is likely due to oversimplification of our assumption that the fracture surface (elastic limit) is hemispherical.

3.2.3.2 Sphericalness of source

The ratio of the horizontal (M_{rW}) to vertical (M_{zGL}) seismic moment components provides a measure of source sphericalness. This parameter is denoted here as γ. For the example scenario presented in this section, γ is only slightly greater than one, implying an almost isotropic P-wave source.

3.2.3.3 Ejecta amplification factor

The vertical momentum transferred to the target p_z, calculated in the process of determining M_{zGL} can also be used to determine S, the amplification factor describing the vertical momentum transfer enhancement of the ejecta:

$$S = \frac{p_z}{p_i} = \frac{M_{zGL}}{c_P}, \tag{3.4}$$

where p_i is impactor momentum. For the example simulation, $S \approx 1.3$ implying a 30% enhancement of momentum transfer from ejecta, consistent with the semi-empirical approximation of Lognonné et al. (2009). Note, however, that the calculated values of S, p_z and M_{zGL} are sensitive to the approach used to exclude ejected momentum from the integral of momentum density over the target. For simplicity, this study assumes all material above the pre-impact level is ejecta. Moving this threshold altitude up or down by one impactor radius changes p_z and its dependencies by ∼15%.

3.2.3.4 Elastic radius

Because the $M_{rW}(t)$ moment converges at a radial distance between the other moments, the M_{rW} convergence distance can be used as a proxy for the elastic radius R_e. As $M_{rW}(R)$ is an average moment over all polar angles at R, our estimate of R_e is also an average over all polar angles and therefore this work assumes a hemispherical geometry for the elastic limit. On the other hand, the fact that the vertical moment M_{zGL} converges at a smaller radius than the horizontal moment suggests that the elastic radius may in fact be smaller in the vertical direction than in the horizontal. Such a geometry is consistent with the inferred extent of fracturing at Meteor crater, for example, but is inconsistent with the deep and narrow geometry of the elastic limit assumed by Shishkin (2007).

To verify the above, moment-based, proxy for the elastic radius for the example impact radial displacement-time paths recorded by probes at different radii from the impact are compared. The normalised displacement time paths are self-similar in the elastic region, as expected. Hence, in all further simulations this proxy is used to approximately delimit the elastic region and derive the scalar seismic moment of the impact for each method by averaging values of each moment in the elastic region ($R > R_e$).

The radial displacement-time paths recorded by each probe were also used to confirm the zones of elastic and plastic deformation. To facilitate comparison between displacement recorded at each probe, the radial displacement is normalised by the radial displacement at the end of the simulation. The time is converted into a normalised retarded time, τ (Shishkin, 2007):

$$\tau = \left(t - \frac{R}{c_P} \right), \tag{3.5}$$

where t is the time after impact and R is the radial distance of the probe. In this space, and away from the target surface, elastic and plastic deformation is clearly distinguishable (Fig. 3.7). First motion times at all probes are consistent with a P-wave speed close to c_P. Displacement records near the surface are more complex and were excluded to facilitate measurement of the elastic radius. Probes in the plastic region (red in Fig. 3.7) record a displacement that increases

continuously with time and is still growing at the simulation end time, whereas probes in the elastic region (blue in Fig. 3.7) record a rapid initial displacement that then stops before the simulation end time, in some cases following a small rebound. In the example case, the plastic-elastic transition occurs between the probes indexed $i_R = 6$ and 7, implying an elastic radius of ≈ 8.5 m (illustrated in Fig. 3.7b), which is consistent with the convergence of $M_{rW}(t)$ and $M_{1M}(R)$.

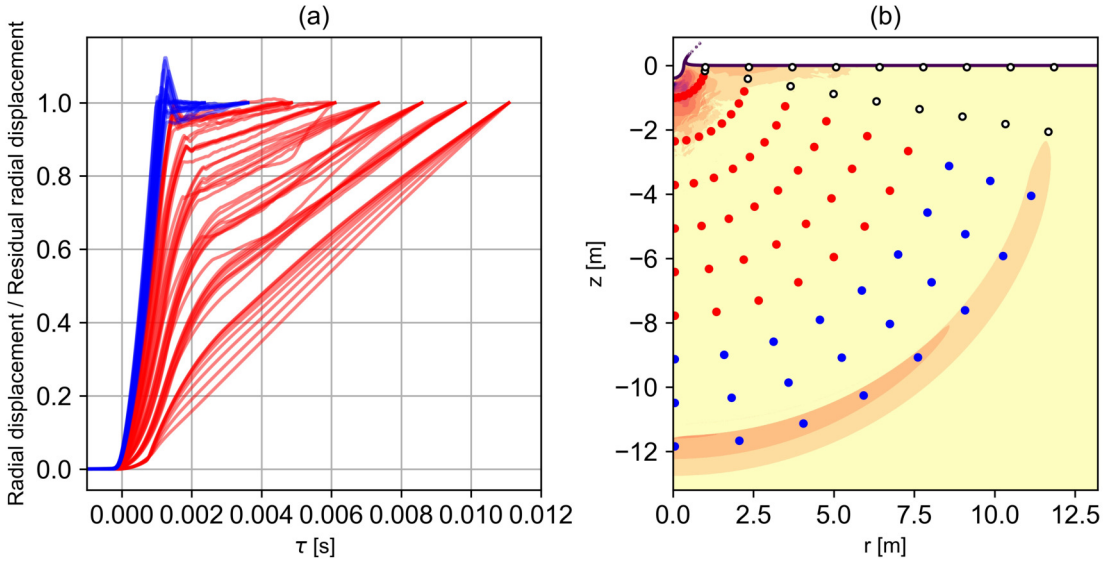

Figure 3.7: (a) Radial displacement normalised by residual radial displacement as a function of retarded time for probes below the surface. Red lines show data for probes interpreted to be in the zone of plastic deformation (highlighted in red in (b)). Blue lines are data for probes interpreted to be in the zone of elastic deformation (blue in (b)). (b) zones of plastic (red) and elastic (blue) deformation used to define the elastic radius, R_e. Near-surface probes omitted from the analysis of the elastic radius are shown in white.

3.2.3.5 Seismic energy and seismic efficiency

To calculate the energy radiated from the impact as seismic waves E_s, closely following Güldemeister and Wünnemann (2017), this study employed the triangular pulse approximation (equation 2.25), to estimate the time integral of the power transferred to the target by the passage of the stress wave at each Lagrangian probe (Fig. 3.2). When applying equation 2.25, P_{max} is defined as the peak pressure recorded by the probe, Δt is the full width at half maximum of the pressure pulse, R is the (spherical) impactor-probe radial distance; ρ and c_P are the reference density and P-wave speed of the pristine target material, respectively. Three example pressure traces are shown in Fig. 3.8b, including peak pressures and half-widths.

To calculate wave energy at each radius R, wave properties were measured for each probe at that radius and averaged across polar angles, weighted by the area of the hemisphere spanned by that angle. Calculated this way, wave energy converges at $\sim R_e$, consistent with the previous section. Hence, to calculate the radiated seismic energy and seismic efficiency with this approach, E_s is defined as the average E_W at probes with $R > R_e$, and k_s as E_s/E_i. Although the energy losses are greatest in the first 2 m from the impact site, the elastic radius in the target extends well beyond the crater rim.

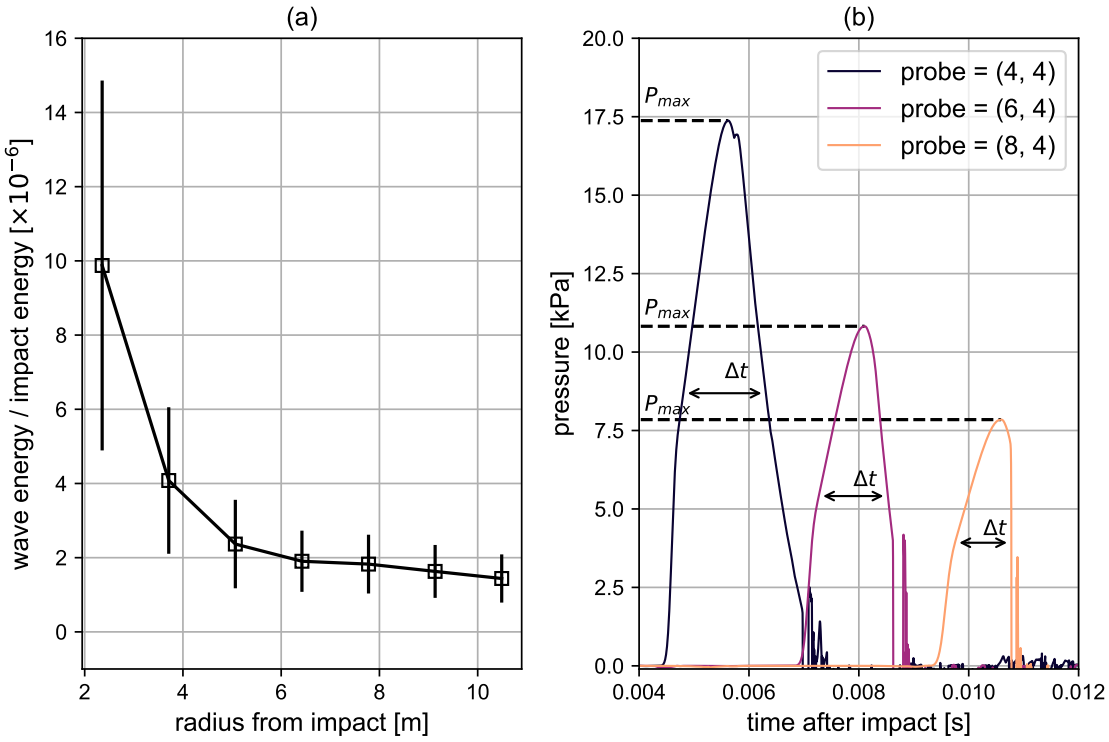

Figure 3.8: (a) Ratio of wave energy and impact energy as a function of radius from impact for a nominal model of a 1-kg impactor striking the surface at 1.93 kms^{-1}. (b) Pressure recorded as a function of time by three probes highlighted in Fig. 3.2. Black dashed lines mark peak pressure values used in equation 2.25 and the half-width, dt, of each trace is also marked.

3.2.3.6 Source time function

The vertical source time function is calculated in post processing for all simulations in Table 3.2, which comprise a smaller domain and a duration of 1 ms after impact. The force pulse is computed, following Lognonné et al. (2009), by firstly evaluating the following sum (a discrete version of equation 2.22):

$$p_z = \sum_{i}^{n} \rho[i] v_z[i] V[i] \tag{3.6}$$

where $\rho[i]$ is the target density in target cell i, $v_z[i]$ is the vertical velocity of material in the cell, and $V[i]$ is the volume represented by the cell. The summation is over n cells in the target below the pre-impact surface. Equation 3.6 is evaluated at every save time of the simulation, and combined into a single time series. Differentiating the time series with respect to time returns a force as a function of time. A time series showing momentum transferred and force at the source for the example impact scenario is shown in Fig. 3.9. The momentum transferred converges to a constant value at 1 ms, consistent with the result shown in Fig. 3.6 for a longer simulation of the same impact scenario. The oscillations seen as the numerical source time function decays can be attributed to the reverberation of the shock wave inside the impactor, which can be recorded at high temporal resolution. The peak force reached was $F_{max} = 2.1 \times 10^7$ N and the source duration was $\tau \sim 5 \times 10^{-4}$ s.

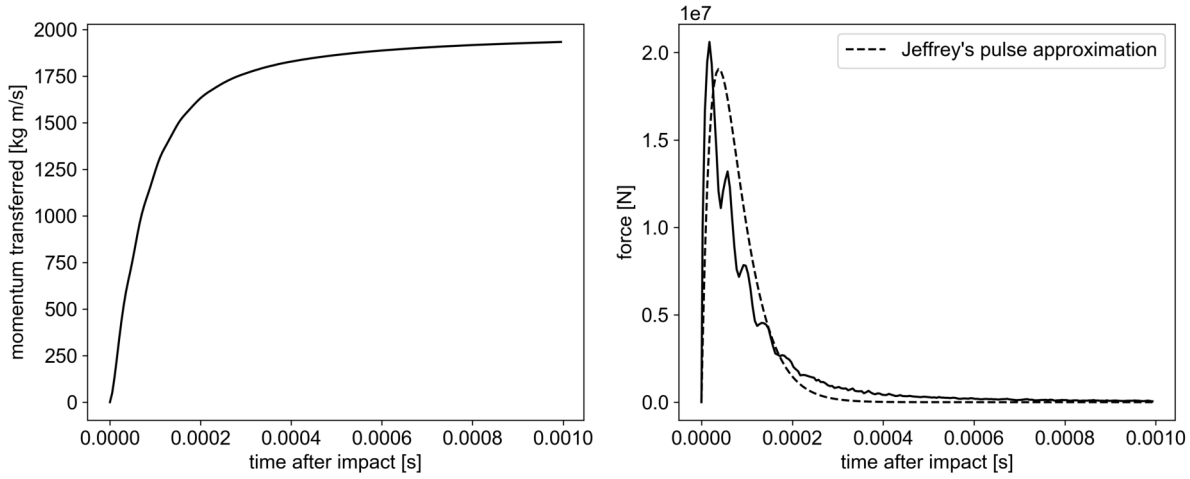

Figure 3.9: (left) Momentum transferred to the target as a function of time; and (right) the resulting source time function for an example impact scenario of a 1-kg impactor striking the surface at 1.93 kms^{-1} (scenario 2 in Table 3.1). A Jeffrey's pulse approximation of the source time function is shown as a dashed line.

As described in Chapter 2, the force pulse can be approximated with Jeffrey's pulse expression, which depends on two parameters: impact momentum and time constant α. Equation 2.27 was fitted to the numerical source time function using a least-squares approach, to find the optimal α. For the example scenario the value of α was $(2.61 \pm 0.06) \times 10^4$ s^{-1}, with an R^2 of 0.78, indicating a good fit. The Jeffrey's pulse approximation has a slightly shorter source duration ($\sim 3 \times 10^{-4}$ s) and lower peak force reached ($F_{max} = 1.9 \times 10^7$ N). Integrating the Jeffrey's pulse approximation recovers the numerical value of momentum transferred to within 4 %.

3.3 Results

The above analysis was performed on each of the simulated impact scenarios. The results characterise impacts as a seismic source for the range in impactor momentum expected to be typical of impacts that might be detected by InSight. Table 3.5 documents the various characteristics of the seismic source for each impact scenario.

Table 3.5: Complete results for wave generation models.

Simulation	p_i[kgm/s]	E_i[J]	M_{rW}[Nm]	M_{1M}[Nm]	M_{zGL}[Nm]	S	γ	k_s	E_s[J]	$R_e[r_i]$
1	7.00×10^2	4.73×10^5	1.09×10^6	1.86×10^6	9.61×10^5	1.26	1.14	1.97×10^{-6}	0.93	182
2	1.99×10^3	1.92×10^6	3.19×10^6	5.22×10^6	2.81×10^6	1.30	1.13	1.63×10^{-6}	3.13	200
3	4.50×10^3	5.63×10^6	7.18×10^6	1.00×10^7	6.39×10^6	1.31	1.12	1.40×10^{-6}	7.87	185
4	1.49×10^4	2.46×10^7	2.51×10^7	4.01×10^7	2.28×10^7	1.41	1.10	1.26×10^{-6}	30.85	209
5	2.43×10^4	4.42×10^7	4.08×10^7	6.68×10^7	3.74×10^7	1.42	1.09	1.18×10^{-6}	52.2	208
6	3.56×10^4	6.97×10^7	6.08×10^7	9.08×10^7	5.57×10^7	1.44	1.09	1.13×10^{-6}	78.6	216
7	5.17×10^4	1.07×10^8	8.67×10^7	1.45×10^8	7.94×10^7	1.41	1.09	1.00×10^{-6}	109	236
8	7.03×10^4	1.54×10^8	1.22×10^8	1.97×10^8	1.12×10^8	1.46	1.09	1.10×10^{-6}	168	242
9	9.51×10^4	2.16×10^8	1.66×10^8	2.79×10^8	1.52×10^8	1.47	1.09	9.64×10^{-7}	209	240
10	1.61×10^5	3.92×10^8	2.85×10^8	3.6×10^8	2.63×10^8	1.50	1.08	9.42×10^{-7}	369	222
11	4.45×10^5	1.20×10^9	7.74×10^8	1.32×10^9	7.33×10^8	1.51	1.06	8.75×10^{-7}	1050	224
12	1.75×10^6	5.19×10^9	3.17×10^9	5.28×10^9	2.94×10^9	1.54	1.08	8.26×10^{-7}	4290	245
13	9.08×10^6	2.9×10^{10}	1.65×10^{10}	2.66×10^{10}	1.54×10^{10}	1.56	1.07	9.24×10^{-7}	26800	242

3.3.1 Seismic moment

The simulations performed in this study show that each estimate of the scalar seismic moment is linearly proportional to impact momentum (Fig. 3.10). $M_{1M} \approx 2 \times M_{rW}$ for all impact momenta. The difference between M_{1M} and M_{rW} can be partially attributed to the polar variation of residual radial displacement. In order to deduce overall trends in seismic moment with impact properties, seismic moment values resulting from the three methods, including respective errors, were combined to produce a single data-set. Using a least squares regression, a best-fit relationship between seismic scalar moment M_1 (Nm) and impact momentum p_i ($\mathrm{kg\,ms^{-1}}$) is:

$$M_1 = 10^{3.18 \pm 0.08} p_i^{1.02 \pm 0.01}. \tag{3.7}$$

Pearson's R value for this relationship is 0.997, indicating good data fit.

Values calculated from our simulations agree very closely with the theoretical GL model (shown

in Fig. 3.10). For the purposes of this comparison, the GL model assumed $\eta = 0.3$, as adopted in Daubar et al. (2018) and Lognonné et al. (2009).

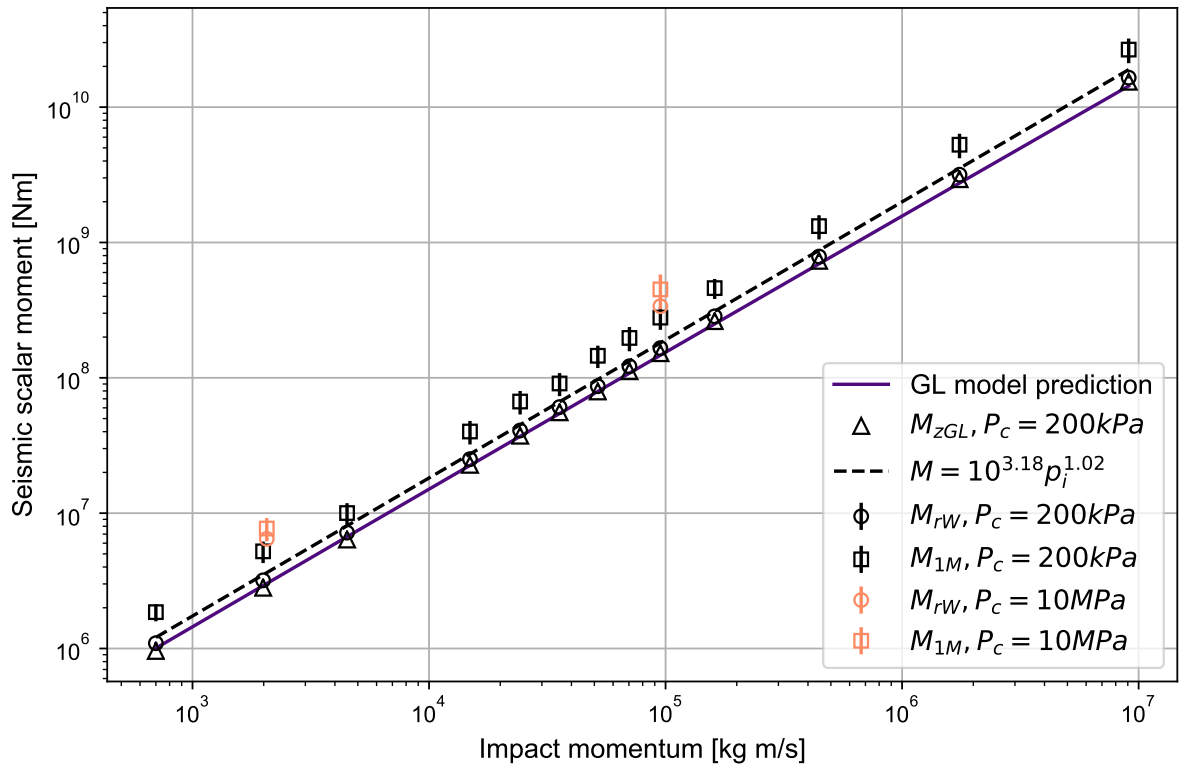

Figure 3.10: Three scalar seismic moment estimates for all simulations as a function of impactor momentum. Solid line: GL model seismic moment prediction, assuming $\eta = 0.3$ (following Lognonné et al., 2009) and $c_P = 1088\,\mathrm{ms}^{-1}$ (consistent with our target material model).

3.3.2 Sphericalness of source

For the simulated impact scenarios, γ, calculated as the ratio of M_{rW} to M_{zGL} (equation 2.20) was 1.05–1.15, implying an approximately isotropic seismic moment tensor for vertical impacts. The value of γ decreased with increasing impact momentum, as shown in Fig. 3.11. The vertical component of the moment tensor is only 5–15% smaller than each of the radial components. Because the simulations in this work were restricted to vertical impacts, future work should explore if these results extend to oblique impacts.

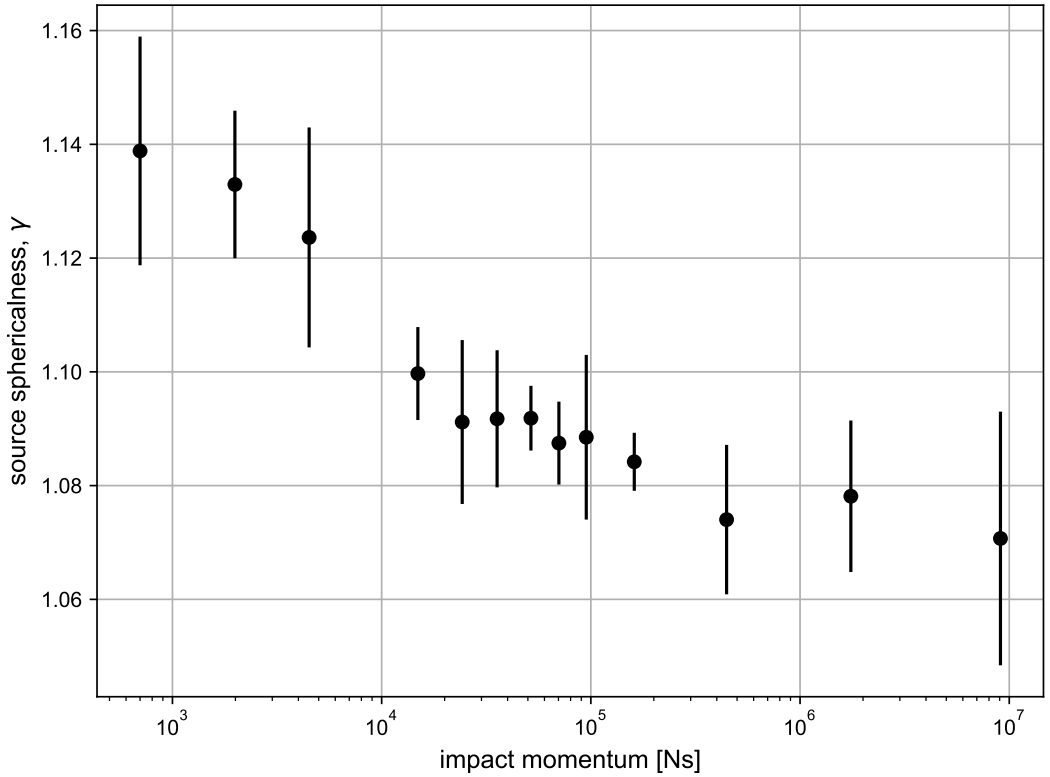

Figure 3.11: The sphericalness of source as a function of impact momentum, for the suite of vertical impacts on Mars simulated in this chapter.

3.3.3 Ejecta amplification factor

As shown in the previous sections, M_{zGL} is proportional to the vertical momentum transferred to the target by the impact (Lognonné et al., 2009; Gudkova et al., 2015). Previous work has shown that momentum transferred to the ground is amplified by material ejected from the crater (McGarr et al., 1969), with amplification extent dependent on impactor and target properties (McFadden, 2005; Raducan et al., 2019). The amplification is characterised by the ejecta amplification factor S. NB in many previous studies, β is used to denote the ejecta amplification factor. S is used here for consistency with the GL model (Lognonné et al., 2009). For the small impacts on Mars simulated here, S increases with impact momentum from 1.25 to 1.6 (Fig. 3.12). These values are comparable to amplification factors derived from ejecta scaling relationships and used in previous estimates of the impulse applied to the ground by

impacts (Lognonné et al., 2009). Higher momentum impacts exhibited lower values of γ but a higher S, so were more isotropic while more momentum was being imparted to the ground.

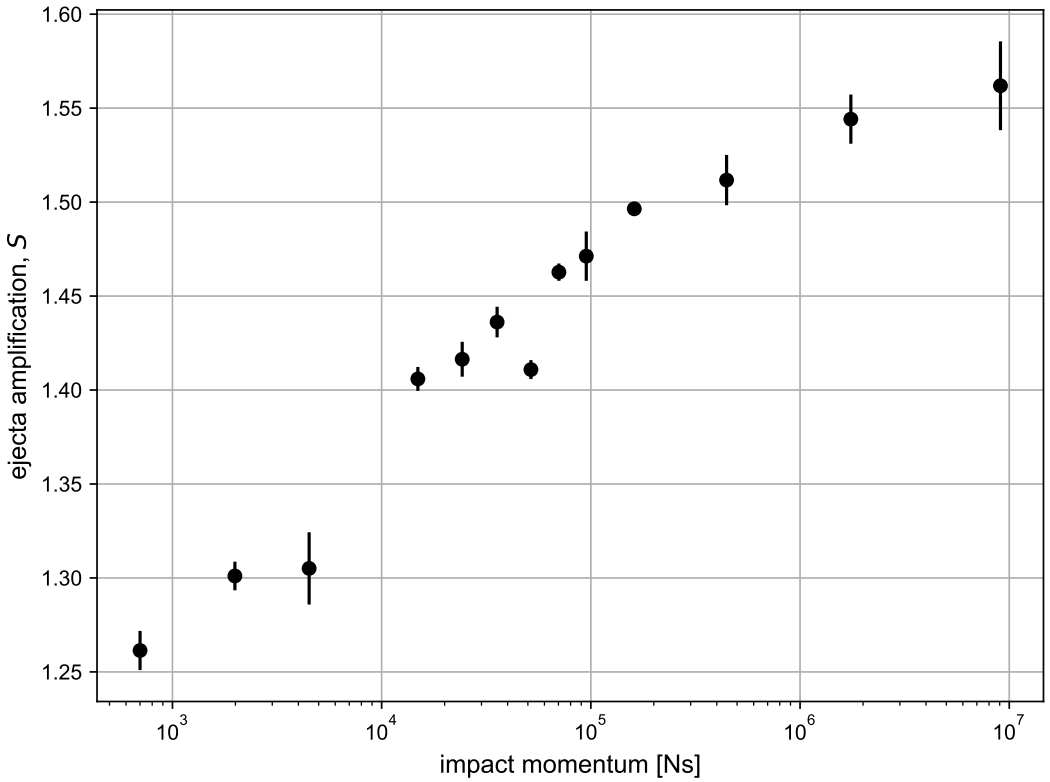

Figure 3.12: Ejecta amplification factor as a function of momentum for the impact scenarios simulated.

3.3.4 Elastic radius of small impacts on Mars

Based on convergence of M_{rW}, the average radius of the plastic-elastic regime transition over all polar angles, R_e, increased with impact momentum from R_e ≈180–240 impactor radii (Table 3.5). This corresponds to 7-11 crater radii, depending on crater scaling assumptions (Fig. 3.1). The elastic radius analysis based on Lagrangian probes displacement was repeated for each model to verify the elastic radius R_e for each impact scenario determined from the convergence of M_{rW}. The resulting elastic radii values were self-consistent.

This is substantially larger than the elastic radius equal to the crater radius assumed in the

analytical model of seismic wave generation of Shishkin (2007), and as suggested by observations of terrestrial craters (Ackermann et al., 1975; Smith et al., 1999), which found the fracture radius of ∼2–2.5 crater radii. We attribute this difference to the difference in strength between target material used in our simulations (∼ 5kPa) and typical terrestrial rocks (∼ 10MPa). For the very weak material in our simulations, the wave must decay to a lower amplitude, which occurs at a further distance. Hence this estimate will vary for craters formed in areas with different target properties than in simulations in this work. Additionally, the elastic radius determined in this work may be overestimated, due to the absence of overburden pressure in our simulations.

If the characteristic timescale of seismic wave generation is the time taken for the impact stress wave to reach the elastic radius (Gudkova et al., 2015), this implies a wave-generation timescale $\approx 10R_c/c_P$, where R_c is crater radius and c_P is P-wave velocity.

3.3.5 Seismic efficiency

The seismic efficiencies of impact simulated in this chapter are at the low end of previous estimates (Fig. 3.13). They are substantially lower than seismic efficiencies measured in laboratory-scale impact experiments in sand (McGarr et al., 1969; Richardson and Kedar, 2013) and those based on missile impacts on Earth (Latham et al., 1970b). The resulting values are comparable to estimates based on large scale artificial impacts on the Moon (Latham et al., 1970a), which represent good analogs to those simulations in terms of impactor momentum and energy, and target properties. However, it must be acknowledged, that the impactors in the artificial lunar impacts were low density, easily crushed, metal spacecraft. Such impactors are poor analogs to strong, rocky meteorites used in simulations in this study. Further research is necessary to determine the effect of individual impactor properties on seismic efficiency.

The simulations in this chapter reveal the seismic efficiency of small impacts is also much smaller than estimates produced in laboratory experiments of impacts in porous rocks and iSALE simulations of those experiments (Güldemeister and Wünnemann, 2017). The difference in k_s between this work and that of Güldemeister and Wünnemann (2017), which used a similar modelling approach, is attributed to the dramatically different properties of assumed target material, in particular the effective crushing strength $p_c \approx -K_0\epsilon_e$. Here, the martian soil was represented with a crushing strength (the onset of permanent compaction) of ∼200 kPa, based on the crushing behaviour of analog materials (Fig. 3.4); the rock targets of Güldemeister and Wünnemann (2017) were represented with a crushing strength of ∼700 MPa.

Additional simulations performed with different crush curve parameters showed that for a simulation with an effective crushing strength of ∼10 MPa, more appropriate for a soft rock, the seismic efficiency was two orders of magnitude larger (Fig 3.13). Seismic moment in those simulations was only 3× larger. While a more thorough investigation of the effect of target crushing strength and other material properties on seismic efficiency is required, this suggests that the detectability of small impacts on Mars might be very sensitive to the proximity to the surface of dense, strong and high impedance materials.

The seismic efficiency values from impact simulations in this chapter decrease slightly with increasing impact energy and impact velocity. This likely reflects the fact that at higher impact speeds more energy is partitioned into waste heat.

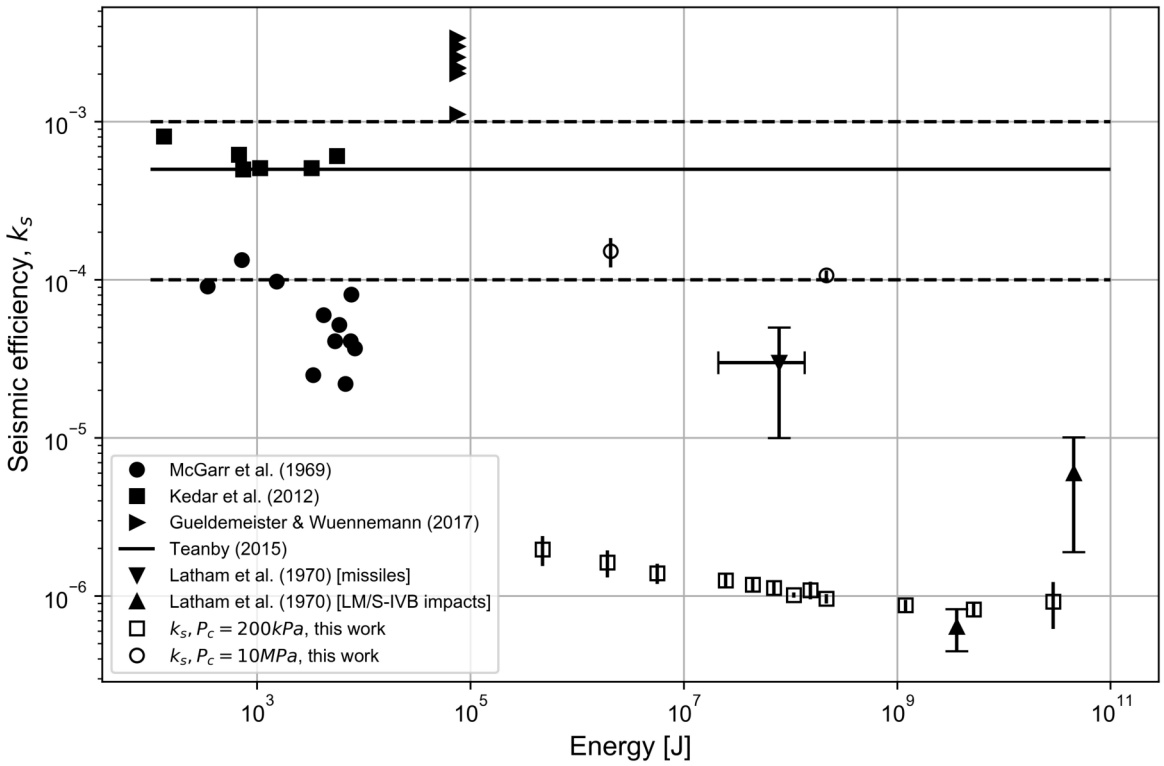

Figure 3.13: Seismic efficiency as a function of impact energy. Our results fall between 8×10^{-7} and 2×10^{-6}, approximately two orders of magnitude below pre-landing predictions. To illustrate the sensitivity of seismic efficiency to the crush curve parameters, a result for a simulation using crushing strength of 10MPa is also shown at 1–2 $\times10^{-4}$. (Note that the vertical bars on the results represent the error bars, for some simulation smaller than the size of the marker.) Data obtained in previous studies, numerical (Güldemeister and Wünnemann, 2017) and experimental (Latham et al., 1970b; Latham et al., 1970a; McGarr et al., 1969; Richardson and Kedar, 2013), are also presented.

3.3.6 Source time function

Table 3.6: Complete results for impact source models. The subscript indicates which parameter was changed in the particular simulation.

Simulation	p_i[kgm/s]	E_i[J]	F_{max} [N]	α [s^{-1}]	t_c [s]
2	2.0×10^3	1.9×10^6	1.91×10^7	26062 ± 667	5.45×10^{-5}
2_{v1000}	1.0×10^3	5.2×10^5	5.65×10^6	14908 ± 386	1.06×10^{-4}
2_{v3000}	3.1×10^3	4.6×10^6	4.53×10^7	40049 ± 927	4.60×10^{-5}
2_{v4000}	4.1×10^3	8.2×10^6	8.03×10^7	53114 ± 1112	3.68×10^{-5}
$2_{r0.082}$	1.3×10^4	1.2×10^7	6.62×10^7	13986 ± 360	1.20×10^{-4}
$2_{r0.12}$	4.0×10^4	3.9×10^7	1.42×10^8	9570 ± 174	1.76×10^{-4}
$2_{r0.49}$	2.7×10^6	2.6×10^9	2.41×10^9	2353 ± 35	7.19×10^{-4}
$2_{\text{fractured bedrock}}$	2.0×10^3	1.9×10^6	3.48×10^7	47679 ± 1003	5.55×10^{-5}
2_{bedrock}	2.0×10^3	1.9×10^6	4.78×10^7	66161 ± 449	4.35×10^{-5}
5	2.4×10^4	4.4×10^7	2.32×10^8	26018 ± 569	7.38×10^{-5}
$5_{\text{fractured bedrock}}$	2.4×10^4	4.4×10^7	3.67×10^8	43297 ± 674	6.91×10^{-5}
5_{bedrock}	2.4×10^4	4.4×10^7	4.35×10^8	48940 ± 185	6.20×10^{-5}
9	9.5×10^4	2.2×10^8	7.74×10^8	22174 ± 449	9.06×10^{-5}
$9_{\text{fractured bedrock}}$	9.5×10^4	2.2×10^8	1.15×10^9	35272 ± 481	8.69×10^{-5}
9_{bedrock}	9.5×10^4	2.2×10^8	1.33×10^9	37930 ± 177	8.07×10^{-5}
13	9.1×10^6	2.9×10^{10}	2.50×10^{10}	7500 ± 97	2.81×10^{-4}
$13_{\text{fractured bedrock}}$	9.1×10^6	2.9×10^{10}	2.81×10^{10}	9120 ± 98	2.78×10^{-4}
13_{bedrock}	9.1×10^6	2.9×10^{10}	3.58×10^{10}	11364 ± 76	2.69×10^{-4}

Table 3.6 lists complete results for the short source simulations. The source time function was calculated and fitted with Jeffrey's pulse approximation for each simulation in Table 3.2. Jeffrey's pulse was found to be a generally good fit for the impact scenarios simulated, with R^2 values ranging: 0.57 - 0.99. To support this claim, the relationship between peak force F_{max} (approximated by Jeffrey's pulse) exerted during impact and impact momentum $\times\alpha$ was tested, where the proportionality constant was found to be only 5% smaller than that predicted theoretically (Fig. 3.14).

As described in Section 3.2, only one of the impactor size, velocity, impact momentum and target material was varied in every simulation, with remaining parameters kept constant. The peak force exerted on the impact site increased with increasing impact momentum, impactor size and impact velocity. Impacts onto weaker, porous targets exerted lower peak force on the impact site.

The effects of individual impact properties are shown in Fig. 3.15. The Jeffrey pulses in this plot

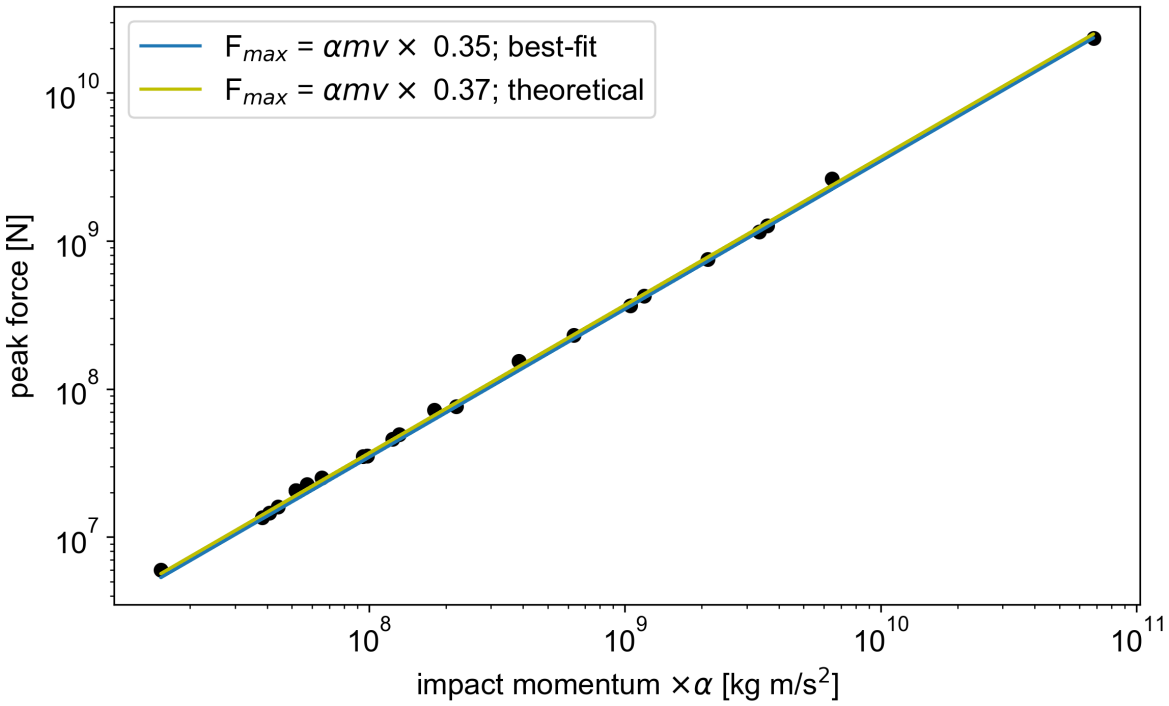

Figure 3.14: The theoretical relationship between peak force exerted during impact F_{max} and impact momentum $\times\alpha$ (green line), compared with our simulation results (black points). A least-squares fit through our results (blue line) gives a proportionality constant of 0.35, only 5% smaller than predicted theoretically.

have been normalised by the peak force of each model to highlight the differences in pulse width. The duration of the pulse increased with increasing impactor size (Fig. 3.15c) and decreasing impact velocity (Fig. 3.15b). For scenarios where both impactor size and velocity were increased (increasing momentum) the duration of the source increased (Fig. 3.15a), implying that the impactor size has the dominant effect on the duration. For stronger and less porous target materials the source time function exhibited shorter duration (Fig. 3.15d).

The main advantage of approximating each pulse with Jeffrey's pulse is its simple two-parameter form. Furthermore, the α parameter can be related to other known impact properties. Because α determines the width of the source time function, it can be considered a measure of the seismic source timescale of the impact process. It follows that it should be inherently related to one of the important timescales in the cratering process. As shown in Fig. 3.16, for the range of scenarios considered in this study, α scales best with the contact and duration timescale of the impact process, t_c, defined here as the time taken for the shock-wave travelling at speed U

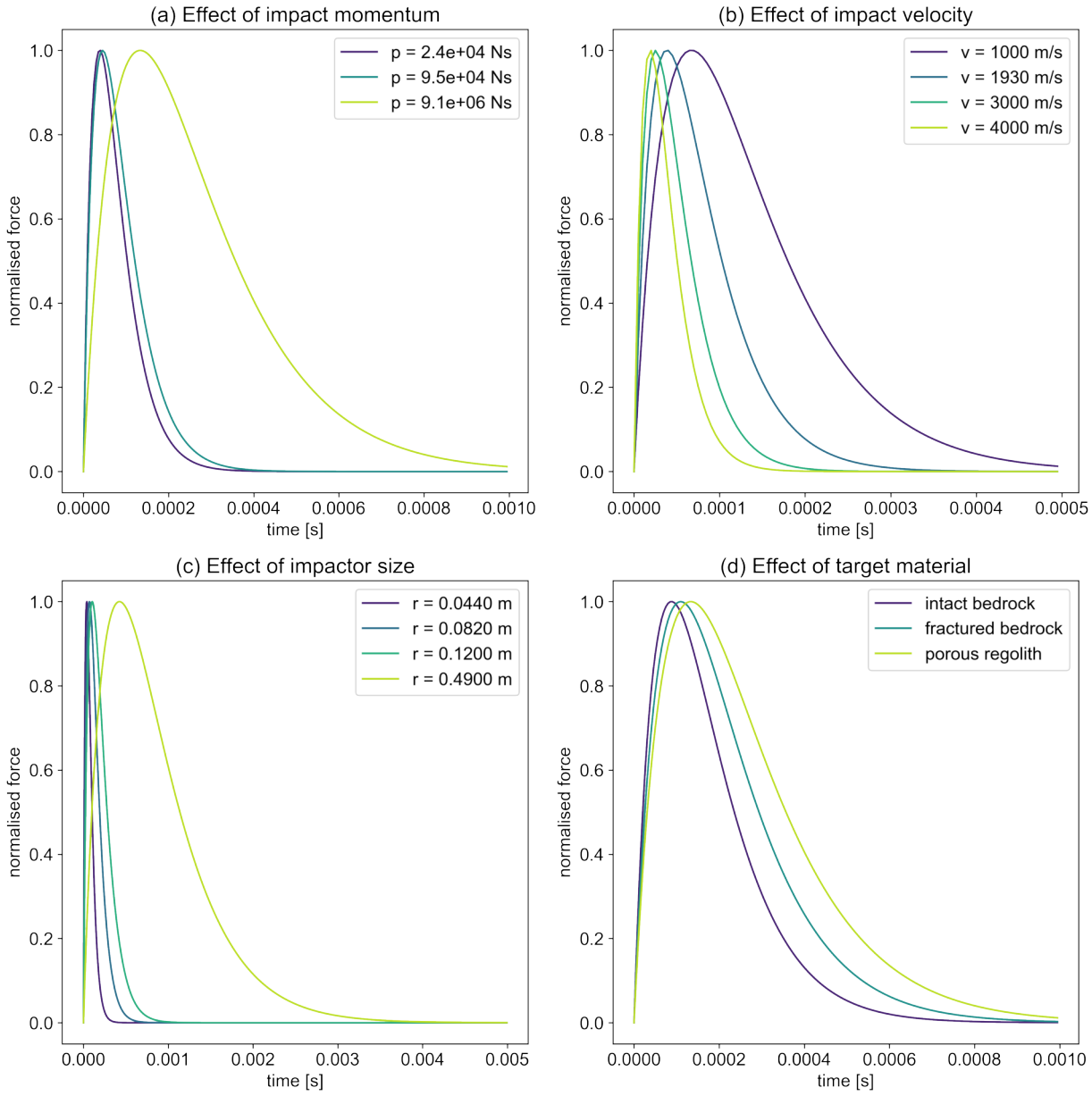

Figure 3.15: Jeffrey's pulse approximations for impact simulations onto a martian surface, showing the effects of impact properties investigated: (a) impactor momentum, (b) impact speed, (c) impactor radius, (d) target material properties. The magnitudes have been normalised by the peak force reached in each model.

in the target material, to travel twice the impactor diameter ($t_c = 2D/U$). The least squares scaling relation is:

$$\alpha = 10^{-0.42\pm0.15} t_c^{-1.20\pm0.04}, \tag{3.8}$$

with an R^2 value of 0.81. Combining this with Jeffrey's pulse expression (equation 2.27) gives:

$$F_z = (10^{-0.42} t_c^{-1.20})^2 p_i t e^{10^{-0.42} t_c^{-1.20} t}, \tag{3.9}$$

which now only depends on physical impact properties of the scenario in question.

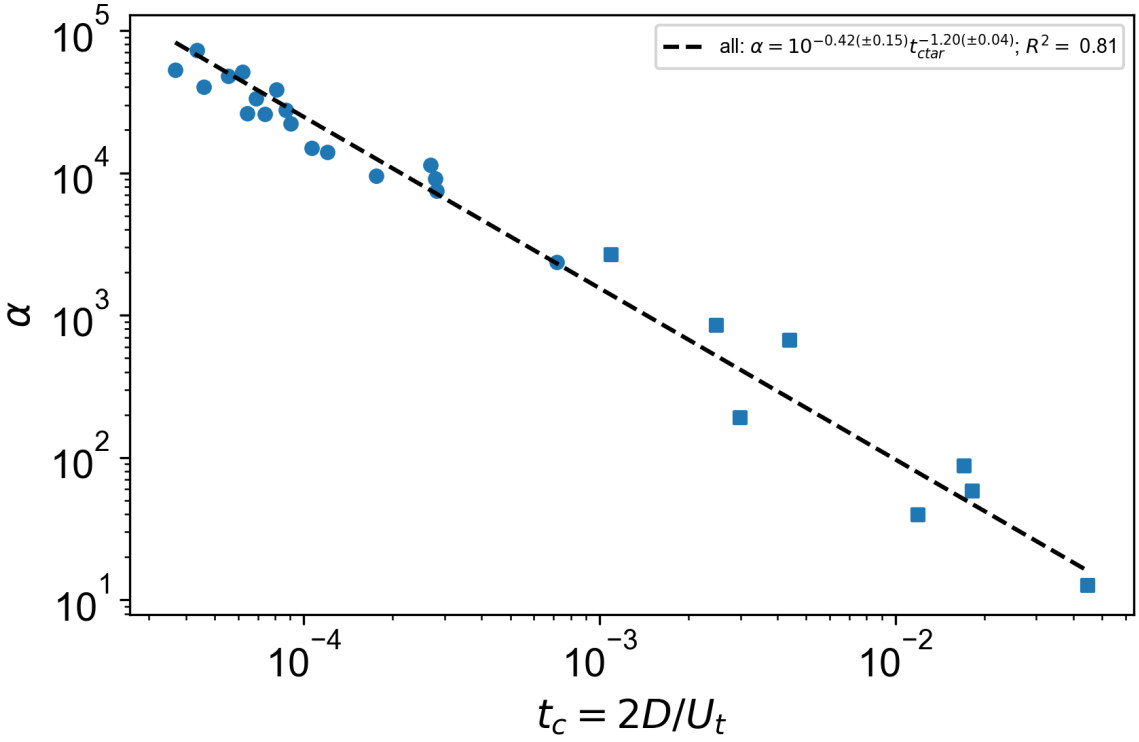

Figure 3.16: Values of α calculated for each simulation in this chapter, as a function of the contact and compression timescale t_c. Results from simulations of impacts onto martian surface are marked with blue dots, and results from impacts onto asteroids are marked with blue squares. The least squares relationship is shown with the dashed line.

The source durations computed in this study are of the same order of magnitude as the results of an experimental study of Richardson and Kedar (2013). A series of high velocity impacts was performed at NASA Ames Vertical Gun Range (AVGR). The impact velocities in the experiments ranged between 1–6 kms^{-1}, which is comparable with impact velocities simulated in this chapter, whilst the pyrex glass impactor masses were significantly lower than those simulated here. As shown in Daubar et al. (2018) for an impact at 1000 ms^{-1} the source duration is approximately 10^{-3} s, which is comparable with duration of impact scenario 2_{v1000}, in spite of significantly smaller impactor than that used in the iSALE simulations. This could reflect the vastly different material properties of the impactor and target. The source durations measured here are also significantly shorter than pre-landing estimates suggested Daubar et al. (2018).

3.4 Implications for InSight

The simulation results presented in this chapter show a linear relationship between impact momentum and seismic moment (and therefore ground motion amplitude). The following section evaluates the implications of this result for impact detectability at InSight.

The expected number of detectable impacts has been estimated in several ways (Teanby and Wookey, 2011; Teanby, 2015; Daubar et al., 2015; Lognonné and Johnson, 2015; Daubar et al., 2018). Teanby and Wookey (2011) estimated detectable impact numbers by combining seismic wave-form modelling, observed cratering rates and an empirical relationship between crater size and seismic moment (Fig. 3.17a). This empirical scaling relationship relies on three elements: an empirical relationship between crater size and impact energy, based largely on terrestrial explosion data (Fig. 3.17b), the seismic efficiency of the impact, and a relationship between radiated seismic energy and seismic moment, based on small earthquake and nuclear explosion data (Fig. 3.17c). The results of simulations in this chapter provide an independent test of these elements.

The radiated seismic energy E_s and scalar seismic moment M_1 determined from our simulations is fit well by a linear relationship with a constant of proportionality of 1×10^{-6}. Assuming $\sigma_s = 5$ kPa and $G = 0.54$ GPa, this implies that for impacts the constant c in equation 2.17 is $\approx$0.1, which is lower than commonly assumed for earthquakes (0.54) and explosions (0.27) (Shishkin, 2007). When combined with earthquake and explosion data, our simulation results follow a power-law trend akin to the Teanby and Wookey (2011) model (TW2011, hereafter). In the most relevant range of seismic energy ($1 - 10^5$ J) the seismic moment predicted by the TW2011 model is 2-3 times that predicted by our simulations (Fig. 3.17c). To convert between seismic energy and impact energy, TW2011 adopted a seismic efficiency of $k_s = 2 \times 10^{-5}$, $\sim$20 times higher than determined here for the weak, porous surface of Mars near InSight. When combined with the difference in E_s-M scaling, this results in TW2011 overestimating seismic moment by a factor of 40-60 for the same size crater.

Although the relationship between impact energy and crater size was not explicitly tested

here by the iSALE simulations, previous work has shown consistency between the π-group scaling of crater diameter used here and iSALE simulations of crater formation in regolith-like targets (Prieur et al., 2017; Raducan et al., 2019). For the impactor parameters adopted here, which account approximately for deceleration during atmospheric entry, the scaling relationship between crater size and impact energy used in TW2011 agrees reasonably with our results for craters of diameter >10 m, but overestimates the impact energy required to produce smaller craters by up to an order of magnitude (Fig. 3.17b).

When all components of the crater size to seismic moment scaling relationship are combined, TW2011 predicts a seismic moment 1–2 orders of magnitude higher for a given crater size than our results. We attribute this difference to a combination of the low seismic efficiency of impacts into very weak porous regolith shown by our results and the previous work's extrapolation of experimental data based on impact energy as opposed to impact momentum. As discussed in Daubar et al. (2018) an important consideration for reconciling these disparate estimates of seismic moment is the effect of target material properties and transmission of seismic energy into bedrock underlying the impacted material. Also shown in Fig. 3.17a are estimates of seismic moment vs crater rim diameter derived using the GL model and the Shishkin model (as described by Daubar et al., 2018) that include a total bedrock moment correction factor of ≈ 5 to account for the effect of a typical crustal bedrock ($c_P = 1000\,\mathrm{ms}^{-1}$, $\rho = 2700\,\mathrm{kgm}^{-3}$) underlying soft impacted regolith ($c_P = 330\,\mathrm{ms}^{-1}$, $\rho = 1500\,\mathrm{kgm}^{-3}$). These lie between our simulation estimates in a regolith analog that do not include a bedrock correction and those of TW2011, based in part on data from explosions and impacts directly into bedrock.

For a nominal noise model, Teanby and Wookey (2011) estimated a total impact-generated seismicity of $10^{13} - 10^{14}$ Nm per Earth year, and one detectable teleseismic range impact every 10 years. Based on the much lower seismic moments predicted by this work, the TW2011 predictions at the lower end of their estimates seem the most likely. These imply a total impact-generated seismicity of $10^{11} - 10^{13}$ Nm and an average recurrence interval of over 100 years for a detectable teleseismic range impact.

To predict seismic moment from crater size, future studies should avoid using the highly-

uncertain seismic efficiency. Instead, we recommend a momentum-based approach whereby the impactor momentum is first determined from crater size using π-group scaling and then seismic moment is calculated from impactor momentum using equation 3.7. For typical small impacts on Mars, the relationship between seismic moment and crater diameter found here (Fig. 3.17a) can be used as a first approximation:

$$M = 3.5 \times 10^5 \left(\frac{D}{1 \text{ m}} \right)^{3.3} \text{ Nm}. \tag{3.10}$$

For impacts into targets that differ substantially from the homogeneous representative target model employed here, some amplitude correction may be necessary to account for the transmission/reflection of seismic energy between the impacted target material and the bedrock below (Daubar et al., 2018).

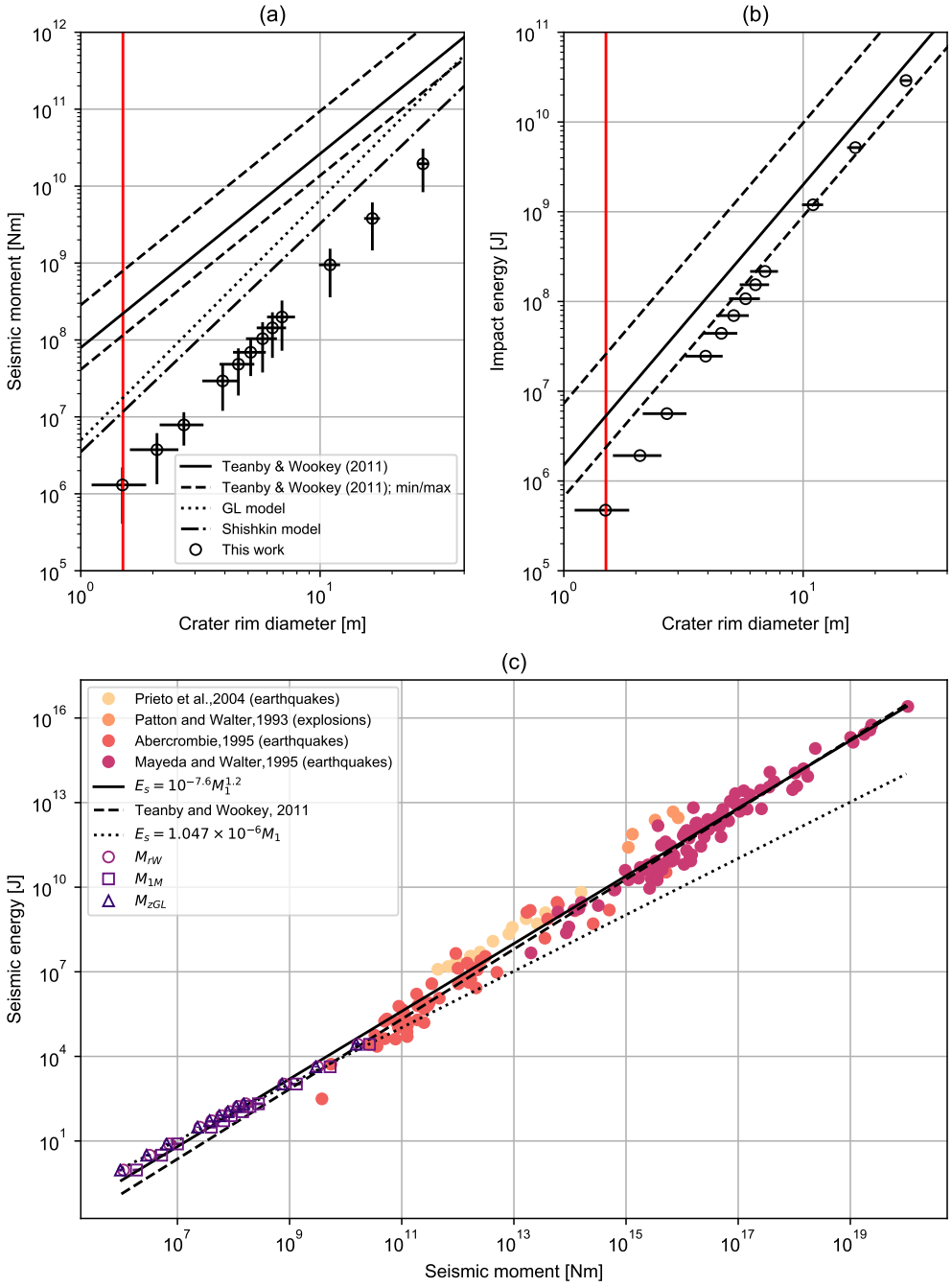

Figure 3.17: Scalar seismic moment (a) and impact energy (b) as a function of crater rim diameter. Simulation results of seismic moment and assumed impact energy are compared to the scaling relationships developed by Teanby and Wookey (2011), Gudkova et al. (2011) and Gudkova et al. (2015) (GL model) and Shishkin (2007) (Shishkin model). Note that the latter two models include correction factors to account for transmission of seismic energy from regolith into bedrock (Daubar et al., 2018), and incorporate both strength and gravity dominated scaling relationships of Holsapple (1993) to determine crater size. Horizontal error bars indicate the range of predicted crater diameter according to pi-group scaling; vertical error bars represent the range in seismic moment estimates from this work. Red vertical lines in (a) and (b) mark the size of the newly discovered small crater near InSight, for context (Daubar et al., 2020). (c) Seismic moment versus seismic energy, alongside data from previous studies of earthquakes and nuclear explosions (Prieto et al., 2004; Patton and Walter, 1993).

3.5 Conclusions

To characterise the seismic signal generated by typical small impacts on Mars, a set of small impacts onto martian regolith was simulated using the iSALE shock physics code. For each simulation, the impact was characterised as a seismic source using scalar seismic moment, seismic efficiency, ejecta momentum amplification factor, sphericalness of loading, and the radius of plastic-elastic wave transition.

Three approaches for calculating the scalar seismic moment of an impact from numerical simulation data (Müller, 1973; Walker, 2003; Lognonné et al., 2009) produced values that agree to within a factor of two and show that scalar seismic moment scales almost linearly with impact momentum. Future studies should use either a horizontal or vertical seismic moment approach: they produce consistent results and obviate the need for Lagrangian probes. Additionally, M_{zGL} required a shorter simulation to converge, hence this approach may be preferred if computational resources are limited.

For small impacts, the ratio of transferred momentum to impactor momentum increases from 1.3 for a 1-m crater to 1.6 for a 30-m crater, indicating a small but significant momentum amplification from ejecta. The leading impact-generated stress wave transitioned from a plastic to elastic behaviour at ∼10 crater radii. Moreover, the ratio of the horizontal to vertical seismic moment components is ∼1, implying, for vertical impacts at least, that small impacts on Mars are well represented by an isotropic seismic moment tensor. However, further work is required to determine whether this extends to oblique impacts.

The seismic efficiency (the ratio of radiated seismic energy to impact energy) of our simulated impacts was $\sim 1 \times 10^{-6}$, decreasing with impact velocity. This is akin to seismic efficiencies determined from artificial lunar impacts, but substantially smaller than estimates from terrestrial missile impacts and laboratory impact experiments. Seismic efficiency was very sensitive to the crushing curve of the target material. In particular, a factor of 50 increase in crushing strength increased seismic efficiency by about two orders of magnitude, while seismic moment only tripled. Due, in part, to this sensitivity, seismic moment is a more robust way to

characterise the seismic source than seismic energy.

The simulation-based estimates of the seismic moment of small impacts on Mars are lower than pre-landing estimates, while our seismic efficiency results are one-to-two orders of magnitude below the value assumed in some pre-landing estimates of the seismic detectability of small impacts by InSight (Teanby and Wookey, 2011; Daubar et al., 2018).

A suite of shorter timescale iSALE2D simulations was performed to investigate the source time function of small impacts and its dependence on individual impact parameters. The duration of the source was the most sensitive to the impactor size, with larger impactors exhibiting longer source duration. The convergence of momentum transferred to target at such small scales are consistent with convergence of M_{zGL} for similar impact scenarios. The force magnitude increased with impact momentum and decreased with higher target porosity. The force pulse was found to be well approximated by a Jeffrey's pulse approximation. The α constant was found to scale best with contact and compression timescale of the impact process as a power law, providing means for an approximated source time function to be derived for other impact scenarios.

Chapter 4

Current impact rate and detectability on Mars

Parts of this chapter are based on a study published in Journal of Geophysical Research: Planets, Wójcicka et al. (2020), a study published in Nature Geoscience, Garcia et al. (2022) and a manuscript currently in review Zenhäusern et al. (2022).

4.1 Introduction

The current impact rate on Mars is uncertain, with observational estimates (e.g.: Daubar et al., 2013) varying significantly from theoretical predictions (e.g.: Hartmann, 2005). Impact rates are of interest to the scientific community because they are vital for determining ages of planetary surfaces. They are also a key aspect of hazard assessment for future space missions. One of the key goals of InSight was to contribute to constraining of the impact rate by seismically detecting impacts, which was achieved in the final year of the mission.

The previous chapter explored detectability of small impacts on Mars by analysing iSALE2D simulation results and characterising the seismic source using several properties, including seismic moment and seismic efficiency. The simulation results show that less energy is transferred

to the target than previously expected, implying lower detectability of small impacts.

In this chapter a different approach is employed to compile the available impact data from various planetary bodies and develop a semi-empirical detectability model. The seismic moment scaling relationship developed in the previous chapter is also used here to connect seismic event magnitudes with corresponding crater diameters. The results are then used to compute the implied impact rate on Mars resulting from a subset of marsquakes detected by InSight.

4.1.1 First impacts detected seismically by InSight

In late 2021, the InSight team successfully identified the first impact generated seismic signals on Mars (Garcia et al., 2022). The key characteristic that led to locating corresponding craters in orbital images was a 'chirp' signal following the main seismic arrival. The chirp's frequency content changes with time, as different frequencies travel at different velocities. This part of the signal was attributed to the atmospheric disturbance caused by the impactor striking the ground. The waves travelled through the atmosphere to the lander, due to a narrow waveguide structure present in the atmosphere at low altitudes (<1 km; Garcia et al., 2022), allowing the waves to travel over long distances. The large difference between the seismic and acoustic wave speeds allowed very accurate source-receiver distance determination. In addition, the strong polarisation of each recorded chirp (alignment of motion with the incoming direction of the acoustic wave), lead to confident constraint of the back-azimuth of the event, as demonstrated in Garcia et al. (2022). The locations estimated using both seismic and atmospheric signals were searched using satellite imaging and three craters/crater clusters were found, corresponding to events: S0793a, S0981c and S0986c (Fig. 4.1) (named after the sol during which each event occurred, using MQS convention; Clinton et al., 2021). Statistical models of atmospheric entry (Collins et al., 2022) were used to constrain the impact properties, such as momentum and energy (Table 4.1). Further targeted searches also identified two more crater clusters, associated with events S0533a and S1034a. All five impacts are located 80-300 km away from the lander, and all are classified as Very High Frequency (VF) events (Böse et al., 2021).

Table 4.1: Properties of three of the nearby impacts detected seismically by InSight (Garcia et al., 2022).

event	crater diameter [m]	distance from lander[b] [km]	impact momentum [Ns]	interquartile range [Ns]	impact energy [J]	interquartile range [J]
S0793a	3.9	91.1	5.5×10^4	4.31-7.6 $\times10^4$	1.6×10^8	1.2-2 $\times10^8$
S0981c	7.2	243.6	2.52×10^5	2.10-3.41$\times10^5$	1.00×10^9	0.70-1.20 $\times10^9$
S0986c	6.1[a]	85.1	2.42×10^5	2.08-3.00 $\times10^5$	7.20×10^8	5.6-8.9 $\times10^8$

[a] Effective diameter for crater clusters.
[b] Distances from orbital imaging.

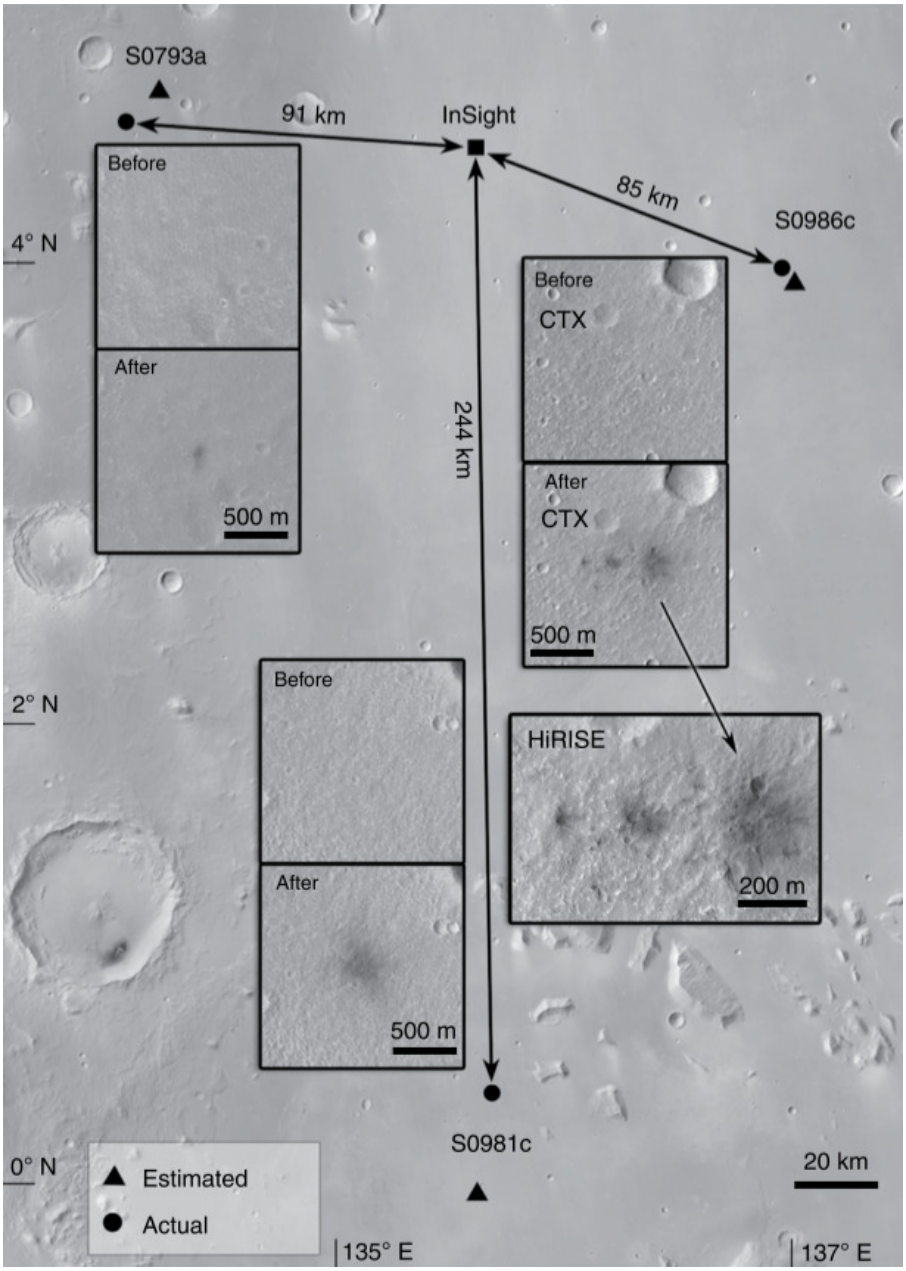

Figure 4.1: Three of the newly detected impact craters, corresponding to events: S0793a, S0981c and S0986c (figure from Garcia et al., 2022).

Soon after, the two largest fresh impact craters imaged to date on the surface of Mars were also detected by InSight (Posiolova et al., 2022). The craters, of diameters 130±12 m and 150±10 m, were first discovered in MRO Context Camera (CTX) and Mars Color Imager (MARCI) images, and were later attributed to events S1000a and S1094b, respectively, due to remarkable agreement in timing and source location. These events occurred significantly further away from the lander, at ∼3500 km and ∼7000 km, respectively, and were classified as Broad Band (BB) events (Böse et al., 2021) due to the characteristics of their frequency content. The craters corresponding to events S1094b and S1000a are shown in Fig. 4.2.

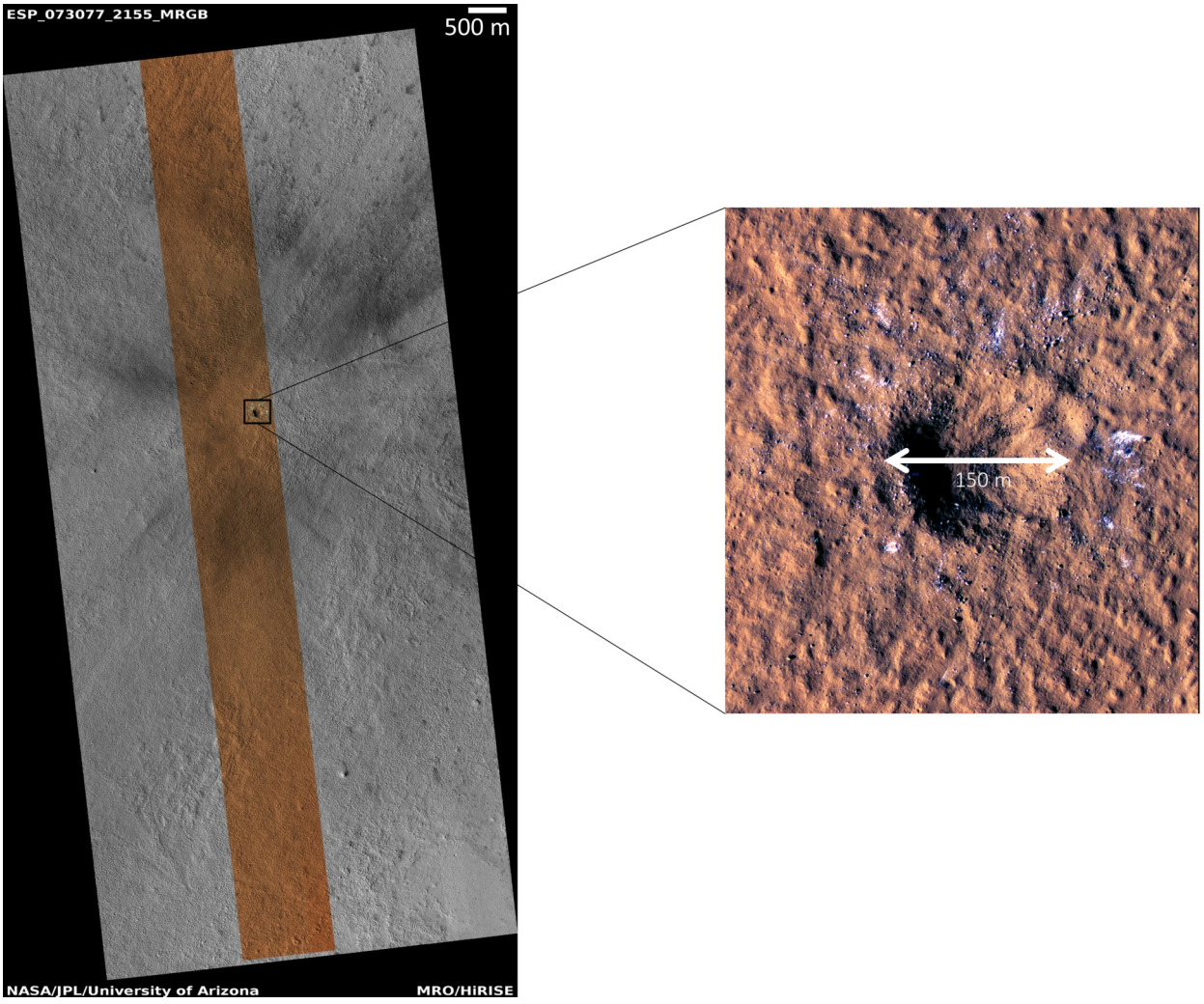

Figure 4.2: HiRISE image of the 150-m crater detected by InSight (Posiolova et al., 2022) corresponding to event S1094b. (Image credit: NASA/JPL-Caltech/UArizona; HiRISE image: ESP_073077_2155)

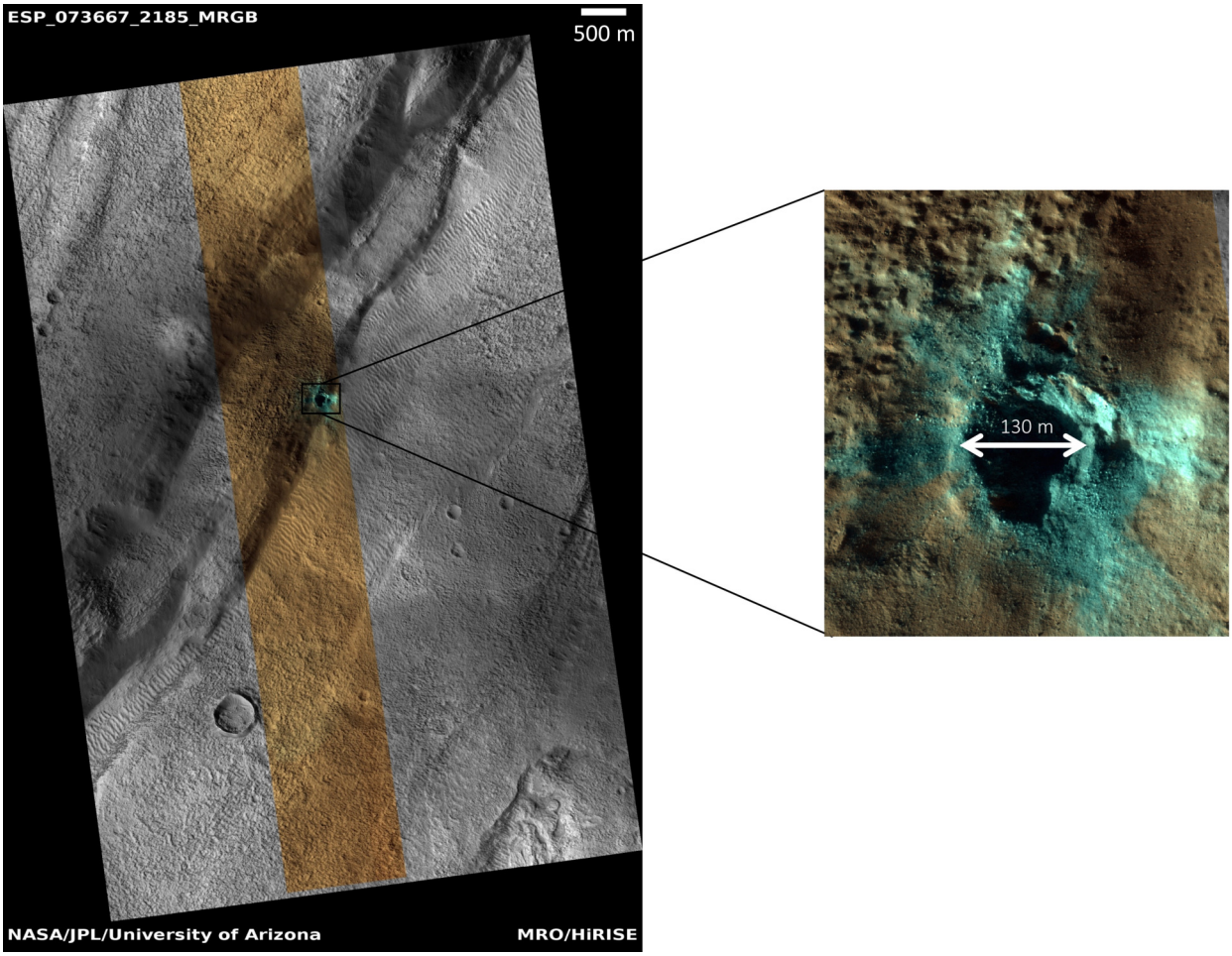

Figure 4.3: HiRISE image of the 130-m crater detected by InSight (Posiolova et al., 2022) corresponding to event S1000a. (Image credit: NASA/JPL-Caltech/UArizona; HiRISE image: ESP_073522_2185)

4.1.2 Are all VF events impacts?

During its lifetime, InSight has detected 71 VF events, 5 of which have been so far successfully attributed to impacts (Garcia et al., 2022). This family of events is characterised primarily by high frequency content (> 2.4 Hz) on all components, with the horizontal components displaying higher frequencies and higher energies than the vertical (Böse et al., 2021). Most events also contain a significantly amplified peak at 2.4 Hz (resonance), which is thought to be caused by the unique subsurface structure at the landing site (Dahmen et al., 2021).Resonance is defined as an amplification of amplitude at natural resonant frequencies of the medium. Here, the 2.4 Hz resonance effect is caused by layering of rock with high impedance contrast under the landing site. VF events are also exclusively regional events, with the bulk of their distribution determined to originate from distances up to 37° (∼2200 km, hollow diamonds in Fig. 4.4). The magnitudes of VF events increase with distance, implying a distance-dependent detectability combined with a uniform spatial distribution over the planet's surface, similar to what is expected of impacts (Driel et al., 2021). Unlike other families of event, VF events do not appear to be clustered in space, which would be expected of tectonic events originating at a particularly seismically active area.

The 'chirp' arrival, which led to the identification of the first four impact events is only present in signals originating closest to the lander, up to 6°. Out of 6 events followed by a 'chirp' signal (circled in Fig. 4.4), 5 have been (so far) identified as impacts. The chirp signal has been determined to be the signature of either the atmospheric disturbance during crater formation or, in the case of event S0986c, the shock wave generated by impactor's atmospheric entry (Garcia et al., 2022). The chirp's propagation is sensitive to the atmospheric waveguide structure. The chirp is also unlikely to be detectable for more distant events, since its amplitude will be reduced to below the noise level and its arrival time would be long after the seismic signal. This could suggest that there are other impact-generated events in InSight's seismic catalog, which haven't been categorised as such because they lack the atmospheric arrival, or even that the entire VF family of events could be attributable to meteorite impacts. In the latter case, a new constraint can be put on the impact rate on Mars - one of InSight's primary mission

objectives.

This chapter explores the hypothesis that all VF events are impact related and its implications for the impact rate on Mars using the semi-empirical scaling relationships derived in this chapter. Out of the 71 VF events recorded by InSight during its operations, 59 were deemed to be quality B or C events (Clinton and Euchner, 2021), according to the convention described in Sec. 2.5.1. These signals were clear enough to have source distances estimated for them and only those events are used in further analysis. The most distant events (S0923d and S1337a) are excluded because their seismic phase arrivals are much less clear than other events. The largest VF event is also excluded from further analysis, because it is deemed to be an outlier, as there is a significant gap in magnitude between this event and the rest of the distribution. The analysis in this chapter is limited to version 12 of the Marsquake Catalogue, which covers events up to Sol 1277. In the months following this very few seismic events were recorded due to low lander power and the noisy season on Mars. Hence, further analysis includes 56 events.

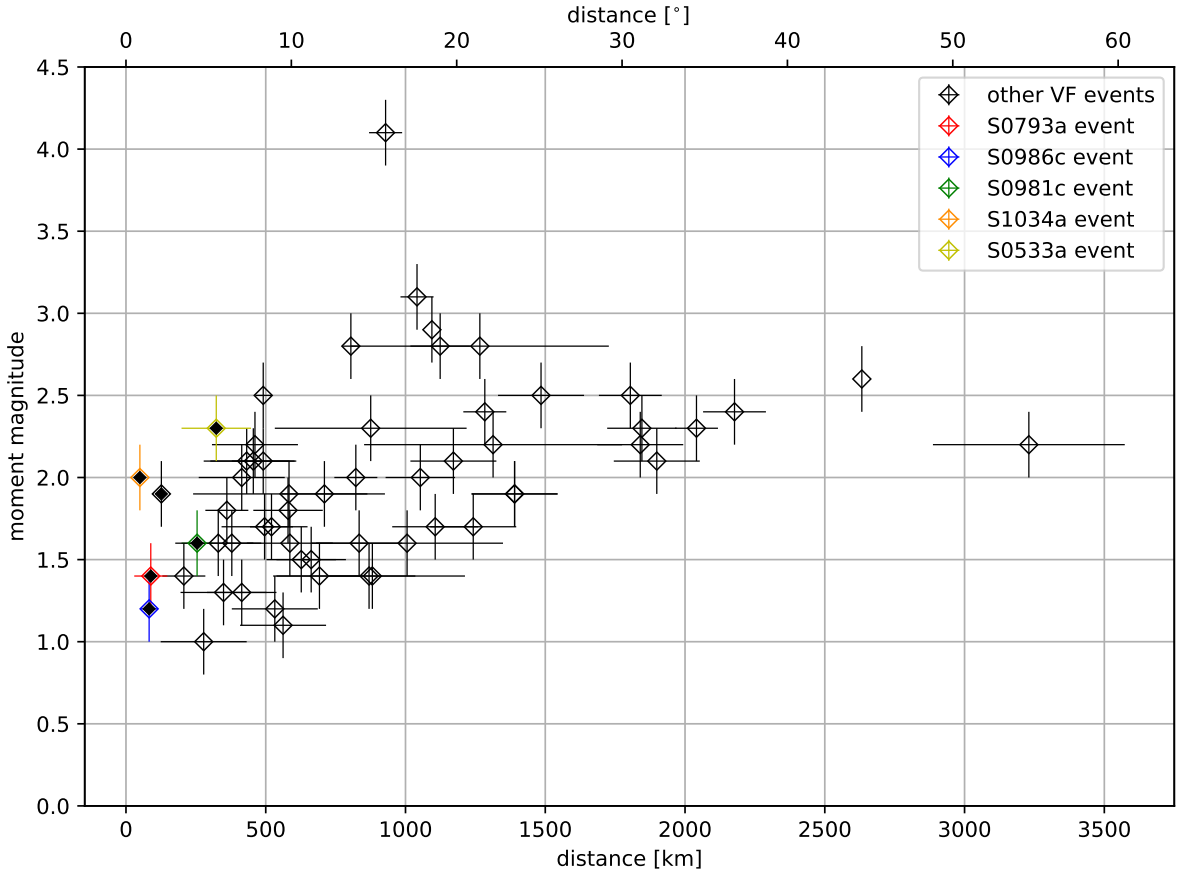

Figure 4.4: All VF events detected by InSight during the mission, for which locations could be determined (59 events). Moment magnitude is plotted as a function of distance. The coloured points show the events so far attributed to impacts (Garcia et al., 2022). Black filler in markers indicate events where the main seismic arrival is followed by a 'chirp' signal, identified as an atmospheric arrival.

4.1.3 Impact rates

Crater counts on planetary surfaces can be used to determine relative ages between surfaces. In general, the older the surface, the more craters will be present. The first crater counts were performed on the Moon using large craters ($D > 2\,\mathrm{km}$) visible from Earth (e.g., Young, 1940). These early studies showed that the number of craters of a given diameter produces approximately straight lines on a log-log plot. The assumption of power-law behaviour was adopted in later studies and quickly became the conventional way of representing cratering data (e.g.: Hartmann, 1964; Hartmann, 1965). These straight lines in $\log N$ vs $\log D$ are equivalent to a power law of the form:

$$N = kD^{-b}, \tag{4.1}$$

where D is the crater diameter, and k and b are constants (Neukum et al., 2001). b is the slope of the straight line on a log-log plot. With the advances in space exploration more crater counts became available, making it apparent that the complete size-frequency distribution comprises several sections defined by crater diameter ranges, where different constants k and b apply (Koenig et al., 1977; Durda et al., 1998). N in equation 4.1 can be defined as incremental (where counted crater sizes are sorted into pre-defined bins, usually of width $\sqrt{2}D$) or cumulative (where the data are cumulatively summed and the number of craters greater than a bin boundary is displayed). The rest of this chapter focuses on the cumulative measure of impact rate.

Typically, impact rates are described in terms of isochrons, defined as as a binned number of new craters over a specified time interval per unit area (Hartmann, 2005). For example, a 1-year isochron would contain the number of new craters (either incremental or cumulative) formed over 1 year per unit area. Isochrons are often used for deducing the ages of a surface of interest by comparing it to observed crater counts. Whilst crater counts only provide a measure of relative ages, rock samples collected on the Moon were independently dated to provide a measure of the absolute age of the surface they were collected from and a calibration

of the crater count curves (Stöffler and Ryder, 2001).

Hartmann (1966) used the size frequency distribution of lunar craters to derive one of the first expected impact rates on Mars over geologic timescales. These estimates included an adjustment due to difference in proximity to the asteroid belt of Mars and the Moon. The Mars impact rate model was subsequently updated in Hartmann (1999) and most recently in Hartmann (2005), where a correction factor due to atmospheric deceleration of small impactors (Popova et al., 2003) was included. The latest iteration of isochrons from Hartmann (2005) for different martian surface ages is shown in Fig. 4.5.

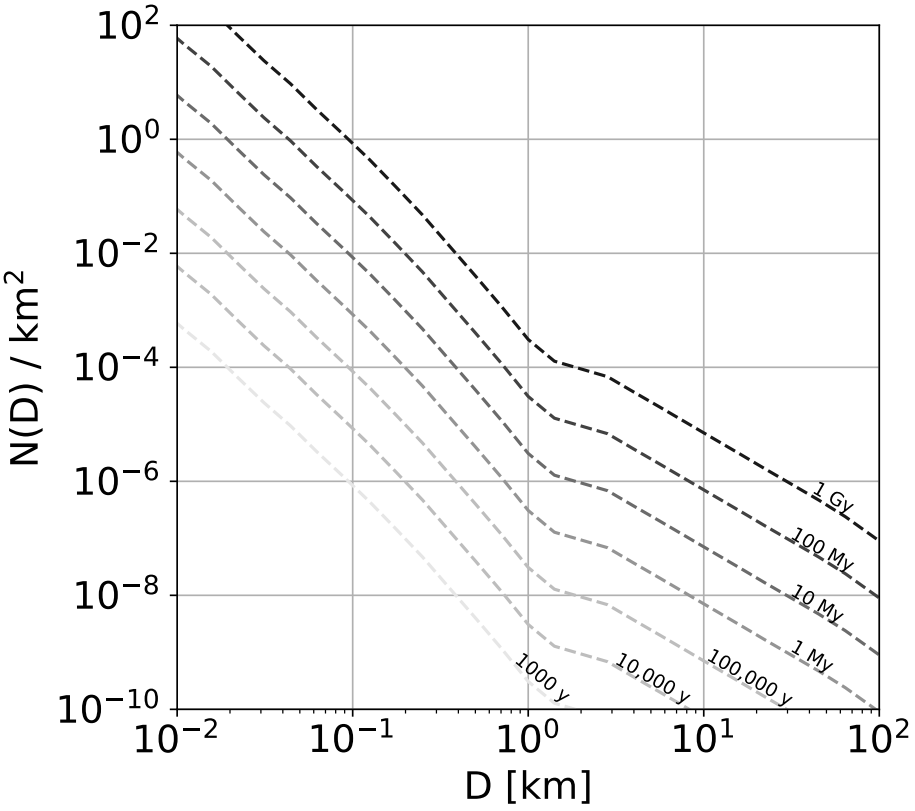

Figure 4.5: Hartmann isochrons for different ages of martian surface (Hartmann, 2005).

Because isochrons were derived based on counts of large craters on very old surfaces, scaling them down to shorter timescales (for example 1 year) requires a considerable extrapolation. Crater counts have to be extrapolated to small sizes where manual counting is intractable and further complicated by abundant secondary craters. The cratering rate is often assumed to be constant over the last 1 Gyr or longer, which does not allow for any fluctuations in impact rate

over shorter timescales.

A widely used method of measuring current impact rates on planetary bodies is to identify and count newly formed craters using orbital imagery. Usually, new craters are first identified in lower resolution images by the dark halos and streaks produced when dust is removed or disturbed around the crater. These low-albedo features are much larger than the craters themselves and hence easier to recognise in lower resolution images, for example CTX (MRO Context Camera) with resolution of 6 m/pixel (Malin et al., 2007) (for example the before and after panels in Fig. 4.1). After impact identification, follow-up images are taken with a high resolution camera such as HiRISE (High Resolution Imaging Science Experiment) of resolution of 0.25m/pixel (McEwen et al., 2007) (for example Fig. 4.2). These images provide more detailed information on crater size and morphology and the geology of the surrounding area. To inform crater production rates, the new crater counts are usually re-scaled by an Area Time Factor (ATF). An ATF usually comprises an area correction given by the total area searched and a time correction, given by the length of time the area was monitored, resulting in impact rates per km^2 per year.

The most recent studies of imaging campaigns such as Malin et al. (2006), Daubar et al. (2013), and Daubar et al. (2015), produced estimates of present impact rates on Mars. Malin et al. (2006) used MOC (Mars Orbiter Camera) images to identify 20 newly formed craters of diameter 2 - 148 m. Daubar et al. (2013) used CTX (MRO Context Camera) images to identify recent impact sites on the martian surface. HiRISE (High Resolution Imaging Science Experiment) images were used to confirm and measure the sizes of 248 new impact craters, 44 of which were constrained in time with before and after images. The crater diameters were 1.7 - 34 m. The incremental and cumulative impact rates from this study are shown in Fig. 4.6 as black circles. Daubar et al. (2013) also showed that ∼56% of impacts on Mars are crater clusters, where the impactor fragmented during its passage through the atmosphere. In these cases the effective diameter is used as the representative diameter of the impact, which is calculated as $D_{eff} = (\sum_{i=1}^{n} D_i^3)^{1/3}$, where n is the number of craters in the cluster and D_i is the crater diameter of each crater in the cluster. The effective diameter can be considered as a proxy for the size of the crater that would be formed if the impactor remained intact until the impact.

Daubar et al. (2013) observed a lower rate and a shallower slope of the cratering count than that of Hartmann (2005) isochron (Fig. 4.6). This suggests that for small craters the impact rate is lower than the average impact rate over geologic time scales, or the Hartmann (2005) isochron overestimates the yearly impact rate. The most recent cratering counts were presented in Daubar et al. (2022), who found the slope of the cumulative impact data to be b=2.2, for craters larger than 8 m in diameter. The searched area for these crater counts is unknown, so the impact rate per unit area cannot be compared with previous studies.

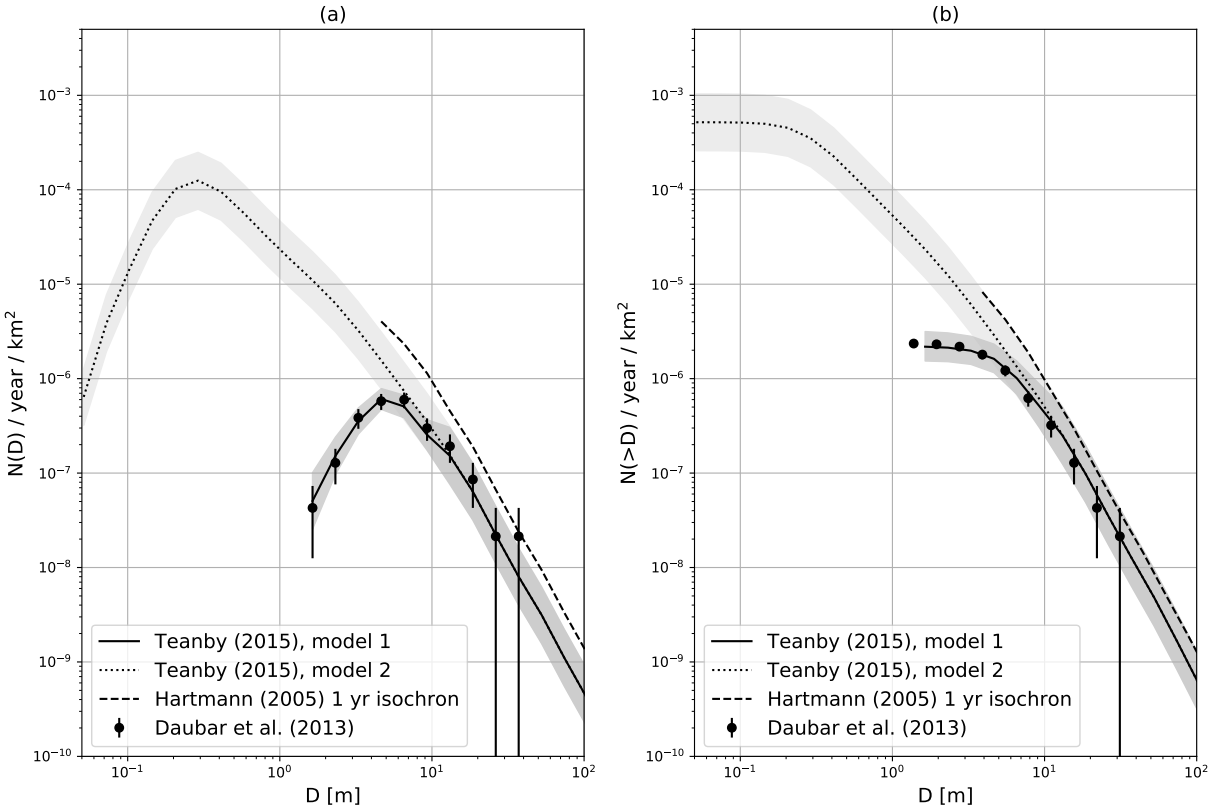

Figure 4.6: (a) Incremental and (b) cumulative impact rate estimates based on recent models (Teanby, 2015), observations (Daubar et al., 2013) and an extrapolation of the Hartmann (2005) isochron to small crater sizes.

In general, small craters are expected to occur more frequently than large ones. Incremental cratering rates on Mars based on orbital observations of Malin et al. (2006) and Daubar et al. (2013) reach a peak between 5 m and 10 m, below which the number of craters begins to fall. Atmospheric entry modelling (Popova et al., 2003; Williams et al., 2014) suggests that ablation only significantly affects the smallest of impactors. Therefore the roll-over observed in orbital

observations is most likely caused by the limit of resolution of the orbital imagery.

More recently, Teanby (2015) considered two models for the present-day rates (Fig. 4.6). Model 1 was based on the crater counts from Daubar et al. (2013) and assumed that these observations represent the entire scope of cratering on Mars. Model 2 on the other hand, extended these observation to be take into account the atmospheric ablation modelling for the smallest crater diameters presented by Popova et al. (2003) and Williams et al. (2014) (Fig. 4.6).

4.2 Detectability of impacts on Mars

Using seismic observations to derive impact rate on Mars requires two key elements: (a) a means of converting the seismic signals to a crater size, and (b) a measure of a Area Time Factor (ATF), which requires an estimate of detectability as a function of crater size, distance and time. This section uses a number of semi-empirical scaling relationships calibrated by impacts detected by InSight on Mars, to update the detectability estimates for impacts on Mars.

4.2.1 Empirical amplitude scaling for seismic amplitudes of impacts

Because impacts were only recognised in InSight data near the end of the mission, impact data from other bodies have been used to constrain detectability of impacts in preparation for such discovery on Mars. This section describes those approaches and compares the existing scaling relationships with newly acquired InSight data.

4.2.1.1 Energy-based approach (Teanby, 2015)

To better constrain the detectability of smaller impacts proximal to InSight, Teanby (2015) adopted an empirical approach to directly relate impact energy to ground velocity amplitude, based on data from impact and explosions experiments. Teanby (2015) proposed that peak P-wave amplitude scaled with square root of the impact energy for both impacts and explosions shows a decreasing trend with distance in km, where the amplitude falls as $x^{-1.6}$. This approach also employed the crater size to impact energy relationship from Teanby and Wookey (2011), which is shown in Chapter 3 to represent an overly optimistic estimate of impact detections.

4.2.1.2 Momentum-based approach (Wójcicka et al., 2020)

The numerical simulations presented in Chapter 3 advocate a momentum-based approach for extrapolating from ground-truth impact scenarios to small impact scenarios on Mars. This study therefore modified the approach of Teanby (2015) to develop two empirical relationships between P-wave peak amplitude v, range x and crater size D, based on vertical impactor momentum, rather than impact energy; one for impacts into a dry cohesionless sand and one for impacts into a somewhat more robust, weakly cohesive soil (Fig. 4.9). These relationships use π-group scaling equations to relate impactor momentum (and other properties) to crater size combined with separate fits to ground motion versus range data.

The impact data used here comprises three sets of impact experiments: the artificial impacts of the Saturn IV boosters on the Moon (Latham et al., 1970a), for which both the impact momentum and seismic amplitude is known; the Carancas impact on Earth (Brown et al., 2008; Kenkmann et al., 2009), where the impactor's mass and velocity were constrained using numerical modelling of the crater formation; and recently seismically recorded impacts on Mars (Garcia et al., 2022), for which impact properties were constrained using atmospheric entry modelling and are presented in Table 4.1. Fig. 4.7 shows that the data produces a clear trend with distance from source, where the peak P-wave amplitude v_{max} scaled by impact momentum p_i (where p_i in Ns is scaled to 10^6 Ns), drops as $x^{-1.56}$ (where x is scaled to 1 km). The resulting least squares scaling relationship is:

$$v_{max}\left(\frac{10^6\text{Ns}}{p_i}\right) = 1.1\times10^{-5}\left(\frac{x}{1\text{km}}\right)^{-1.56}. \tag{4.2}$$

In order to express the above equation in terms of observed crater diameter, π-group scaling equations are used to relate impactor momentum (and other properties) to crater size (Holsapple and Schmidt, 1982; Daubar et al., 2020). For cohesionless sand the momentum is given by:

$$p_\perp = 79.4D^{3.6}\left(\frac{v_i}{1000\text{ms}^{-1}}\right)^{-0.23}\left(\frac{g}{3.71\text{ms}^{-2}}\right)^{0.61}\left(\frac{\delta}{2000\text{kgm}^{-3}}\right)^{-0.19}\left(\frac{\rho}{1500\text{kgm}^{-3}}\right)^{1.19}, \tag{4.3}$$

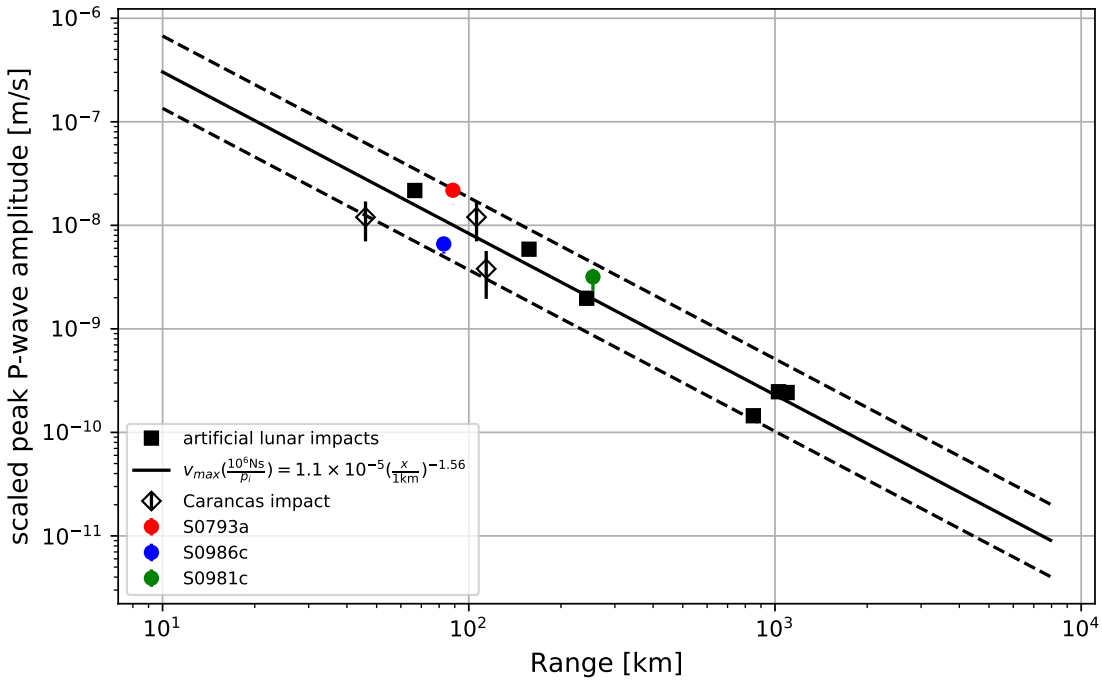

Figure 4.7: Peak P-wave amplitude scaled by impact momentum as a function of distance for artificial impacts on the Moon (black squares, Latham et al., 1970a), the Carancas impact on Earth (hollow diamonds, Brown et al., 2008; Kenkmann et al., 2009), and the seismically detected impacts on Mars (coloured markers Garcia et al., 2022). The black solid line shows the least squares fit to the nearby impact data (the Carancas impact, artificial lunar impacts and three martian impacts detected by InSight) at distances up to 1200 km. The dashed lines represent the uncertainty in the scaling relationship.

where x is the range in km, D is crater rim diameter in m, $v_\perp$ is vertical impact velocity in ms^{-1} and g is gravity in ms^{-2}.

For weakly cohesive soil the relationship is given by:

$$p_\perp = 821 D^3 \left(\frac{v_\perp}{1000\mathrm{m/s}}\right)^{-0.23} \left(\frac{Y}{100\mathrm{kPa}}\right)^{0.62} \left(\frac{\delta}{2000\mathrm{kgm}^{-3}}\right)^{-0.2} \left(\frac{\rho}{1500\mathrm{kgm}^{-3}}\right)^{0.59}, \quad (4.4)$$

where $v_\perp = 3535$ m/s is the vertical impact speed, chosen as the vertical component of velocity for a typical metre-range impactor (most relevant for this work) on Mars at the most common impact angle of 45°. Based on atmospheric deceleration of impactors in this size range from average atmospheric entry velocity of $\sim 10\,\mathrm{km/s}$, vertical velocities of impacts forming craters between 1-30 m in diameter are likely to range between 1-6 km/s. $Y = 50$ kPa is the target

strength, appropriate for weakly cohesive regolith (Daubar et al., 2020). $\delta = 2000$ kgm^{-3} is the impactor density and $\rho = 1500$ kgm^{-3} is the target density based on a porous, weakly cohesive regolith material. Whilst the exact parameters appropriate for each impact scenario are likely to vary from those chosen here, the crater diameter measurement is the largest source of uncertainty in the impact momentum estimated. Furthermore, this relationship only applies to small craters in the strength regime of impact cratering.

The difference between equations 4.4 and 4.3 is shown in Fig. 4.8. The variation in vertical impact velocity shown was chosen based on typical impacts on the surface of Mars forming craters between 1-30 m, which are the most relevant for InSight (see Sec. 3.2).

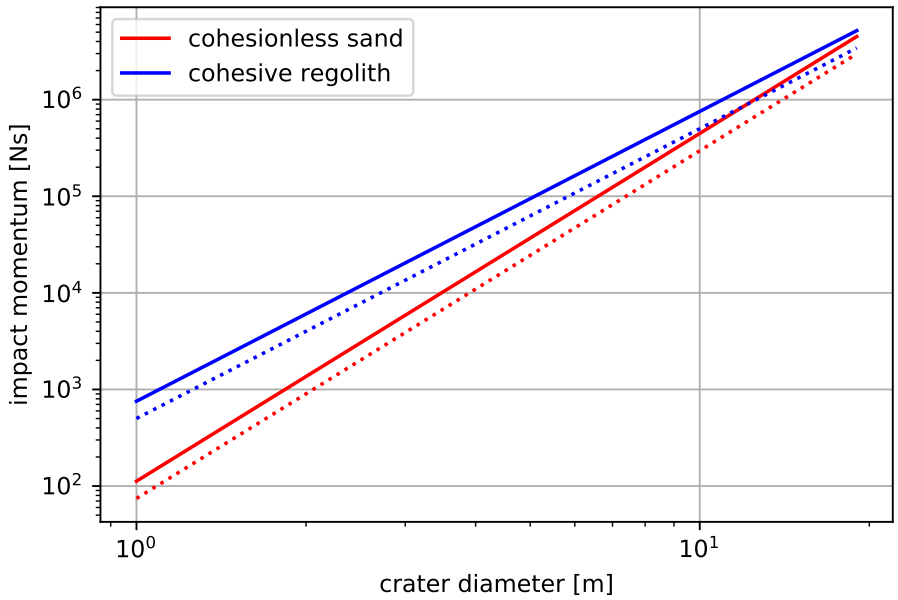

Figure 4.8: The relationship between impact momentum and crater diameter for impacts in weakly cohesive regolith (blue) and cohesionless sand (red). The solid lines represent an impact at vertical velocity of 1 km/s and the dotted lines at 6 km/s.

The two largest impacts detected by InSight (events S1000a and S1094b, Posiolova et al., 2022) were also the most distant impacts recorded seismically on any planetary surface, at distances of ∼3000 km and ∼7500 km respectively. These provide an excellent opportunity to test the amplitude-distance scaling relationships beyond previously available distances. For these two events, the first arrival P-wave amplitudes could not be measured, because for such distant

source the waves propagate largely within the mantle and may even reach the core, and can therefore be subjected to reflection and diffraction. As such for events 1000a and 1094b only amplitudes of PP (P-wave reflected from the underside of the martian surface) and Pdiff (P-wave diffracted around the outer core boundary) were measured. These amplitudes scaled by the impact momenta predicted from observed crater sizes are substantially lower than equation 4.2 predicts. This could indicate a transition to a steeper amplitude-distance power law at such large distances, although more data in this range is required to confirm or refute this hypothesis. Because of this, the two large distant events are not included in further analysis in this chapter.

4.2.2 Revised detectability of impacts on Mars

The seismic data from the four impacts recently detected on Mars, combined with impact data from Earth and the Moon, provide new estimates of P-wave amplitudes as a function of distance for several impact scenarios in the range more relevant for InSight (crater diameters between 1-100 m). The two momentum-based empirical scaling relationships (Fig. 4.9a and Fig. 4.9b) show a much greater variation in peak amplitude with crater diameter than the energy-based approach (Fig. 4.9a). For a ∼30 m crater diameter, which represents the scenario closest to the Saturn IV booster impacts on the lunar regolith, the three approaches are relatively consistent, differing by only a factor of 5. However, when crater size and ground velocity are scaled by impactor momentum, the peak amplitudes predicted for craters less than 20 meters in diameter are 10 to 100 times lower than the energy-scaling predictions, depending on the material properties of the target.

The measured noise at the InSight landing site varies significantly over the course of a day. Following Teanby (2015) and Daubar et al. (2020) seismic noise in the 1-16 Hz frequency range can be considered as the most appropriate for small impact craters. The measured seismic noise at the 4 Hz geometric centre of the range varies from p_a=1.5 $\times 10^{-9}$ ms^{-2} Hz$^{-1/2}$ during quiet periods to 1×10^{-7} ms^{-2} Hz$^{-1/2}$ during noisy periods (Lognonné et al., 2019; Lognonné et al., 2020). This corresponds to peak noise levels in seismic ground velocity of n_v=2.9×10^{-10} ms^{-1}

to 1.9×10^{-8} ms^{-1}, using $n_v = (5/8\pi)p_a\sqrt{1/f_1 - 1/f_2}$ from Teanby (2015) for a frequency range of $f_1 = 1$ Hz to $f_2 = 16$ Hz (horizontal lines in Fig. 4.9).

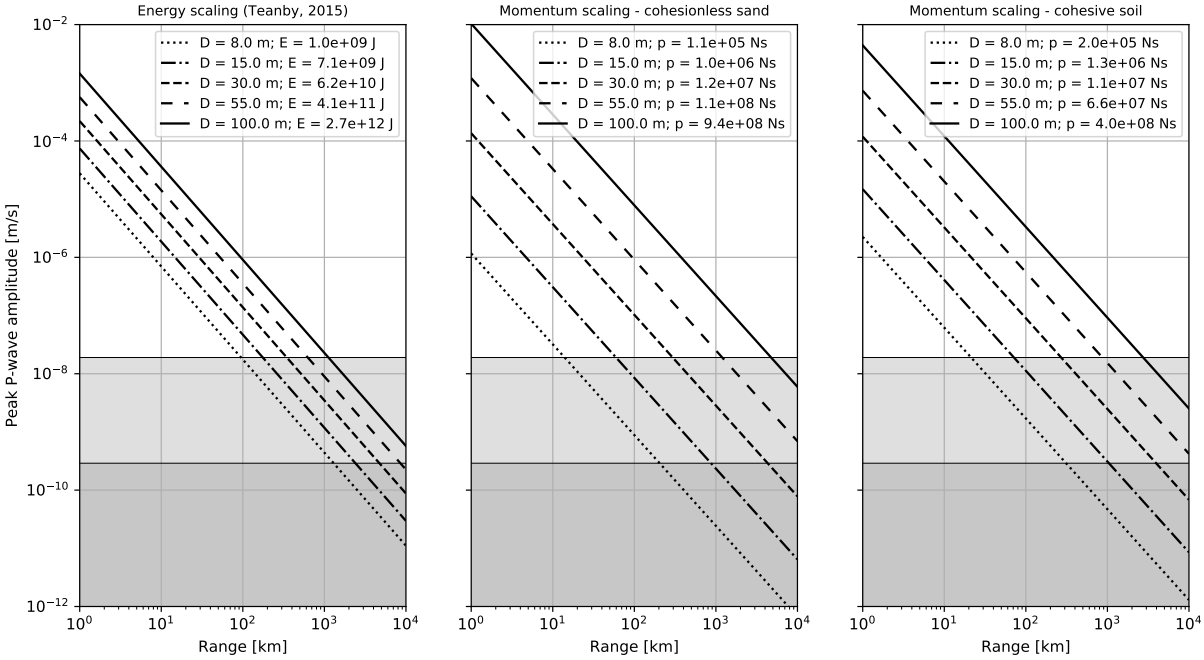

Figure 4.9: Predictions of P-wave peak amplitude versus range for different impact crater diameters using three different scaling approaches. (a) P-wave amplitude is scaled by the square-root of the impact energy as described by Teanby (2015); crater diameter is related to impact energy by the scaling relationship of Teanby and Wookey (2011). (b) P-wave amplitude as measured in lunar SIVB impacts (Latham et al., 1970b), the Carancas impact on Earth (Kenkmann et al., 2009) and three impacts detected by InSight (Garcia et al., 2022) is scaled by the impactor momentum (equation 4.2), crater diameter is related to impactor momentum by π-group scaling (Holsapple, 1993) for cohesionless sand (equation 4.3). The results presented assume $v_\perp = 3535\,\mathrm{ms}^{-1}$, $\rho = 1500\,\mathrm{kgm}^{-3}$, $\delta = 2000\,\mathrm{kgm}^{-3}$. and cohesion is neglected. (c) P-wave amplitude estimates using the newly detected impacts on Mars, the Carancas impact on Earth and the artificial lunar impacts. The crater diameter is related to impactor momentum by π-group scaling (Holsapple, 1993) for a cohesive soil using the same parameters as (b) but with cohesion $Y = 50\,\mathrm{kPa}$ (equation 4.4. Horizontal lines and shading represent measured InSight noise levels at 1-16 Hz from Lognonné et al. (2019) and Lognonné et al. (2020) under low noise and high noise conditions. The impact energy E or momentum p corresponding to each crater size is given in the legend.

Fig. 4.10 shows the maximum detectable distance for craters of diameter $1 < D < 150\,\mathrm{m}$ (at low noise conditions), estimated by three detectability models in this chapter. The momentum-based scaling approach derived here suggests that craters of diameter <30 m are detectable at much shorter range from InSight than previously proposed. The two momentum-based scaling relationships also show variation depending on which material properties are assumed

when converting between momentum and crater size. In the most pessimistic case, where the impact occurs in a loose, porous and cohesionless target, a 1-m crater >3 km away would be undetectable, even under low noise conditions. On the other hand, this approach suggests that craters of diameter >30 m are much more detectable, particularly if the impact were to occur in a part of Mars with a stronger, denser surface with more efficient ground coupling of impactor momentum. The cohesive regolith scaling appears to be the best fit to the data currently available for Mars, as all impact craters accociated with a seismic event lie above the detectability curve. All impact craters constrained to have occurred during InSight's operations using orbital imaging but not detected seismically lie below the detectability curve. In addition no undetected craters lie significantly above the detectability curve, which would imply they should be detectable during both low and high noise. The cohesioneless sand scaling appears to predict a slightly more pessimistic scenario, excluding two of the recently detected impact craters as undetectable. The energy-based Teanby (2015) approach predicts that several of the undetected small craters should be detectable at low noise conditions, although this can be explained by the impacts occurring during high noise part of the sol.

The martian data used in the scaling relationships contains both single craters and crater clusters. In the case of crater clusters, the effective diameter was used for converting between impact momentum and crater size, which may be an oversimplification for the most complex scenarios. Event S0986c in particular was determined to be a very oblique and complex impact (Garcia et al., 2022). Fig. 4.7 shows that scaling the P-wave amplitude by estimated impact momentum put the event slightly below the single crater events discovered at similar distances. Since over 50% of impact on Mars are expected to form crater clusters (Daubar et al., 2013), it is likely that there are more of such complex impact scenarios in the VF dataset. Finding these craters and examining their seismic signatures can be further complicated by topographic features, which may obscure the craters themselves. Future studies should explore in detail how the difference between crater clusters and single craters, as well as impact angle affect the amplitude-distance scaling.

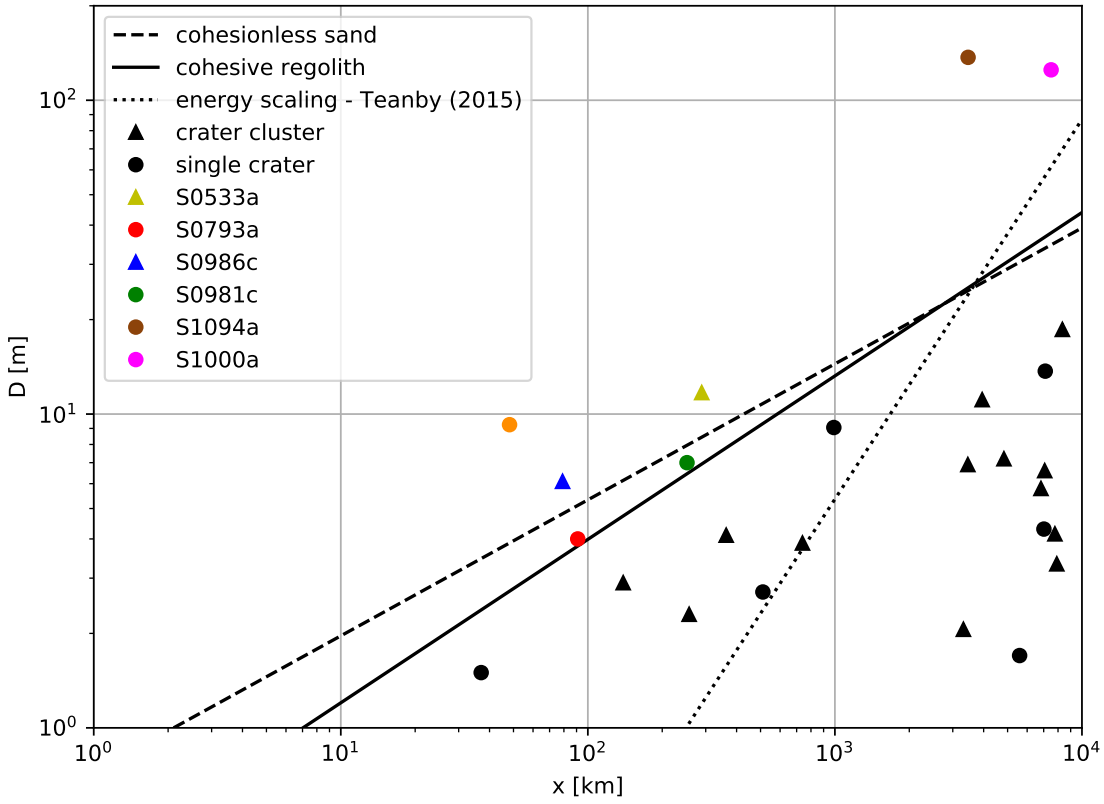

Figure 4.10: Detectability of impact craters of diameter D as a function of distance from InSight (x in km), at the average low noise level recorded at the landing site ($v_{noise} = 2.9 \times 10^{-10}$ m/s). Three models are shown for comparison: energy-based scaling (dotted line, Teanby, 2015), momentum-based scaling for impacts into cohesionless sand target (dashed line) and the momentum-based scaling for impacts into cohesive regolith target (solid line). Five nearby impact craters detected by InSight are shown with coloured markers. Other craters discovered during InSight's operations, but not detected seismically are also shown as black markers.

4.3 Impact rate on Mars

The following sections present two methods of achieving the means of converting seismic signals to crater size: one using peak P-wave amplitudes (Method 1, Sec. 4.3.1), and one using seismic moment magnitudes (Method 2, Sec. 4.3.2).

4.3.1 Method 1: Impact rate on Mars implied by peak P-wave amplitudes

A natural progression from the amplitude distance scaling derived in the previous section is to use the seismic amplitudes recorded by InSight to predict a crater size of a given event, for example to aid search for a crater corresponding to a suspected impact event. As shown in the previous section, the cohesive regolith was determined to be the most appropriate version of the momentum based scaling (equations 4.2 and 4.4).

Combining equation 4.2 with equation 4.4, and assuming a 45° impact angle for converting between scalar and vertical momentum, results in the maximum distance a crater of given size D would be detectable assuming noise level v_{max}:

$$x_{max} = 5.53 \times 10^{-6} D^{1.92} v_{max}^{-0.64}. \tag{4.5}$$

Analogously, for an event at a given distance x_{event}, producing an amplitude v_{event}, the predicted crater diameter $D_{\text{predicted}}$ is given by:

$$D_{\text{predicted}} = 542\, v_{\text{event}}^{1/3} x_{\text{event}}^{0.52}. \tag{4.6}$$

Equation 4.6 is applied to each VF event to obtain its predicted crater diameter.

In this approach, it is crucial to consider the frequency range in which the amplitude is determined. The artificial lunar impact data and the Carancas impact data also used in this

chapter was Butterworth bandpass filtered with corner frequencies of 1 and 16 Hz, as detailed in Teanby (2015). In the case of the InSight VF events identified as impacts, the peak P-wave amplitude was determined using a seismogram filtered with corner frequencies of 3-8 Hz, chosen to be as close to the frequency range of the other data used here as possible. The Marsquake Catalogue (Clinton and Euchner, 2021) however, does not contain signal in this frequency range and extensive reprocessing of seismic data would be required to obtain these amplitudes for all events. As mentioned in Sec. 4.1.2, VF events contain an amplified peak at 2.4 Hz ($A_{2.4\,\mathrm{Hz}}$), which is stored in the Marsquake database. Fig. 4.11 illustrates that when both amplitudes are scaled by impact momentum, the $A_{2.4\,\mathrm{Hz}}$ is consistently higher than $A_{3\text{-}8\,\mathrm{Hz}}$ by a mean factor of 4.9. Hence, using $A_{2.4\,\mathrm{Hz}}$ in equation 4.6 would result in crater diameters larger by a factor of 1.7. To counteract this effect, the amplitudes at 2.4 Hz recorded in the Marsquake Catalogue are reduced by a factor of 4.9.

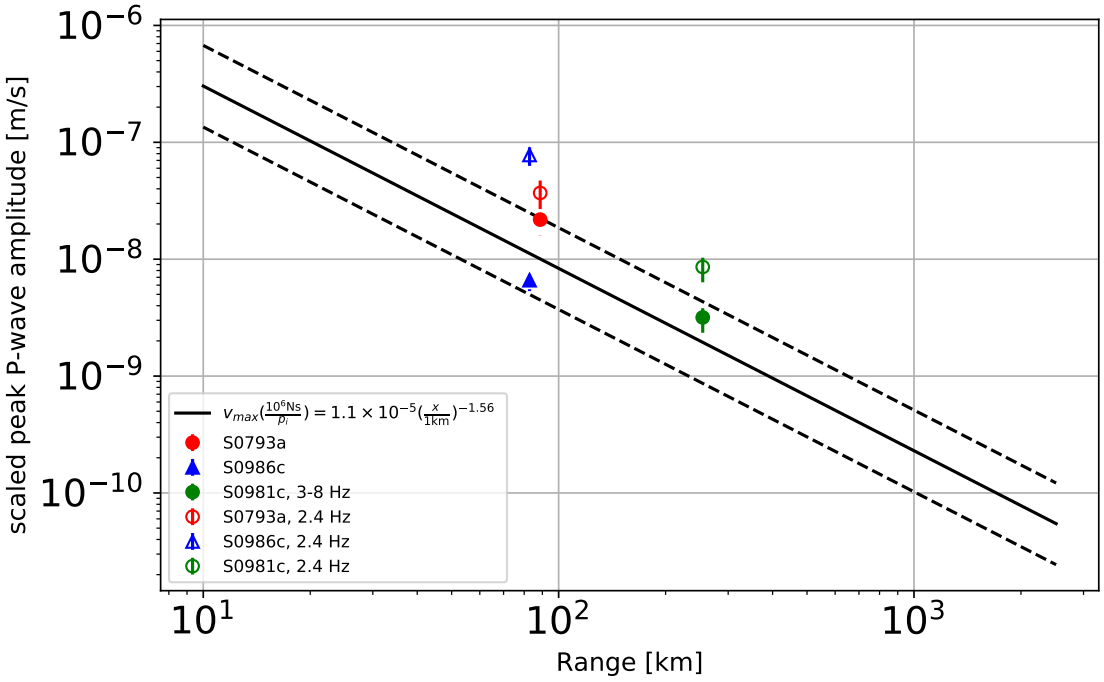

Figure 4.11: Amplitude measured in frequency range 3-8 Hz (filled markers) versus the 2.4 Hz resonance amplitude (hollow markers), for the four small crater recorded seismically (Garcia et al., 2022).

To estimate a crater size, equation 4.6 is applied to each of the considered VF events. The resulting distribution of crater sizes is 3-40 m (Fig. 4.12a). The largest contribution to the

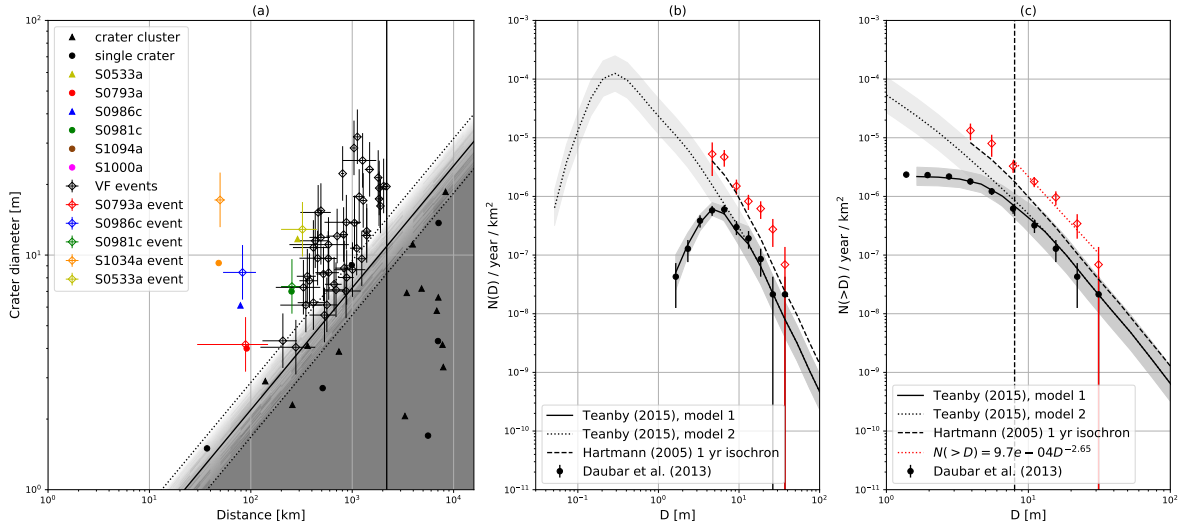

Figure 4.12: (a) The detectability of craters of a given diameter as a function of distance. The black circles and triangles are observed but not detected impact craters and crater clusters (respectively) that are constrained to have occurred during the InSight mission. The coloured filled in points are observed and detected craters and clusters, colour-coded by event name. The hollow diamonds in corresponding colours are the predicted crater sizes of detected impact events based on peak P-wave amplitude. The black hollow diamonds show the distribution of predicted crater sizes for all other VF events. The solid black line indicates the detectability curve for noise amplitude of 5×10^{-11} m/s. This curve defined the Area Time Factor used to calculate impact rates up to a distance of 37°. Beyond that distance, no VF events are expected to be detected. (b) Incremental impact rates resulting from the distribution of predicted crater sizes for all VF events using peak P-wave amplitude scaling shown in (a). The most recent imaging based rates from Daubar et al. (2013) are shown by black circles. The solid and dotted black lines show Teanby (2015) Model 1 and 2 respectively (with grey lines marking uncertainty). The dashed black line indicates the Hartmann (2005) 1-yr isochron (rescaled from 1 Gyr isochron). (c) Cumulative impact rates resulting from the distribution of predicted crater sizes for all VF events using peak P-wave amplitude scaling shown in (a). The dashed line indicates the 8 m mark for comparison between studies.

uncertainty in predicted crater diameter is due to the conversion from amplitude to impact momentum. The colour-coded markers indicate a very good match between the predicted and observed crater sizes for 3 out of 5 events identified as impacts. This method overestimates the crater sizes for the 2 remaining events (S0986c and S1034a). Both of these events were attributed to either a crater cluster produced by more than one fragmentation event (S0986c) or a single crater with an unusually large number of secondary craters (Garcia et al., 2022). The complexities of these two events may explain the disagreement between the observed and predicted craters sizes.

Fig. 4.12a also shows impact craters and crater clusters detected using orbital imaging (black markers), which have been constrained to have occurred during the InSight mission, but were not detected seismically. Whilst the majority of these craters lie below the detectability line, several also lie above it. This could suggest that those impacts occurred during the noisy period and therefore were not seismically detected. No impact craters without an associated seismic event were imaged during the mission that lie significantly above the detectability threshold, supporting the appropriateness of its placement.

Fig. 4.12b and c show the incremental and cumulative impact rates derived from the distribution in Fig. 4.12a. The incremental rate is computed by binning the data in bins of width $D\sqrt{2}$. The binned data is then scaled by the Area Time Factor (ATF). An ATF usually comprises an area correction given by the total area searched and a time correction, given by the length of time the area was monitored. The 'searched area' is computed by assuming that impact detectability is size and distance dependent. Smaller impacts will stop being detectable at shorter distances than large ones, as can be seen from distribution of VF events. To account for this, the maximum distance at which the central crater in a given bin would be detectable is calculated using equation 4.5 (solid black line on Fig. 4.12a), up to a distance of 37° (≈ 2200 km, black vertical line on Fig. 4.12a), since no VF events included in this study are seen beyond that distance. The detectability amplitude was chosen to fall just below the smallest predicted crater diameter of the VF events, as $v_{max} = 2 \times 10^{-11}\,\mathrm{ms}^{-1}$. The maximum detectable distance of 37° takes effect for craters from approximately 10 m in diameter. The area factor for the given crater size bin is given by the circular area of radius equal to the detectable distance around InSight, resulting in impact rates per km^2.

The second element of the ATF is the time correction. It is assumed that that due to noise variation during each sol, VF events are detectable approximately during 1/3 of the day. Because the VF dataset spans 3 years of recording time, the time factor is assumed to be 1, and the resulting rates are shown per year per km^2. The cumulative rate (Fig. 4.12c) is calculated as a cumulative sum of the incremental rate (Fig. 4.12b), and is also given per year per km^2.

The resulting incremental rate is approximately 4 times higher than the rate measured in

Daubar et al. (2013) and only slightly larger than the Hartmann (2005) 1-year isochron (Fig. 4.12b). The cumulative impact (Fig. 4.12c) rate predicted by the amplitudes recorded for VF events larger than previously measured using orbital imaging and the cumulative Hartmann (2005) isochron rate. The results follow a power law of the form of equation 4.1 and the least squares fit for crater sizes between 8 and 30 m gives $a = 9.7 \times 10^{-4}$ and $b = 2.64$. Whilst the yearly impact rates are higher than those predicted by previous studies, the gradient of the cumulative rate is in close agreement with that determined in Daubar et al. (2013). The values plotted in Fig. 4.12 are shown in Table 4.2.

4.3.2 Method 2: Impact rate on Mars implied by the seismic moment magnitudes

Ideally, seismic magnitudes (i.e., seismic moments) measured at InSight would be used to predict crater sizes for potential impact events, and to determine detectability of impacts. Magnitudes are frequency range independent, making them a more robust parameter to be used. However, magnitude scales derived for Mars using InSight data may need to be revised specifically for an impact source. This section adapts the above workflow for predicting crater sizes from seismic amplitudes to one that uses the moment magnitudes.

Seismic moment is related to seismic moment magnitude via the equation:

$$M_W = \frac{2}{3}(\log_{10} M_{MQS} - 9.1), \tag{4.7}$$

where M_{MQS} is the seismic moment assigned to seismic events detected by InSight (Böse et al., 2021). Results of numerical simulations (Wójcicka et al., 2020), provide a first-order scaling relationship for the seismic moment generated from small impacts on Mars, as a function of crater size:

$$M_{source} = 3.5 \times 10^5 \left(\frac{D}{1\,\mathrm{m}}\right)^{3.3}, \tag{4.8}$$

where D is the mean crater size determined for a range of impact scenarios simulated in Wójcicka et al. (2020), for craters formed in cohesionless sand and weakly cohesive regolith. The range

of crater sizes due to target material properties assumed provides the uncertainty on D. Combining equations 4.7 and 4.8 results in a relationship between the seismic moment magnitude and predicted crater diameter.

The impact data recorded by InSight shows that M_{MQS} is broadly proportional to $D^{3.3}$, consistent with simulation results. The seismic moment values obtained from source numerical simulations and corresponding to equation 4.8 are however significantly lower than M_{MQS} determined for events recorded at InSight. This is illustrated in Fig. 4.13 for the impact events detected by InSight, where both the crater size and seismic moment were independently measured (filled coloured markers). The scatter of the observed data can be attributed to differences in soil properties directly under the impact site. The Garcia et al. (2022) also used full waveform modelling to determine the predicted seismic moment of three of the impacts (s0793a, S0981c and S0986c). These estimates are between the results of impact source simulations and the M_{MQS} (shown as hollow markers in Fig. 4.13). This problem was discussed in more detail in Posiolova et al. (2022), where it was proposed that the seismic moment released in an event depends heavily on the material properties at the source depth, more specifically the combination of density and seismic wave velocity. For a marsquake of tectonic origin, the source depth is likely to be 30-50 km, consistent with magnitude scales developed for Mars (Böse et al., 2021). For an impact, the depth at which the seismic moment is released is significantly shallower, approximately equivalent to the crater diameter. For the craters in the size range of the detected impacts, this depth is of the order of metres or tens of metres. At such depths, the seismic velocities are of the order of hundreds of ms^{-1}, many times slower than at 30-50 km. This means that since the equivalent seismic source moment will vary from the one measured at InSight by a product of P-wave velocity cubed (c_P^3) and density at the approximate source depth, a correction factor of several order of magnitude may be required. A correction factor, c, is introduced to account for this difference in depth, resulting in the following expression for the receiver measured moment:

$$M_{MQS} = c \times 3.5 \times 10^5 \left(\frac{D}{1\,\mathrm{m}} \right)^{3.3}. \tag{4.9}$$

The true value of c is dependent on depth of seismic moment release, which is likely to depend

on the crater size and exact subsurface structure under the crater. However, because crater size is unknown for all but four VF events, and this chapter aims to constrain the crater size distribution based on the seismic moment distribution of VF events, the approach of a crater size-dependent correction is not feasible. Instead, this study estimates c by using the four seismically detected impacts near InSight: S0533a, S0793a, S0981c and S0986c. For these four events, both the measured seismic moment magnitude and the observed crater size are known independently, and hence they can be used as a benchmark for the most appropriate value of c. The coloured markers in Fig. 4.13 show the receiver-measured seismic moment as a function of crater diameter. A least-squares regression was used to find the optimal value of c to be 2831±900. This approach is further justified, because the four events' M_{MQS} values were in the range 10^{10} - 10^{13} Nm, which contains most of the considered VF events dataset. By using a constant c, the crater diameter is more likely to be underestimated for larger events, and overestimated for smaller events. This is further illustrated by the two very large craters (Posiolova et al., 2022), whose MQS seismic moment falls below the trend of seismic moment vs diameter for the smaller events (Fig. 4.13).

Applying equations 4.7 and 4.9 to the VF events dataset returns a distribution of crater diameters between 3 and 30 m. As shown in Fig. 4.14a, the predicted crater sizes for 3 our of 5 detected impacts are consistent with the observed crater diameters. As in the results of Method 1, the crater diameters for events S0986c and S1034a are underestimated, which can be attributed to the complexity of these cratering events.

The incremental impact rate implied by the resulting distribution of crater sizes was calculated using the same approach as in Method 1. The area was calculated using the detectability curve shown in Fig 4.14a, where the detectability amplitude was chosen to fall just below the smallest predicted crater diameter of the VF events, as $v_{max} = 4 \times 10^{-11}\,\mathrm{ms}^{-1}$. As shown in Fig 4.14, the resulting incremental rate is only slightly higher than measured in Daubar et al. (2013) and is in good agreement with the Hartmann (2005) 1-year isochron.

The cumulative rate (red diamonds in Fig. 4.14c) is calculated as a cumulative sum of the incremental rate (red diamonds in Fig. 4.14b). The cumulative impact rate predicted by the

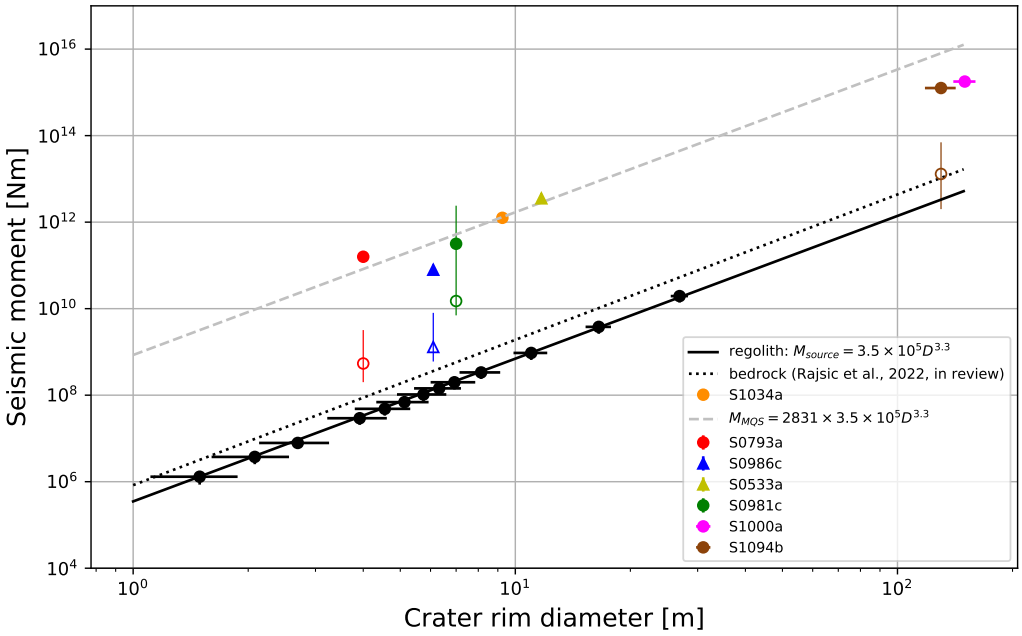

Figure 4.13: Seismic moment as a function of crater diameter. The black circles indicate simulation results from Wójcicka et al. (2020) with the black line as the least squares fit. The filled coloured markers show the seismic moment determined in the InSight MQS Catalogue vs the observed crater size for the four nearby impacts (Garcia et al., 2022) and two distant very large impacts (Posiolova et al., 2022). The silver line shows the least squares fit to these events, producing $c = 2831 \pm 900$. Hollow markers represent the seismic moment values determined in Garcia et al. (2022) using full waveform modelling for the three out of the recently detected events (S0793a, S0981c, S0986c). The hollow dark brown marker indicates the source seismic moment of event S1094b, determined by estimating the depth of seismic moment release (Posiolova et al., 2022).

VF events recorded by InSight is slightly larger than previously measured using orbital imaging and the cumulative Hartmann (2005) isochron rate. The results follow a power law of the form of equation 4.1 and the least squares fit for crater sizes between 8 and 30 m gives $a = 4.2 \times 10^{-4}$ and $b = 2.29$. The values plotted in Fig. 4.14 are shown in Table 4.2.

D_{min} [m]	D_{max} [m]	D [m]	Method 1		Method 2	
			Incremental rate $N(D)$ [yr^{-1}km^{-2}]	Cumulative rate $N(\geq D_{min})$ [yr^{-1}km^{-2}]	Incremental rate $N(D)$ [yr^{-1}km^{-2}]	Cumulative rate $N(\geq D_{min})$ [yr^{-1}km^{-2}]
3.9	5.5	4.7	$(1.3 \pm 0.4) \times 10^{-5}$	$(5.3 \pm 3.0) \times 10^{-6}$	$(8.8 \pm 3.9) \times 10^{-6}$	$(4.9 \pm 1.6) \times 10^{-6}$
5.5	7.8	6.6	$(8.0 \pm 3.3) \times 10^{-6}$	$(4.7 \pm 1.5) \times 10^{-6}$	$(3.9 \pm 1.0) \times 10^{-6}$	$(1.8 \pm 5.1) \times 10^{-6}$
7.8	11.0	9.3	$(3.3 \pm 0.8) \times 10^{-6}$	$(1.5 \pm 0.4) \times 10^{-6}$	$(2.1 \pm 0.4) \times 10^{-6}$	$(1.2 \pm 0.3) \times 10^{-6}$
11.0	15.6	13.1	$(1.8 \pm 0.4) \times 10^{-6}$	$(8.3 \pm 2.4) \times 10^{-7}$	$(9.6 \pm 2.6) \times 10^{-7}$	$(6.2 \pm 2.1) \times 10^{-7}$
15.6	22.1	18.6	$(9.6 \pm 2.6) \times 10^{-7}$	$(6.2 \pm 2.1) \times 10^{-7}$	$(3.4 \pm 1.5) \times 10^{-7}$	$(2.1 \pm 1.2) \times 10^{-7}$
22.1	31.2	26.3	$(3.4 \pm 1.5) \times 10^{-7}$	$(2.8 \pm 1.4) \times 10^{-7}$	$(1.4 \pm 0.9) \times 10^{-7}$	$(1.4 \pm 0.9) \times 10^{-7}$
31.2	44.2	37.1	$(6.9 \pm 6.9) \times 10^{-8}$	$(6.9 \pm 6.9) \times 10^{-8}$	-	-

Table 4.2: A comparison of the incremental and cumulative rates produced using Method 1 and 2 described in this chapter. D_{min} and D_{max} represent the left and right bin boundary respectively, and D is the bin centre.

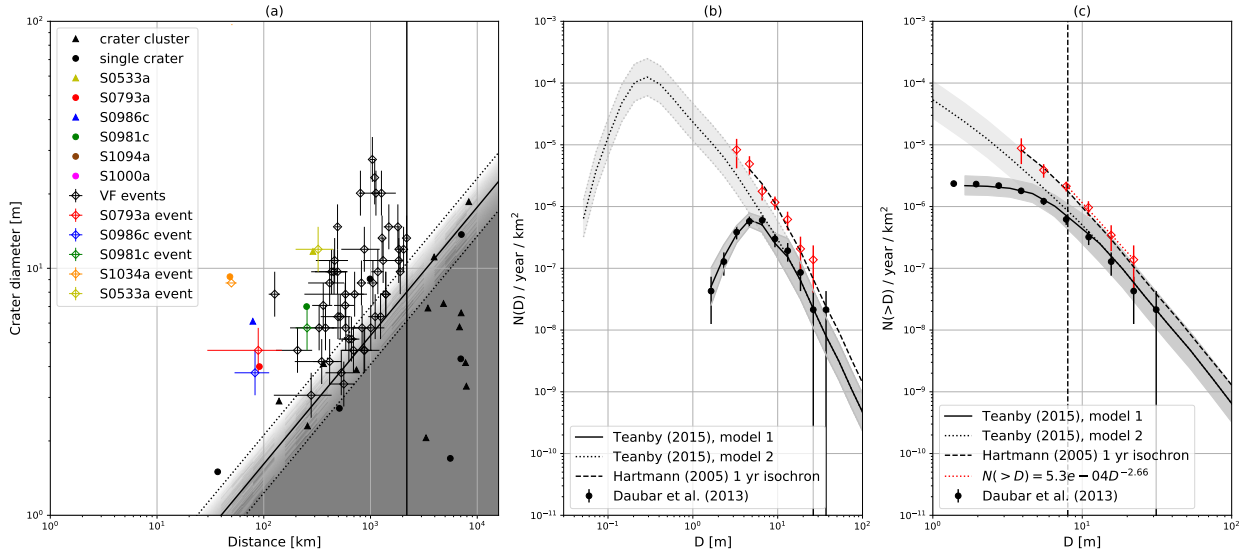

Figure 4.14: (a) The detectability of craters of a given diameter as a function of distance. The black circles and triangles are observed but not detected impact craters and crater clusters (respectively) that are constrained to have occurred during the InSight mission. The coloured filled in points are observed and detected craters and clusters, colour-coded by event name. The hollow diamonds in corresponding colours are the predicted crater sizes of detected impact events based on seismic moment magnitude. The black hollow diamonds show the distribution of predicted crater sizes for all other VF events. The solid black line indicates the detectability curve for noise amplitude of 2×10^{-11} m/s. This curve defined the Area Time Factor used to calculate impact rates up to a distance of 37°. Beyond that distance, no VF events are expected to be detected. (b) Incremental impact rates resulting from the distribution of predicted crater sizes for all VF events using seismic moment magnitude scaling shown in (a). The most recent imaging based rates from Daubar et al. (2014) are shown by black circles. The solid and dotted black lines show Teanby (2015) Model 1 and 2 respectively (with grey lines marking uncertainty). The dashed black line indicates the Hartmann (2005) 1-yr isochron (rescaled from 1 Gyr isochron). (c) Cumulative impact rates resulting from the distribution of predicted crater sizes for all VF events using seismic moment magnitude scaling shown in (a). The dashed line indicates the 8-m mark for comparison between studies.

4.3.3 Impact rates implications

The two methods for determining impact rate from a subset of events detected by InSight produce a distribution of predicted crater sizes in a similar range ∼3–40 m. Method 1 implies an impact rate higher than that of Daubar et al. (2013) by a factor of ∼5. Method 2 gives a rate only ∼3.5 times higher than that determined by Daubar et al. (2013). These results are consistent with a recent study Collins et al. (2022), which found that the impact rate of small impacts on Mars might be as high as 1.5–4 times higher than observational estimates. The least squares approximations to the cumulative rates derived imply that for impact crater diameters ≥8 m, between 565 (Method 1) and 295 (Method 2) impacts can be expected globally. The slope of the cumulative impact rate is approximately consistent with that of the Hartmann isochron and the slope determined by Daubar et al. (2022).

Method 2 predicts 4 out of 5 crater diameters correctly, compared to 3 out of 5 when using Method 1, implying that it is more appropriate for VF events dataset than Method 1. The differences between results of the two methods can be attributed to the difference in estimating the impact momentum for each event. In Method 1, the impact momentum (and therefore crater diameter) is estimated from a scaled amplitude at 2.4 Hz. Fig. 4.11 shows that there is some scatter in the impact data, which suggests that the scaling factor may not be a constant for all VF events, and may depend on the exact subsurface structure at each impact site. It is however difficult to predict its exact effects. Future studies should aim to reprocess the InSight data and extract the P-wave amplitude at the required frequency to test this relationship. On the other hand, Method 2 relies on a scaling relationship between seismic moment and crater diameter, calibrated by the confirmed VF events. Fig.4.13 shows that the data follows the same trend as the numerical modelling results, but the exact relationship will vary slightly depending on the subsurface structure.

The cumulative rate determined using Method 2 is within error bars of the Hartmann (2005) isochron. Assuming that the isochron represents the true rate of meteorite impacts on Mars, this implies that Method 2 provides a more robust workflow for estimating crater sizes from

seismic events than Method 1. The differences in the incremental rate can be explained by small number statistics, as the entire dataset considered here consists of only 57 events. On the other hand, Method 1 predicts an impact rate higher than the Hartmann (2005) isochron, which could imply that the scaling factors used to account for the difference in proximity to the asteroid belt and atmospheric effects between the Moon and Mars should be revised.

The method of using orbital observations to derive crater rates introduces several biases. Firstly, it assumes that all of the craters in the imaged area have been identified. According to Sidiropoulos and Muller (2015), only 61% of the martian surface has been imaged three or more times, with resolution finer than 20 m/pixel. This implies that many craters are likely missed by the orbital observations. Orbital detections of new craters are restricted to dusty areas, in which the low-albedo halo can be easily seen. Even in these areas topographic features, such as crater rims or shadow zones in interiors, may cause halos around some craters to be missed by human eye. This is further illustrated by novel machine learning techniques that have identified previously overlooked new craters in CTX data (Wagstaff et al., 2022). Additionally the orbiters do not take images of the same area at consistent intervals, meaning crater formation time can only be constrained to within months or years. This introduces further complication and could imply a systematic error in determining the ATF needed for scaling impact rates.

Seismic detections are independent of halo visibility of new craters and we can assume that all impacts above the detectability condition in the region around the receiver are detected. Seismic detections are also able to provide a more exact impact time. However, recognising impacts in seismic data unambiguously is challenging, as tectonic and impact generated events can be very similar in character. Additionally, seismic detectability of impacts is dependent on the noise level at the receiver, which has been shown to vary with time of day and season. The detectability is also sensitive to specific impact conditions, such as impact angle and potential atmospheric breakup, which were not investigated here.

Why so many more impacts were detected in the second year of InSight's operations than the first is debated. This is especially prominent given that two largest impacts recorded in the 16

years since MRO operations began (>100 m) were discovered just three months apart (Posiolova et al., 2022). The higher impact rate predicted by the VF events detected by InSight compared to both orbital imaging and isochron estimates could imply a recently increased impact rate. This could be related to a recent asteroid breakup in the vicinity of Mars, a comet stream, or a large impact into one of Mars' natural satellites causing ejecta to impact Mars. Such temporarily increased impact rate would not would not necessarily be reflected by crater counts from orbital imaging as temporal constraints on crater formation are usually long, of the order of months or years. The 1-year isochron is derived by assuming an unchanged impact rate over the most recent 1 Gy, so any short terms fluctuations in impact rate would not be reflected in those estimates. Further uncertainty is introduced by the scaling factor used to extrapolate lunar crater counts to Mars, to account for Mars' proximity to the asteroid belt.

The fact that the impact rates implied by the rate of VF events are higher than observation-based estimates suggests that if all VF events are impact related, then seismology can be a more effective tool for measuring the rate of meteorite impacts on Mars than orbital imaging alone. Furthermore, the cumulative seismic rates do not show a significant roll-off that is seen the orbital imaging based rate. This implies that InSight is able to detect smaller impacts than the resolution of satellite cameras permits, giving a better insight into the smallest crater production rate. However, at present, orbital imagery is necessary to identify an impact-generated seismic event unambiguously. Orbital images also provide important details of the source properties, which further inform the seismic analysis. If future missions to Mars establish more seismic stations on the planet's surface, the dataset of impact-generated seismic events can be expanded and the uncertainty in impact rate can be further reduced.

4.4 Conclusions

This chapter uses empirical peak P-wave amplitude scaling relationships to update pre-landing detectability estimates for impacts on Mars. P-wave amplitudes for impacts on Mars, Earth and the Moon scaled by impactor momentum show a clear trend with distance, where amplitude falls as $x^{-1.56}$. Compared with pre-landing approach of Teanby (2015), where the peak P-wave amplitude was scaled by impact energy, this approach implies that impacts smaller than 30 m in diameter are less detectable, but impacts producing craters larger than 30 m in diameter are more seismically detectable. The momentum-based approach also appears to be more consistent with the combined satellite observations of new craters and the seismically detected impacts (Fig. 4.10).

The unique properties of the VF family of events, and the fact that all nearby impacts detected by InSight to date belong to this family, imply that more or even all of those events could be impact related. This chapter presented two methodologies for predicting crater sizes of seismic events. Method 1 is based on converting peak P-wave amplitude into crater diameter using the amplitude-distance scaling relationship combined with *pi*-group crater scaling. Method 2 uses seismic moment magnitudes determined for the VF events, instead of amplitudes, and converts them into crater diameters using a scaling relationship based on simulation results from Chapter 3.

Method 1 predicts a slightly wider range of crater sizes (3-40 m) than Method 2 (3-30 m), leading to a higher and steeper impact rate than Method 2 and previous theoretical and observational estimates. When the cumulative impact rate is approximated with a power law of the form: $N(\geq D) = kD^{-b}$, the distribution of VF events returns $k = 9.4 \times 10^{-4}$ and $b = 2.64$. Method 2 on the other hand predicts an impact rate higher than the observational estimates but consistent within uncertainty with the Hartmann (2005) 1-year isochron. When approximated with a power law expression Method 2 returns $k = 4.2 \times 10^{-4}$ and $b = 2.29$. Whilst Method 1 predicts a steeper impact rate than Method 2, both gradients are comparable with previous estimates. These results show that seismology is a robust tool for measuring impact rates. Future seismic-

based missions to Mars and other bodies will improve upon this set of impact detections and provide more insight into the impact rates across the Solar System.

Chapter 5

Frequency content of impact-generated seismic signals

Parts of this chapter are based on Lunar and Planetary Science Conference abstract Wójcicka et al. (2022).

5.1 Introduction

5.1.1 Motivation and Aims

As described in previous chapters, identifying impacts in seismic data from Mars has proven challenging. This can be partially explained by the complex relationship between the signal/source properties and the impact properties. Some properties of seismic waves at very short timescales after the impact were linked to impact parameters in Chapter 3. However, one of the key properties used to classify seismic events on Mars, which was not considered in previous chapters, is the frequency content of the signal. This depends on a combination of the frequencies generated at the source and the properties of materials along the propagation path of the waves from source to the receiver.

In Daubar et al. (2018) the authors determined that impacts could follow the '−2 model', where the frequency spectrum is flat up to a cutoff frequency, and then decays with a power of −2 (described in more detail in Sec. 5.3 and shown in Fig. 5.2). Alternative models, such as the GL model, have shown that the high frequency decay may instead be proportional to f^{-3}. Depending on the form of the source time function used, the spectrum could show a high frequency overshoot, where the spectrum is flat at low frequencies, then increases to a peak amplitude at the cutoff frequency before sharply decaying at higher frequencies (Lognonné et al., 2009). Previous studies Gudkova et al. (2011) and Gudkova et al. (2015) used seismic data of impacts on the Moon to suggest that impacts exhibit a lower cutoff frequency when compared with shallow moonquakes. However, they also found that the cutoff frequency heavily depends on the geology of the impact site as well as the size of the impact. Schmerr et al. (2019) found that impact clusters show a higher cutoff frequency than single impacts, implying inverse dependence on impactor size.

Impact-generated seismic waves are also relevant to other bodies in the Solar System, such as asteroids. Impact-induced seismic shaking is a phenomenon observed on small asteroids, where the seismic waves generated during an impact event reverberate inside the target. These reverberations can affect the surface morphology of asteroids sometimes erasing small craters (Asphaug, 2008). Knowledge of the frequencies generated during impact is crucial to understanding this process. Richardson et al. (2020) used hydrocode simulations to generate synthetic seismograms and their power spectra for a range of slow impacts onto a 1-km wide asteroid target. These numerical experiments provided further insight into the dependence of the frequency content of impact-generated seismic waves on impactor size and target material.

This chapter aims to quantify the dependence of the frequency spectra of impact-generated seismic waves on the impact momentum, velocity, size and target material. This study represents the first step in linking the spectra of signals recorded at InSight to impact properties. Following the approach of Richardson et al. (2020), a suite impacts into a spherical asteroid target are simulated. The main advantage of using a spherical target, over a half-space similar to that used in Chapter 3 is the ability to track the seismic wave produced for a longer period of time needed to generate a frequency spectrum, without contamination from nonphysical

reflection from the mesh boundary. The final section presents the effect of applying a simple attenuation model to estimate the expected frequency content at a much larger distance, more relevant for Mars.

So far, 5 out of 7 impact detected by InSight were categorised as VF events, with the remaining two distant large impacts classified as BB events. Whilst the previous chapter explored the hypothesis that all VF events are impact related, it is important to consider the possibility that impact-generated seismic signals could take very different forms depending on exact impact conditions.

Since the frequency content is one of the main properties used to differentiate between different types of marsquakes, it is also a key characteristic that may be used to identify impact-generated signals in the data.

5.2 Modelling approach

In this study, the shock physics code iSALE2D is used to simulate a range of vertical impacts onto a suite of spherical targets. All simulations use a two-dimensional simulation mesh in cylindrical geometry. The spherical, asteroid-like target was chosen here to overcome computational difficulties related to simulating impacts-generated seismic waves for long periods of time. Modelling wave propagation from source to far-field seismic signals using a shock-physics code such as iSALE is very computationally expensive, as the mesh resolution is dictated by the small (sub-metre scale) size of the impactor. This results in an intractable number of cells across the simulation domain. A method like this also fails to account for the complex structure of Mars' interior. Furthermore, impacts onto a planetary surface are often modelled using a half-space geometry, which introduces nonphysical reflections from the boundary that contaminate the seismic signal. Such simulations can therefore only be extended until the P-wave reaches the mesh boundary, a timescale limited to usually less than 1 s for sub-metre to metre scale impacts. In order to avoid these reflections, a spherical target resembling a small asteroid can be used. The only reflections recorded in such geometry are due to the asteroid's surface,

which are physical and form part of the signal in this case. This study follows the approach of Richardson et al. (2020), who simulated impacts onto an asteroid target with SALES2 (Amsden et al., 1980; Collins et al., 2002; Collins et al., 2004) in order to investigate their frequency spectra.

Table 5.1: Impactor radius (r_i), vertical velocity (v_i) and target material for simulations into spherical asteroid targets. The first section contains simulation reproduced from Richardson et al. (2020) (Sec. 5.2.1). The second section contains additional simulations used to investigate the response of the frequency content to individual impact parameters.

Simulation number	Impactor radius, r_i [m]	Vertical velocity, v_i [m s^{-1}]	Target material
4_{simple}	2	100	elastic rock
60_{simple}	30	100	elastic rock
4_{bedrock}	2	100	intact rock
$4_{\text{fractured bedrock}}$	2	100	fractured rock
4_{regolith}	2	100	regolith
16_{bedrock}	8	100	intact rock
60_{bedrock}	30	100	intact rock
$4_{\text{800m/s}}$	2	800	intact rock
$4_{\text{6400m/s}}$	2	6400	intact rock

The following sections describe two parts of this chapter: the benchmarking against these original experiments (Sec. 5.2.1) and the extended suite of simulations used to determine the seismic signal's response to impact properties (Sec. 5.2.2).

5.2.1 Benchmarking against numerical experiments in SALES2

The first part of this study focused on reproducing two of the numerical experiments from Richardson et al. (2020) with iSALE2D. The two scenarios simulated vertical impacts of impactor diameters of 4 m and 60 m, onto a 1-km wide spherical target. These scenarios are listed in the top section of Table 5.1 as simulations 4_{simple} and 60_{simple}, respectively. The iSALE2D simulations in this work were run in Eulerian mode, where the material moves across a fixed simulation grid. This is in contrast to SALES2, a Lagrangian hydrocode used by Richardson et al. (2020), which distorts the simulation grid to follow material flow.

The impactor was resolved with 15 cells per projectile radius (CPPR) in the case of the 60 m impactor, and with 10 CPPR in the case of the 4 m impactor. The target resolution and

individual cell size depended on the size of the impactor. In the 60 m impactor simulation a cell width of 2 m in each direction was used, resulting in the total simulation domain of 250 cells in the horizontal direction and 500 cells in the vertical. In the smaller impactor simulation, the cell width was 0.2 m in each direction resulting in a simulation mesh of 2500 (horizontal) x 5000 (vertical) cells. The state of field variables in the mesh was saved at regular time intervals. In order to gain a higher temporal resolution record of wave propagation at a specific point in the target material, a Lagrangian probe was placed 2 m under the surface at the equator of the asteroid (Fig. 5.1). In particular, the probe measured displacement as a function of time, acting as a virtual seismometer. The simulation ran for 2 seconds after the impact, and the seismic wave was allowed propagate across the asteroid a number of times. Three snapshots of the simulation scenario 4_{simple} are shown in Fig. 5.1, where a P-wave front and the surface wave front can be seen.

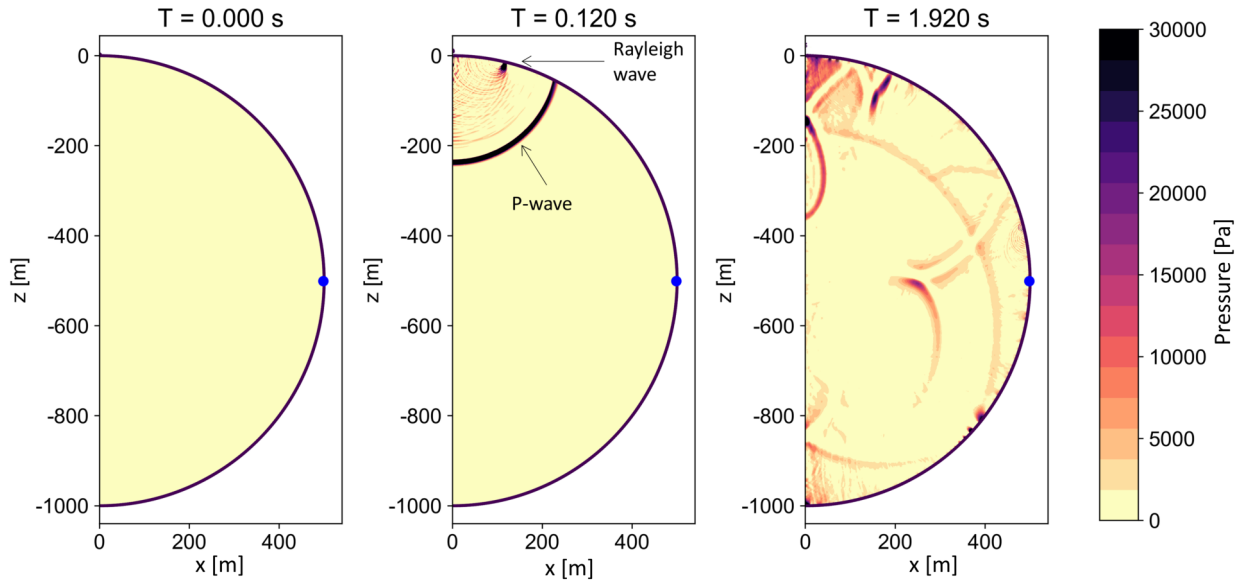

Figure 5.1: Three snapshots of a simulation of impact scenario 4_{simple} ($r_i = 2\,\text{m}$, $v_i = 100\,\text{ms}^{-1}$; Table 5.1) into an asteroid. Seismic waves can be seen progressing across the simulation mesh. The seismic signal is recorded using a virtual seismometer located at the equator of the target (blue dot).

The two simulations in this section used an 'elastic rock' material model to represent both the target and impactor, with parameters closely based on those used in the original study. This model approximates an 'infinitely strong' rock and allows us to investigate the elastic response of the asteroid. A Tillotson equation of state was adapted to match the specific parameters used

in Richardson et al. (2020) ('elastic rock' in Table 5.2). The equation of state was combined with the Lundborg strength model (Lundborg, 1968). This material model is suitable to study low velocity impacts, such as those reproduced from Richardson et al. (2020). Richardson et al. (2020) employed such low speeds in order to ensure stability of the Lagrangian simulation mesh in SALES2 and to investigate the elastic behaviour of the target material. Whilst these velocities are significantly smaller than those typical for impacts on Mars, Richardson et al. (2020) and Richardson and Kedar (2013) argued that impact velocity does not significantly affect the frequency content generated. For consistency with Richardson et al. (2020) most of the impact scenarios simulated here have impact speed of 100 m/s, however two additional speeds are also investigated to examine their effect on the produced spectra.

Table 5.2: Tillotson EoS input parameters[a] for basalt used in this work.

Material	ρ_0 [kg m^{-3}]	a	b	A [GPa]	B [GPa]	E_0 [MJ/kg]	α [MJ/kg]	β [MJ/kg]	E_{iv}	E_{cv}
Basalt[b]	2860	0.5	0.8	19.3	29.3	4.87	5	5	4.72	18.2
Elastic basalt [c]	2200	0.0	0.0	4.89	0.00	0.00	0.00	0.00	2×10^{99}	2×10^{99}

[a] For parameter descriptions see Tillotson (1962)
[b] Based on parameters given in Benz and Asphaug (1999),
but with revised reference density ρ_0, bulk modulus A, b and B parameters.
[c] Based on parameters used in Richardson et al. (2020).

5.2.2 Extended range of scenarios

In order to determine the effects of impactor and target properties on the frequency content of impact-generated seismic waves, a suite of additional simulations was run, where impactor size, velocity and target material were varied. A full list of impact scenarios is listed in the bottom section of Table 5.1.

This study considered three target materials (in addition to the idealised elastic material): porous regolith, fractured rock and intact rock, which were previously used to simulate small impacts on Mars in Wójcicka et al. (2020) and Rajšić et al. (2021). The full list of parameters used is shown in Table 5.3. The volumetric response of the target was described with an analytical Tillotson equation of state for basalt (see 'Basalt' in Table 5.2 in this thesis and Tillotson, 1962), combined with Lundborg strength model (Lundborg, 1968) in 'regolith', or

Table 5.3: Impactor and target material properties.

		Impactor	**Target**			
Parameter[a]		Non-porous rock	Elastic rock[b]	Intact rock[c]	Fractured rock[c]	Porous regolith[d]
Bulk density [kg m^{-3}]	ρ_0	2860	2200	2860	2150	1589
Bulk sound speed [m s^{-1}]	c_B	2598	1491	2598	1559	857
P-wave speed [m s^{-1}]	c_P	3302	2000	3302	1981	1100
S-wave speed [m s^{-1}]	c_S	1764	1154	1764	1059	583
Bulk modulus [GPa]	K_0	19.3	4.89	19.3	5.22	1.17
Shear modulus [GPa]	G_0	8.9	2.93	8.9	2.41	0.54
Poisson ratio	ν	0.3	0.25	0.3	0.3	0.3
LUNDD strength model parameters						
Internal friction coefficient	μ	0.7	0.6	-	-	0.6
Limiting strength [GPa]	Y_m	1	1×10^{90}	-	-	0.25
Cohesion [kPa]	Y_0	5	1×10^{90}	-	-	5
ROCK strength model parameters						
Internal friction coefficient (damaged)	μ_d	-	-	1.2	0.67	-
Limiting strength (damaged) [GPa]	Y_{dm}	-	-	3.5	0.17	-
Cohesion (damaged) [kPa]	Y_{d0}	-	-	10	0.2	-
Internal friction coefficient (intact)	μ_i	-	-	1.2	1.8	-
Limiting strength (intact) [GPa]	Y_{im}	-	-	3.5	0.17	-
Cohesion (intact) [kPa]	Y_{i0}	-	-	10	0.2	-
$\epsilon-\alpha$ **porosity model parameters**						
Initial distension	α_0	1	1	1	1.33	1.8
Initial porosity	ϕ_0	0	0	0	0.25	0.44
Elastic compaction threshold	ϵ_e	-	-	-	-4×10^{-4}	-2×10^{-4}
Transition distention	α_x	-	-	-	1.1	1.2
Exp. compaction rate	κ	-	-	-	0.98	0.98
Sounds speed ratio	χ	-	-	-	0.60	0.33

[a]Descriptions of material model parameters can be found in Collins et al., 2004; Wünnemann et al., 2006; Collins et al., 2011.
[b] Material model based on Richardson et al., 2020.
[c] Material model based on Rajšić et al., 2021
[d] Material model based on Wójcicka et al., 2020

ROCK strength model (Collins et al., 2004) in 'intact rock' and 'fractured rock'. The porous materials ('fractured rock' and 'regolith' in Table 5.3) also used an $\epsilon-\alpha$ compaction model. Because the results of this works are intended to be extrapolated specifically to Mars, the 'intact rock' was chosen as the default target material. Both impact scenarios from the previous section were repeated in this target (4_{bedrock} and 60_{bedrock}). The range of impactor sizes expected to be the most relevant for InSight are between few centimetres to ~2 m in diameter (Daubar et al., 2018; Wójcicka et al., 2020). Simulating impacts of this size at a reasonable resolution would require a very large number of cells, rendering the simulation time unsustainable. Instead, the 4-m impactor was chosen as the benchmark scenario. The recorded response to different

impact parameters can be used to infer the frequency spectrum of impactors in the range more appropriate for Mars.

To investigate the effects of impactor size on the frequency spectrum, the impact scenarios list was extended to include an intermediate impactor radius of 8 m (16_{bedrock} in Table 5.1). To determine the effect of target material scenario 4_{bedrock} was then repeated in the remaining two target variants. The response of the frequency spectrum to impact velocity was studied by increasing impact speed of scenario 4_{bedrock} to 800 m/s and 6400 m/s.

5.3 Methods

This section describes the data processing methods used to calculate frequency spectra of displacement seismograms recorded for impact scenarios in this study. To illustrate the data analysis procedure the two simulations reproduced from Richardson et al., 2020 are used: 4_{simple} and 60_{simple} (Table 5.1).

5.3.1 Benchmarking against numerical experiments in SALES2

As described in Sec. 5.2, for each simulation a Lagrangian probe placed at the equator 2 m below the surface. The probe measured displacement as a function of time, saving the data at every time step of the simulation. In iSALE, the time step length varies throughout the simulation according to the Courant–Friedrichs–Lewy (CFL) condition, where the timestep is limited to the time for a sound wave to travel across $\frac{1}{5}$ of the smallest cell dimension in the simulation domain. For the purposes of time series analysis it is important that samples are equally spaced in time, hence the output time series was down-sampled to $dt = 2 \times 10^{-4}$ s, resulting in a total of 15,000 samples. This was chosen to match the temporal resolution used in Richardson et al. (2020).

Figures 5.3(a) and (c) show the resulting horizontal and vertical displacement seismograms for the 4-m and 60-m impact, respectively. For the smaller impact scenario, the first (P-wave) arrival is seen at ∼0.3 s, followed by an S-wave at ∼0.6 s and a surface (Rayleigh) wave at ∼0.75 s. In the case of the 60-m impact, the seismic amplitudes are significantly higher and it can be qualitatively seen that the frequency of the signal is much lower than in the case of the smaller impactor. This suggests that the frequency content is inversely proportional to the impactor size. The seismogram is dominated by the surface wave and hence it is difficult to resolve individual arrivals.

Figures 5.3(b) and (d) show the power spectra of the seismograms in a and c, respectively, compared with the vertical spectra of Richardson et al. (2020). The Power Spectra Density

(PSD) is calculated for each seismogram between 0.5 to 2500 Hz with frequency resolution of 0.5 Hz are calculated using Welch's PSD method with 50% overlap between Hanning-windowed segments.

In order to quantitatively investigate the dependence of the power spectrum on impact conditions, the PSD is assumed to follow a '-2 model', where the amplitude in the frequency domain remains 'flat' until a 'corner frequency' f_c (Brune, 1970; Aki and Richards, 2002). For frequencies higher than f_c, the spectrum amplitude decreases as f^{-2}, defined by the following equation:

$$A(f) = \frac{A_0}{1 + \frac{f^2}{f_c^2}} \tag{5.1}$$

where the constant A_0 is the low frequency plateau amplitude in $\mathrm{mHz}^{-1/2}$, that is linked to the seismic moment. By using this simple expression, the PSD can be expressed with just 2 free parameters: A_0 and f_c, as illustrated in Fig. 5.2.

The smaller impact shows a higher corner frequency of about 200 Hz and significantly more energy than the SALES2 simulation at higher frequencies beyond 200 Hz. This can be attributed to high-frequency noise recorded in the iSALE simulation, which could have been caused by the higher spatial resolution used in the iSALE simulation compared with the SALES2 simulation. The normalised power spectrum is consistent with the results of Richardson et al. (2020) at low frequencies, whilst showing slightly higher corner frequency and more energy at higher frequencies. The larger impact shows a frequency content consistent with Richardson et al. (2020), with corner frequency of approximately 10 Hz. In this case, the spectrum shows much less energy at frequencies beyond 100 Hz compared with the results of Richardson et al. (2020). This could reflect the fact that the 60-m impact was simulated with a much larger cell size than the one used in the SALES2 simulation.

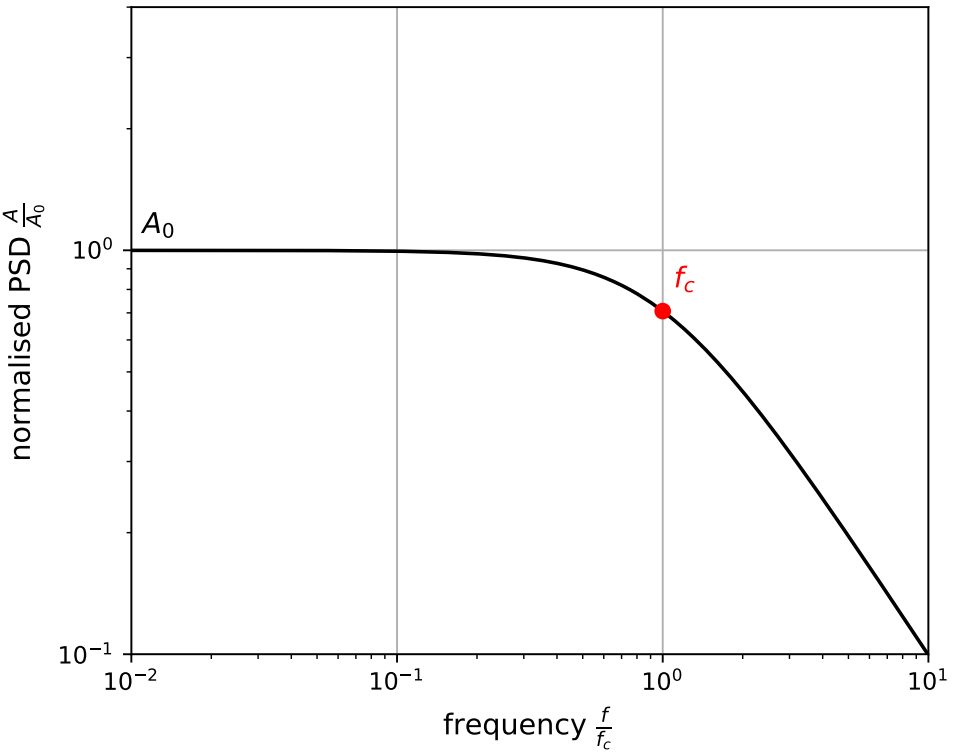

Figure 5.2: A normalised power density spectrum represented by equation 5.1. The amplitude, measured in m, has been normalised by A_0 (the low frequency amplitude plateau) and frequency has been scaled to f_c (the corner frequency). The f_c is marked with the red circle, and is equivalent to where the amplitude has decreased by a factor of $\sqrt{2}$.

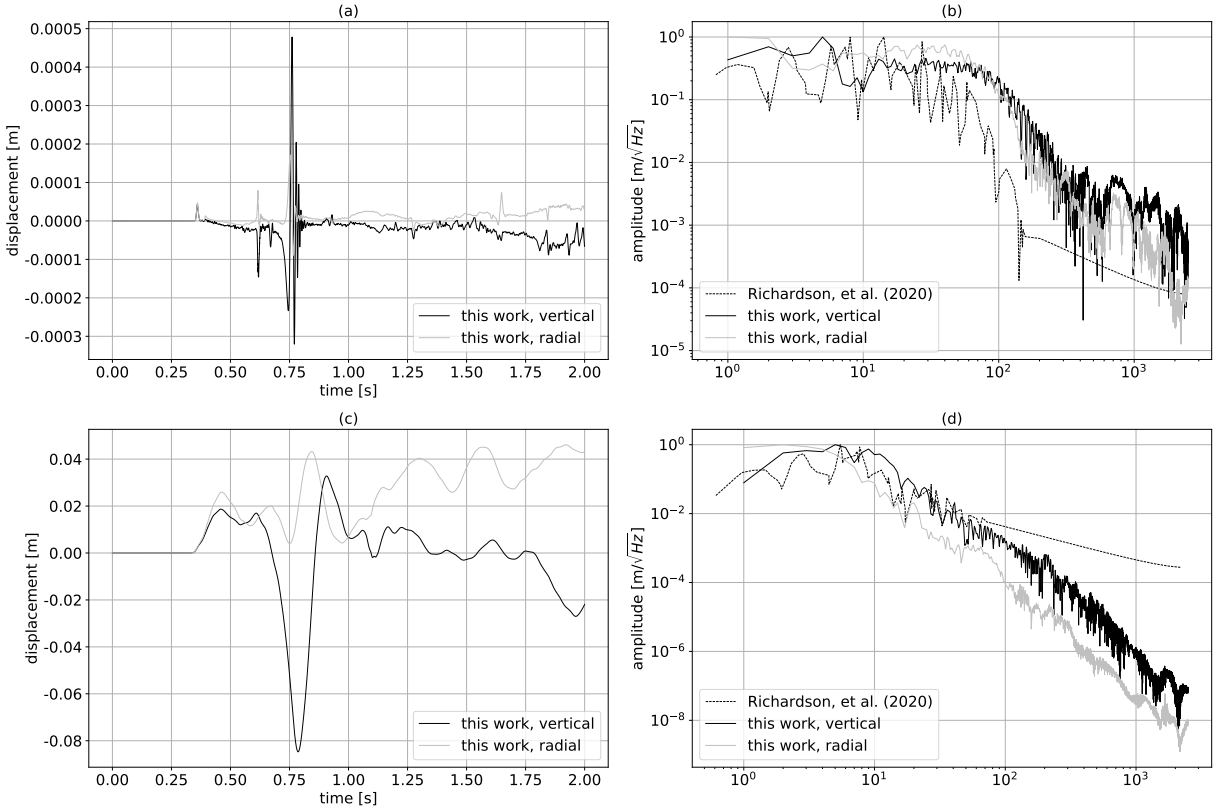

Figure 5.3: Vertical (black lines) and radial (grey lines) seismograms recorded from iSALE simulation of (a) a 4-m impact and (c) 60-m impact, reproduced from Richardson et al., 2020, and their respective normalised power spectra (b) and (d). The power spectra and the seismic trace for the smaller impact are compared with numerical simulations results from Richardson et al. (2020) (dashed lines) for the same impact scenario recorded in the vertical component.

5.3.2 Extended range of scenarios

The same procedure, as described the in the previous section, for extracting the seismic record from iSALE output and computing its PSD was followed when processing the remaining simulations in this chapter.

A least squares regression was performed on all 7 simulations in the bottom section of Table 5.1 to find the best fit values both parameters in equation 5.1. Fig. 5.4 shows the displacement in both radial and vertical directions for the example simulation 4_{bedrock}. The R^2-values for this scenario were 0.90 and 0.96, respectively, indicating a good fit to data.

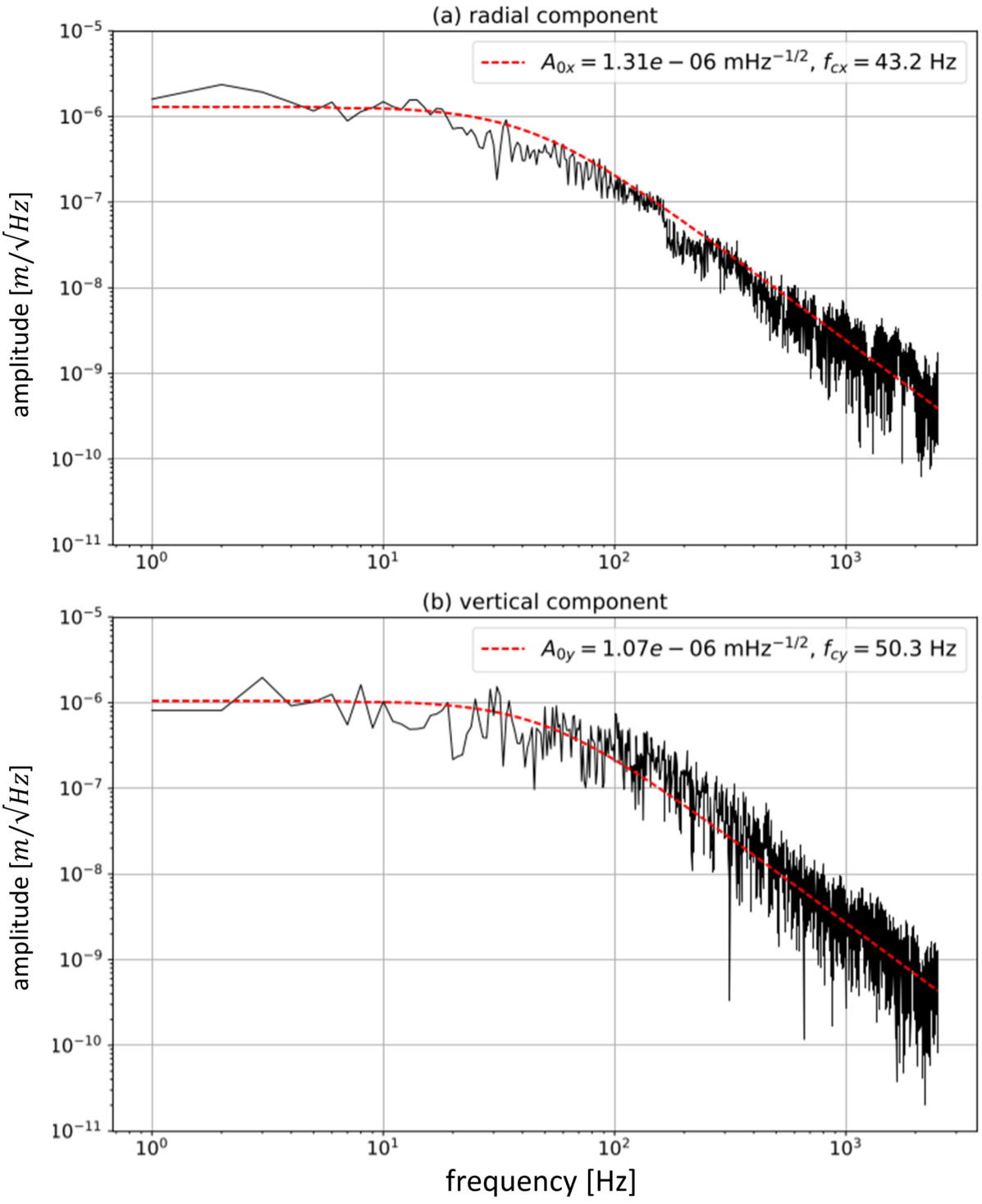

Figure 5.4: The horizontal (a) and vertical (b) PSD recorded at the equator of the 1-km wide asteroid for the 4-m impactor striking an intact bedrock target at 100 ms^{-1}. Each component was fitted with equation 5.1 and least squares results are shown as red lines on both panels.

5.4 Results

The post-processing methodology described above was repeated on the remaining simulations in Table 5.1. The power spectrum measured at the equator was characterised for each impact scenario using the two parameters in equation 5.1 and the complete results are shown in Table 5.4.

Table 5.4: Complete results for all simulations.

Simulation	Impact momentum p_i [kgm/s]	Impact energy E_i [J]	Corner frequency f_{cx} [Hz]	Corner frequency f_{cy} [Hz]	Low-frequency amplitude A_{0x} [mHz$^{-1/2}$]	Low-frequency amplitude A_{0y} [mHz$^{-1/2}$]
4_{bedrock}	9.6×10^{6}	4.8×10^{8}	43.2 ± 0.6	50.3 ± 1.0	(1.31 ± 0.01)×10^{-6}	(1.07± 0.02)×10^{-6}
$4_{\text{fractured bedrock}}$	9.6×10^{6}	4.8×10^{8}	10.6 ± 0.1	12.5 ± 0.2	(3.78 ± 0.01)×10^{-6}	(1.25 ± 0.03)×10^{-6}
4_{regolith}	9.6×10^{6}	4.8×10^{8}	2.3 ± 0.1	1.6 ± 0.1	(5.78 ± 0.06)×10^{-6}	(9.57 ± 0.10)×10^{-6}
16_{bedrock}	6.2×10^{8}	3.1×10^{10}	8.4 ± 0.1	10.2 ± 0.1	(4.95 ± 0.03)×10^{-5}	(2.23 ± 0.01)×10^{-5}
60_{bedrock}	3.3×10^{10}	1.6×10^{12}	3.7 ± 0.1	5.8 ± 0.1	(1.17 ± 0.01)×10^{-3}	(2.97 ± 0.05)×10^{-4}
$4_{\text{800m/s}}$	7.7×10^{7}	3.1×10^{10}	17.8 ± 0.2	27.0 ± 0.4	(1.59 ± 0.01)×10^{-5}	(5.63 ± 0.06)×10^{-6}
$4_{\text{6400m/s}}$	6.2×10^{8}	1.2×10^{12}	4.9 ± 0.1	6.8 ± 0.1	(3.05 ± 0.01)×10^{-4}	(1.69± 0.02)×10^{-4}

Fig. 5.5 shows the approximated frequency spectra, fitted using equation 5.1, with the best-fit corner frequency and long-period amplitudes listed in Table 5.4. The R^2 values for all simulated scenarios ranged between 0.82 - 0.98 indicating a good fit. In particular, all signals closely followed a high frequency fall-off proportional to f^{-2}. Each panel shows the response of the signal to a single impact parameter, with all the other parameters kept constant. The behaviour of each parameter in equation 5.1 with respect to impactor and target properties were quantified by least squares approximations shown in Fig. 5.6 and 5.7.

The results show that the larger the impactor size, the lower the corner frequency of the spectrum (Fig. 5.5a). This is consistent with the observations of Richardson et al. (2020) and simulations reproduced from that study in the first part of this chapter. Increasing the impactor radius by a factor of 4 results in corner frequency lower by a factor of ∼2.5 and 4 in the horizontal and vertical directions, respectively. The impactor in scenario 60_{bedrock} has the highest kinetic energy, so more energy is transferred into the seismic signal, which is illustrated by the larger area under the displacement spectrum in Fig. 5.5a. Figure 5.6a shows a least-squares fit to the corner frequency for those three impact scenarios. The vertical and horizontal corner frequency follows a clear power law with impactor size, with the vertical component decreasing at a faster

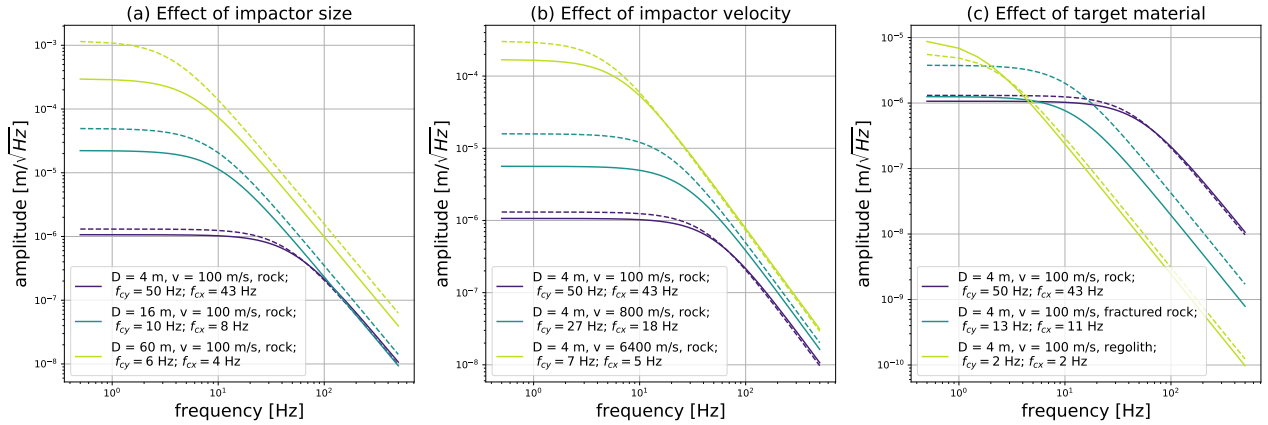

Figure 5.5: Power spectrum density approximations for simulations in Table 5.1, showing the effects of individual impact properties: (a) impactor size, (b) impact velocity, (c) target material. The solid lines show the vertical component and the dashed lines represent the horizontal component of ground motion.

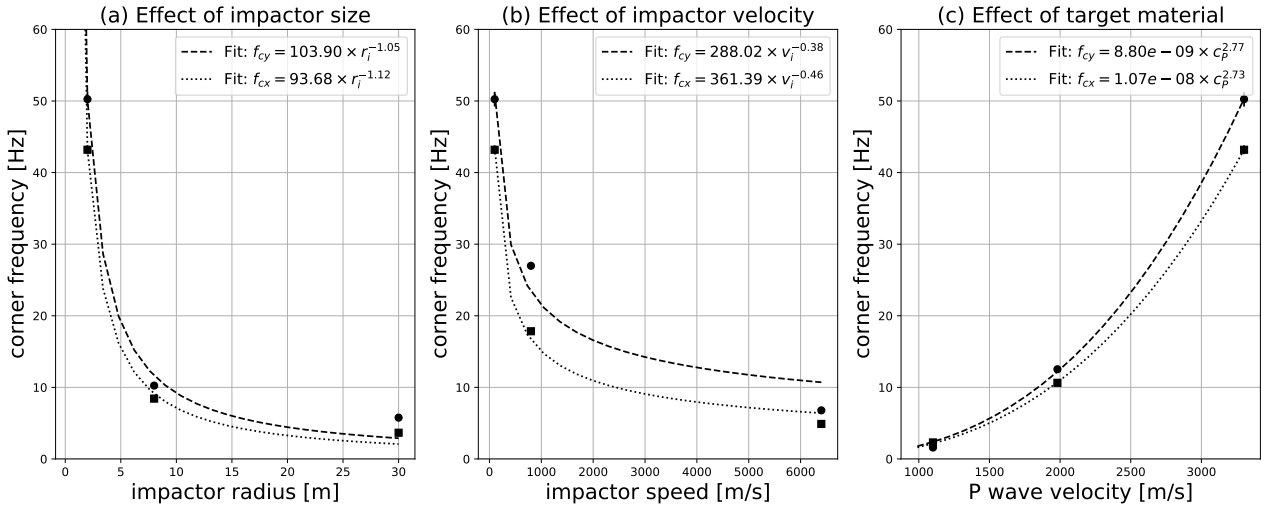

Figure 5.6: Vertical (circles) and horizontal (squares) corner frequency as a function of each investigated parameter: (a) impactor size, (b) impact velocity, (c) target material represented by the P-wave velocity for porous regolith, fractured bedrock and intact bedrock, as shown in Table 5.3. Dashed and dotted lines show a least squares fit to vertical and horizontal components respectively.

rate than the horizontal and being approximately inversely proportional to r_i.

Secondly, the higher the impact velocity, the lower the corner frequency of the impact-generated seismic signal. Figure 5.5b shows increasing the impact velocity by a factor of 64 (from 100 ms^{-1} to 6400 ms^{-1}), for meteorites of the same size ($r_i = 2$ m) reduced the corner frequency of the displacement signal by a factor of 4.5 in horizontal component and a factor of 4 in vertical component. This is in contrast to previous studies Richardson and Kedar (2013) and Richardson et al. (2020), who suggested that the corner frequency is independent of impact velocity. As

shown in Fig. 5.6b the corner frequency follows a power law with impact velocity, similar to the relationship with impactor radius. The corner frequency decreases with v_i at a slower rate than with r_i, suggesting that the effect of impactor size is dominant.

The final impact parameter considered here is the target material. Figure 5.5c shows that impacts onto a more porous and less cohesive target exhibit a lower corner frequency. Whilst the overall energy in the signal is higher for impacts onto non-porous bedrock (due to higher seismic efficiency, see Rajšić et al. (2021)), the energy is distributed across broader range of frequencies, up to ∼100 Hz. Impacts onto porous regolith transfer less energy into the seismic signal, but majority of the energy is concentrated at low frequencies below 3 Hz. As shown in Fig. 5.6, both vertical and horizontal corner frequency scales as a power law with the P-wave velocity in the target material, with the vertical component increasing at a steeper rate than the horizontal.

The scaling relationships shown in Fig. 5.6 allow for extension of this work to a range of other impact scenarios. For a nominal impact scenario, where an impactor of radius r_i strikes a target of P-wave velocity c_P at vertical velocity v_i, the vertical corner frequency can be calculated by combining the effects of the three parameters studied here. The corner frequency can be scaled from scenario $4_{bedrock}$ by a series of scaling factors:

$$f_{cy,(r_i,v_i)} = f_{cy,(2\text{ m},100\,\text{ms}^{-1})} \times \left(\frac{r_i}{2\text{ m}}\right)^{-1.05} \times \left(\frac{v_i}{100\,\text{ms}^{-1}}\right)^{-0.38} \times \left(\frac{c_P}{3302\text{ ms}^{-1}}\right)^{2.77}, \tag{5.2}$$

where r_i is given in m, v_i in ms^{-1} and c_P in ms^{-1}.

In the horizontal direction this equation becomes:

$$f_{cx,(r_i,v_i)} = f_{cx,(2\text{ m},100\,\text{ms}^{-1})} \times \left(\frac{r_i}{2\text{ m}}\right)^{-1.12} \times \left(\frac{v_i}{100\,\text{ms}^{-1}}\right)^{-0.46} \times \left(\frac{c_P}{3302\text{ ms}^{-1}}\right)^{2.73}. \tag{5.3}$$

These scaling relationships can be used to predict the approximated power spectrum for a given impact, based on its properties relative to those of scenario 4_{bedrock}, measured at a distance of 800 m.

The long period plateau amplitude is inherently related to seismic moment, which was found to scale almost linearly with impact momentum (Chapter 3). Consequently, it follows that A_0 should also scale with impact momentum. Fig. 5.7 shows the horizontal and vertical A_0 as a function of impact momentum for all simulations. The least squares approximation for the relationship between amplitude and impact momentum is given by:

$$A_{0y} = 1.13 \times 10^{-11} p_i^{0.77}, \tag{5.4}$$

in the vertical component. Analogously, in the horizontal direction this relationship becomes:

$$A_{0x} = 3.96 \times 10^{-12} p_i^{0.83}. \tag{5.5}$$

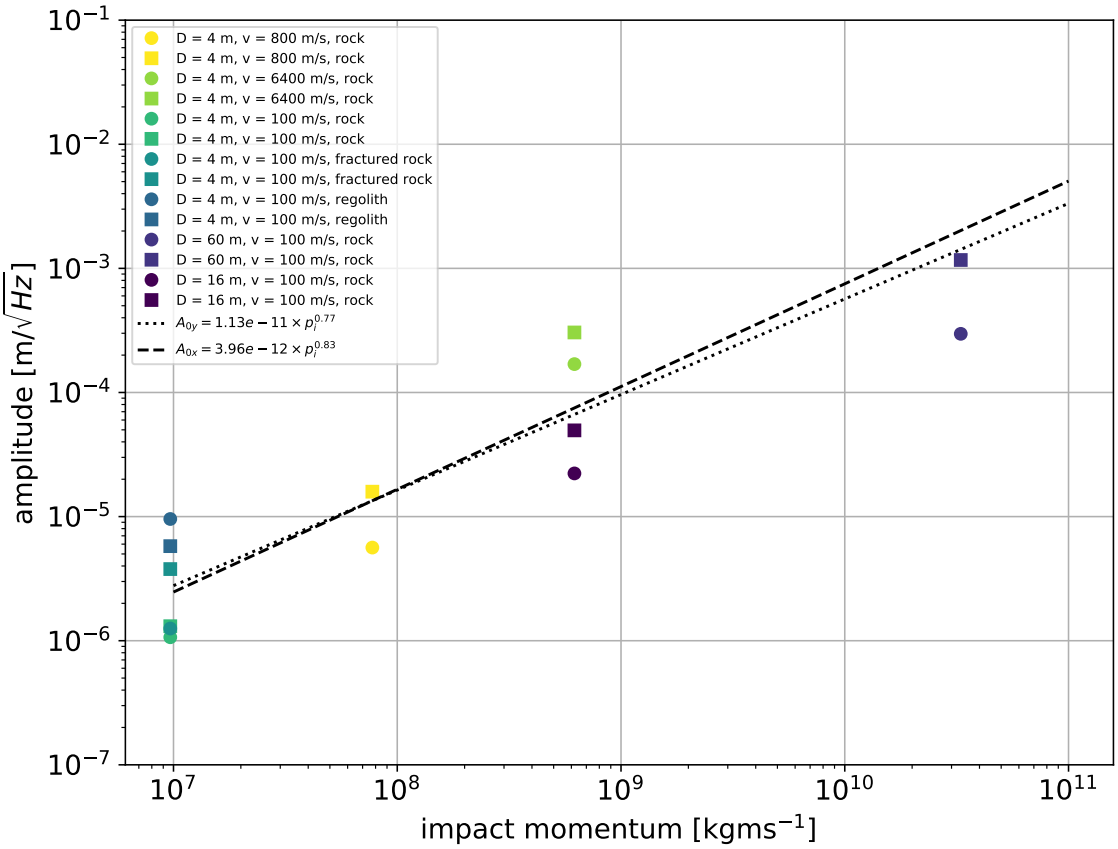

Figure 5.7: Vertical (circles) and horizontal (squares) low frequency amplitude A_0 as a function of impact momentum for all simulated scenarios. Dotted and dashed lines show a least squares fit to vertical and horizontal components respectively.

Whilst a clear trend can be seen where A_0 in both components increases with increasing impact momentum, there is some variation due to other impact parameters. For impacts of the same momentum into a porous regolith target, the amplitude of the low-frequency signal (measured in displacement) is up to 10 times higher than for an impact into intact bedrock. Therefore, the resulting scaling relationship, which was derived from results of impacts into all targets, is the most appropriate for impacts into the intermediate strength, fractured bedrock material. In the case where impact momentum ($6\times10^8\,\mathrm{kgms^{-1}}$) and target material (intact bedrock) are the same, but one impactor is larger (16_{bedrock}) and the other faster ($4_{6400\mathrm{m/s}}$), the faster impact will generate the higher amplitude. In this case the amplitude is approximately 1 order of magnitude higher, which suggests that more impact scenarios need to be simulated.

5.4.1 Frequency content of impacts at large distances and implications for InSight

The previous section presented an investigation of the effects of individual impact parameters on the displacement spectra measured at $\sim$ 800 m from impacts that produce craters up to 100 m in diameter. To date, the closest marsquake recorded by InSight (event S1034a) was estimated to be at a distance of 0.8 ° ($\approx$50 km) from a crater $\approx$ 9 m in diameter, implying that real seismic impact detections are likely to emanate from sources at much larger distances than those used in simulations in this chapter. At such distances other factors that influence the frequency content and amplitude of the signal become significant. This section investigates how signals produced by small impacts would vary if the propagation distance was extended.

In late 2021, four Very High Frequency (VF) events recorded by InSight (S0533a, S0793a, S0981a, S0986c following standard MQS nomenclature) were attributed to impacts (Garcia et al., 2022). These events are the first impacts to be seismically detected on another planetary body outside Earth and the Moon, and as such offer a unique opportunity to test the scaling relationships presented in this chapter. Statistical modelling of the atmospheric passage of meteoroids was performed to determine the most likely meteoroid parameters responsible for the the observed crater size, as detailed in the previous chapter (Table 4.1 in this thesis, and

Garcia et al., 2022). Two of these impact events (S0793a and S0986c) are considered in this chapter for the purpose of comparison to modelling results.

Firstly, a simple geometric spreading factor is applied, assuming that the amplitude of seismic waves decreases as $1/x$, where x is distance in km. This factor results in decrease of A_0 with propagation distance. To account for effects of attenuation, an average quality factor Q, defined in seismology as a measure of energy loss per oscillation cycle, is assumed to be between 2000–3500 for martian crust (Garcia et al., 2022). The crust is the most relevant here as impacts are superficial sources, which results in trapping of seismic waves in the crust. Moreover, the impact events considered here are located in close proximity ($< 40°$) to InSight, and hence the propagation path is likely to be dominated by the crust.

When the two effects described above are combined, the spectra in this work $A_1(f, x_1)$, recorded at a distance x_1 away from the source, can be scaled by the following expression to compute the amplitude spectrum $A_2(f, x_2)$ at a distance x_2:

$$A_2(f, x_2) = A_1(f, x_1)\frac{x_1}{x_2}e^{\frac{-\pi f(x_2 - x_1)}{cQ}} \tag{5.6}$$

where c is the wave velocity, assumed assume to be a constant value of $4000\,\mathrm{ms}^{-1}$ (Garcia et al., 2022).

Fig. 5.8 shows an example of applying the above equation to scenario $4_{6400\mathrm{m/s}}$, which approximates an impact into an intact bedrock target. The amplitude is reduced across all frequencies. At low frequencies, attenuation can be considered negligible and the amplitude decrease is primarily due to geometric spreading, whilst at high frequencies attenuation is the dominant effect. The resulting spectra suggest that at 1000 km such an impact would be expected to produce seismic signal containing frequencies smaller than 10 Hz.

Each HF-family event recorded by InSight is approximated with the following expression:

$$A(f) = A_{0,\mathrm{receiver}}\frac{1}{1 + \left(\frac{f}{f_c}\right)^2}e^{-\pi f t^*}, \tag{5.7}$$

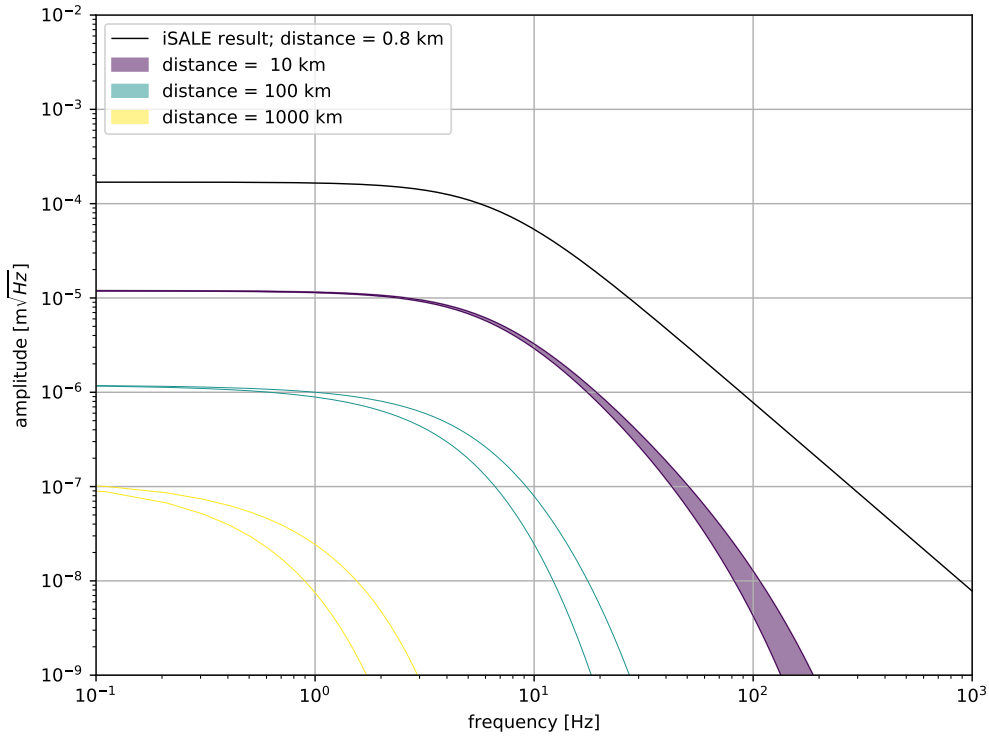

Figure 5.8: Power spectrum density scaled with distance from source for a 4-m impactor striking an intact bedrock target at 6.4 kms^{-1}. The seismic signal is measured at a distance of 800 m (black line). It is scaled using equation 5.6 to distances: 10 km (purple lines), 100 km (green lines) and 1000 km (yellow lines). The shaded areas represent the range of amplitudes possible due to the range of quality factors used.

where A_0 represents the low frequency plateau in mHz$^{-1/2}$, f_c is the corner frequency of the source and t^* is a parameter accounting for attenuation of high frequency as the seismic waves travel through the planet. t^* ranges from 0.05 to 0.5 s for VF events (Böse et al., 2021). Additionally, events in the HF family contain an amplified peak at 2.4 Hz of amplitude $A_{2.4\text{Hz}}$. This peak is separately fitted with the expression for Lorentz curve:

$$u(f) = \frac{A_{2.4\text{Hz}}}{1 + \left(\frac{f - f_0}{w}\right)^2}, \tag{5.8}$$

where $f_0 = 2.4$ Hz is the central frequency of the peak and w is the width of the peak.

Event S0793a was determined to be associated with a 3.9 m crater formed 91 km away from the lander. The most probable impactor radius was determined to be 0.096 m with vertical impact velocity 2807 ms^{-1} (see Table 4.1 in this thesis or Garcia et al., 2022, for list of other properties). Using the scaling relationship 5.2 determined in previous section, the vertical corner frequency

for S0793a at a distance of 800 m away from source is estimated to be 344 Hz for an impact in intact bedrock, 82 Hz in fractured bedrock and 18 Hz in porous regolith (dashed lines in Fig.5.9a). The low frequency plateau amplitude $A_{0y} = 1 \times 10^{-7}$ mHz$^{1/2}$ for an impact onto a fractured bedrock target. Due to the spread of data for various target materials, a factor of 2 difference in amplitude was assumed between fractured and intact bedrock, and between fractured bedrock and porous regolith targets. When the simple attenuation scaling is included, the vertical corner frequency range becomes: 5 Hz–10 Hz. The low-frequency amplitude is lowered to $A_{0,\text{receiver}} = 8 \times 10^{-10}$ mHz$^{1/2}$ for a fractured bedrock target. The final spectra are shown as solid lines and shaded areas in Fig. 5.9a. The power spectrum of the signal measured at InSight is shown for comparison as a black solid line. The f_{cy} range predicted here is slightly (approximately a factor of 2) higher than the measured corner frequency for this event (2.2 Hz). The amplitudes predicted for all three target materials here are between 1–1.5 orders of magnitude larger than the measured amplitudes.

Event S0986c was associated with a crater cluster discovered 85 km away from InSight, with an effective diameter of 6.1 m (see Table 4.1). The most probable impactor radius to produce the largest crater in the cluster (5.7 m) was determined to be 0.152 m with vertical impact velocity of 2068 ms^{-1} (see Table 4.1 in this thesis or Garcia et al., 2022, for list of other properties). The estimated corner frequency for event S0986c at a distance of 800 m is 240 Hz for an impact in intact bedrock, 57 Hz in fractured bedrock and 13 Hz in porous regolith (dashed lines in Fig. 5.9b). The low frequency plateau $A_{0y} = 3 \times 10^{-7}$ mHz$^{1/2}$ for an impact onto a fractured bedrock target. When the attenuation scaling is included the vertical corner frequency becomes: 5–20 Hz, depending on target material. The low-frequency plateau amplitude becomes $A_{0y} = 1.5 - 6 \times 10^{-9}$ mHz$^{1/2}$. The final spectra are shown as solid lines in Fig. 5.9a. The f_{cy} values are comparable with the measured corner frequency for this event (10 Hz). For this event, the amplitudes predicted in this chapter are also approximately two orders of magnitude larger than those measured at the landing site.

The differences in the case of S0986c could be attributed to the complexity of the cluster event, which contained over 7 craters (Garcia et al., 2022). The above calculation only takes into account the largest crater in the observed in the cluster, whilst seismic signals generated

by crater clusters are expected to show higher frequency content than those of single craters (Schmerr et al., 2019). Future studies should improve on this result for more complex impact events, such as clusters or very oblique cases.

Whilst for both impacts considered here the corner frequencies are predicted in the correct range compared to measured signals, the amplitudes predicted are significantly higher than those measured by InSight. This effect is the opposite to the results of Chapter 3, which found that the seismic moment amplitudes derived from numerical source simulations are consistently lower than those measured by InSight. A possible explanation for the discrepancy is the fact that the seismograms used to produce the spectra in this chapter include a surface wave, of several times higher amplitude than the P and S waves. No surface wave was recorded by InSight for the seismic events considered above. Because of the short time separation between seismic phases, it would be difficult to separate this part of the signal from the rest in the simulated seismograms. Additionally, in order to produce spectra spanning a wide range of frequencies, the total length of signal of 2 seconds was required. This could have increased the value of A_0 in the simulated scenarios. Future studies should further investigate the frequency content of specific seismic phases generated during impact.

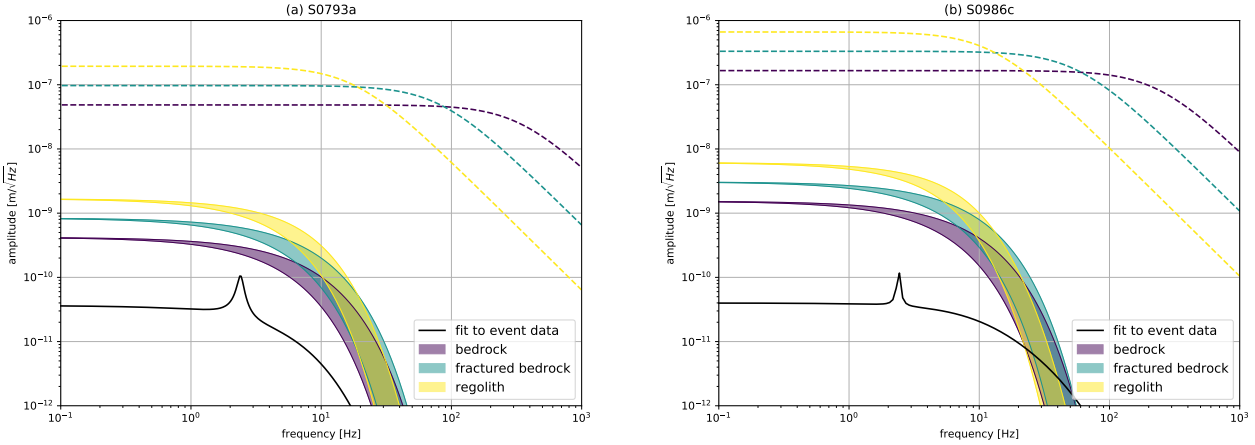

Figure 5.9: Predicted power spectrum densities for two of the recently detected impact events: (a) S0793a, produced by a 3.9-m crater 91 km away from InSight, and (b) S0986c, caused by a crater cluster formed 85 km from InSight. The dashed coloured lines show the predicted PSD at 800 m from the source, whilst the solid lines mark the predicted PSD at the true distance between impact crater and InSight (91 and 85 km, respectively). The shaded area shows the variation in amplitude with the range of Q values used here.

InSight's seismic package Seismic Experiment for Internal Structure (SEIS) consists of two

seismometers: Short Period (SP) and Very Broad Band (VBB). The sensitivity range of these sensors extends from 0.01 Hz to 50 Hz. The noise levels at the lander's location vary over the course of day, with quietest time in the early evening until midnight Local Mean Solar Time (LMST) (Lognonné et al., 2019). The lowest noise is observed at frequencies between 0.1 - 1 Hz. At higher frequencies the noise increases significantly, due to the lander noise excited by wind. This study has shown that sub-metre-scale impacts are likely to deposit a large portion of their seismic energy into the high frequencies of the order of 10 Hz, or higher if the source is in denser material such as bedrock. This could lead to lower than expected detectability of impacts in a number of ways. Firstly, high-frequency signals are likely to be more heavily attenuated over large distances, with less overall energy arriving at the receiver, making those signals less detectable. Secondly, even for a local event where attenuation effects are small, the amplitude of the signal needs to be higher to be detectable, due to higher noise at short periods. This suggests that impacts of sub-metre to metre scale are less likely to be detectable at InSight than larger, less frequent impacts.

Recent work has shown that impacts onto less porous and stronger targets transfer more of their kinetic energy into seismic waves (Güldemeister and Wünnemann, 2017; Rajšić et al., 2021). Such impacts would produce higher amplitude seismic waves and hence be more detectable than impacts onto porous regolith targets. However, simulations in this chapter show that, whilst more energy is transferred to the seismic waves in impacts onto exposed bedrock, the additional energy is deposited into higher frequency oscillations (above 10 Hz). This means that the low frequency amplitude plateau (A_0) is likely to be lower for an impact of the same energy onto bedrock than porous regolith. These results could partially explain lack of impact detections in the first year of observations.

5.5 Conclusions

This study used a suite of iSALE shock physics code simulations to compute displacement frequency spectra for several impact scenarios. The impacts considered were onto a 1-km wide spherical asteroid. The displacement recorded by a virtual seismometer was measured at a distance of ≈800 m away and the resultant power spectrum approximated with a two-parameter expression. The first part of this study was used to benchmark iSALE results against those from previous numerical experiments (Richardson et al., 2020).

Individual effects of impact parameters on the frequency spectrum were determined by varying impactor radius (2–30 m), impact velocity (0.1–6.4 kms^{-1}) and target material properties (intact bedrock, fractured bedrock and porous regolith). The corner frequency of the spectrum is found to increase with target bulk density and decrease with impact speed and impactor size. The long period amplitude is found to increase with impactor momentum and target bulk density. Impacts into less porous targets have higher seismic efficiency, however, due to their higher corner frequency the long period amplitude is lower than that of the same impact into a more porous target. Higher frequencies, generated by impacts into denser targets, are also more attenuated at large distances. This implies that impacts into porous targets could be detectable at greater distance than impacts into non-porous targets such as exposed bedrock. However, at those greater distances the attenuation parameters are likely to be different to account for mantle propagation and scattering, and a more complex interior structure of Mars.

Four scaling relationships are developed to allow for scaling of the frequency spectrum relative to the baseline scenario simulated, based on the three impact parameters considered. A simplified attenuation model is used to scale the spectra to larger distances, more appropriate for InSight. A combination of these scaling relationships is used to predict the vertical frequency spectrum for two of the recently detected by Insight impacts — events S0793a and S0986c. The resulting spectra have a range of corner frequencies surrounding the corner frequency measured by InSight, depending on the material properties assumed at the impact location. However, the predicted amplitudes are several orders of magnitude higher than those measured at InSight,

which requires further investigation.

Future studies should explore how these results vary for different impact angles and complex events such as crater clusters. A more realistic Martian interior model should also be implemented to scale the power spectra developed here from source to receiver.

Chapter 6

Conclusions

6.1 Summary of results

The key findings of this work are contained in three chapters 3, 5 and 4. This section provides the reader with a summary of key results of each Chapter and their implications.

6.1.1 Seismic source properties

Chapter 3 placed novel constraints on seismic source properties of small impacts onto Martian regolith. The main parameters investigated were seismic moment, seismic efficiency and source time function. The impactor size and velocity range studied was chosen to be most relevant for InSight - impacts forming craters between 1-30 m. In total, 13 impact scenarios were simulated using iSALE2D. The pressure wave generated during the impact was tracked as it decayed across the simulation mesh. The key findings of this study were:

- The seismic moment was found to be between 10^6–10^{10} Nm and was determined to scale almost linearly with impact momentum in that range.
- The ratio of horizontal to vertical seismic moment tensor components was found to be $\sim$1, implying an almost isotropic P-wave source, for vertical impacts. The ejecta amplifica-

tion factor, S, increased with impact momentum from 1.25–1.6, consistent with previous studies. Higher momentum impacts were therefore more isotropic while more momentum was imparted to the ground.

- Seismic efficiencies, k_s, were found to be $\sim 10^{-6}$, dependent on the target crushing strength and impact velocity. The relatively low seismic efficiency and seismic moment predictions suggest that the detectability of small meteorite impacts on Mars is lower than previously assumed.

- Seismic source time function duration and peak force was measured for a subset of impact scenarios and approximated with a two-parameter Jeffrey's pulse expression. The effects of individual impact parameters on the source time function were investigated. The source duration varied between $\sim 10^{-4}$–10^{-3} s, increasing with impact momentum, impactor size and target porosity. Increasing impact velocity had the opposite effect of decreasing the source duration. The peak force, F_{max}, at the source for impacts in the range of most interest for InSight was determined to be between 10^6–10^{11} N. F_{max} was found to increase with increasing impactor momentum, size and velocity, but decrease with target material porosity. The α parameter in Jeffrey's pulse expression was found to scale best with t_c, the contact and compression timescale of the impact process, resulting in a scaling relationship for the source time function approximation comprised of physical impact parameters.

6.1.2 Impact rate and detectability on Mars

Chapter 4 builds on results of Chapter 3 to further constrain the detectability of small impacts on Mars. The semi-empirical amplitude-distance scaling relationship were derived based on peak P-wave amplitude scaled by impact momentum, for impacts on Earth, Moon and recently discovered impacts on Mars. The momentum based scaling relationships were compared with energy-based detectability estimates. Because of the special shared characteristics of Very High Frequency (VF) events, and the fact that the majority of impacts observed visually and seismically belong to that event family, it is likely that more or all VF events are impact

related. This chapter combined the amplitude-distance and seismic moment-crater diameter scaling relationships to predict a crater size for each VF event recorded by InSight using two methods: one based on peak P-wave amplitudes (Method 1) and one based on seismic moment magnitude (Method 2). The key results of this chapter are:

- The peak P-wave amplitude scaled by impact momentum produces a clear trend with distance where amplitude decreases as $x^{-1.56}$. This approach implies that impacts forming craters smaller than 30 m in diameter are less detectable than pre-landing estimates suggested. Larger impacts on the other hand are more detectable than pre-landing predictions.

- Crater diameters for all VF events resulting from Method 1 were between 3–40 m. The impact rate predicted by Method 1 is approximately 5 times higher than that of Daubar et al. (2014).

- Method 2 predicts an impact rate that is only 3.5 times higher than the most recent observational estimates (Daubar et al., 2014), and is consistent with Hartmann (2005) isochron rates within uncertainty.

- If all VF events are impacts, their rate of detection implies an impact rate that is higher than previously estimated from spacecraft observations of newly formed craters over the last 16 years. This could indicate a recent increase, for example due to asteroid breakup near Mars. Another possible explanation is a systematic error in calculation of the ATF used to scale crater counts from orbital observations.

6.1.3 Frequency content of impact-generated seismic waves

Chapter 5 aimed to constrain the frequency content of displacement seismograms of meteorite impacts. This was achieved by using an asteroid target in iSALE2D simulations, which allowed the simulations to run significantly longer, because a whole body was included in the simulation domain, and boundary reflections formed part of the signal and did not pose a contamination

problem. This is in contrast to the half-space geometry (for example the one used in Chapter 3), where the mesh boundary introduces nonphysical wave reflections, which contaminate the signal. Displacement seismograms were recorded ∼800 m (between 10–200 crater diameters) from impact point for 7 impact scenarios. The power spectrum was found to closely follow a −2-model, where the amplitude for frequencies larger than the corner frequency decreases as f^{-2}. The spectrum was approximated by a two-parameter expression, characterised by low frequency plateau (A_0) and corner frequency (f_c). The response of the frequency spectrum to changes in impactor size, velocity and target material was investigated individually. The key conclusions of this chapter are:

- Corner frequency f_c of the signal decreases with increasing impactor size and velocity, following a power law. Weaker and more porous target materials exhibit lower corner frequency.
- Low-frequency amplitude A_0 was found to scale with impactor momentum, with some sensitivity to target material properties.
- The power spectrum can be scaled to longer distances, over which impacts are more likely to be detected, by applying simple attenuation and geometric spreading model. The corner frequencies predicted for two of the seismically detected impacts are consistent with observations. However, the predicted amplitudes are significantly higher than those observed at InSight. This can be attributed to inclusion of the P, S and surface waves in the simulation spectra.

6.2 Limitations and future work

The results of Chapter 3 contributed to constraining seismic source properties of small impact on Mars, specifically in the context of InSight. It is clear however, that a lot of work remains to be done in order to fully understand the relationships between those seismic properties and the impactor and target properties. All targets simulated in this work were assumed to be uniform, which is unlikely to be true at real impact sites. Future studies should explore the effects of layered targets, for example a porous regolith layer overlaying denser intact bedrock, on seismic moment and efficiency, as well as other seismic parameters. Another possible approach would be to use a vertical porosity gradient, where the density of the target material increases as a function of depth. It should also be noted that gravity was neglected in all simulations in this work, which is an important component of crater formation especially for larger craters, and may also have an effect on the seismic source properties of the impact.

In Chapters 3 and 5 the material properties of the impactor were kept constant, as nominal non-porous basalt of density $2860\,\mathrm{kgm}^{-3}$, which is representative of a rocky meteorite. However, specific composition of meteorites is likely to vary across different cases, with more porous impactors or ones containing ice being less dense. Metal-rich meteorites are likely to be much denser and exhibit very different properties. Whilst the target material is likely to have the most influence over the generation of the seismic wave during impact, because the generation takes place inside the target, the impactor may also play an important role. A further study, investigating the specific dependence of the seismic wave properties, such as seismic moment and efficiency, should be conducted in the future to further our understanding of this process.

Whilst the simulations in this thesis focus on impact scenarios most relevant for the mission, it is important to note that all simulations were performed in two dimensions (axially symmetric, cylindrical geometry). Because of this all scenarios are approximated as vertical impacts, and the effects of impact angle are neglected. Chapter 3 employed a widely adopted convention of taking the vertical component of impact velocity. However, especially for directional quantities, such as seismic moment, and quantities derived from them, such as source sphericity, taking

impact angle into account may yield very different results. Future studies should therefore explore if the results presented in this thesis extend to oblique cases, using three-dimensional simulations. This is particularly relevant for investigations of the largest crater recorded by InSight (event S1094b) and the complex crater cluster formed 85 km from the lander (S0986c), both of which show evidence of a highly oblique impact angle. The unique features of each of the above cratering events, such as the presence of excavated ice in S1094b or the possible multiple fragmentation of S0986c, also provide room for detailed modelling studies focusing on how the seismic properties of those complex events vary from other cases.

As demonstrated in Chapters 3 and 4, the seismic moment recorded at the source location (such as in iSALE simulations) can be very different to the values determined at the receiver. A working hypothesis is that this is due, in large part, to the source depth correction factor introduced in Chapter 4, which dictates that the seismic moment generated at a seismic source is dependent on the seismic wave velocity and density of the material at the seismic moment release depth. In Chapter 4 this correction factor was assumed to be a constant value for all events and its value was calibrated using confirmed impact events. This is a reasonable choice for the small subset of marsquakes considered in this work. However, for other impact scenarios, this correction factor will depend on the specific material properties at the impact site as well as the diameter and depth of the crater, making it difficult to determine for a wide range of impacts. Future studies should aim to investigate whether this correction factor is the true and complete explanation for the discrepancy between modelling results and observations. Moreover, further constraining of this factor for the small set of confirmed impact events, by combining geological knowledge of the area with analysis of the seismic signal and numerical modelling of the specific impact scenarios, is also needed.

Chapter 4 used a subset of seismic events recorded by InSight to derive a novel estimate of the current impact rate on Mars. The specific shared properties of the VF events family made them excellent candidates for impacts. However, it is possible, that there are many more impact-related seismic signals in the seismic catalogue, which have not yet been recognised. This suggests that a further search for impact related seismic signals is needed. An example of a potential dataset would be the Broad Band (BB) events, two of which were already identified

as large, distant impacts (S1094b and S1000a, Posiolova et al., 2022). Because those events are much larger and are thought to be located significantly further away from InSight, they can provide significant constraints on the martian interior structure, especially if the source location and properties are well constrained by an imaged crater. In addition, such events can be used to further calibrate the seismic magnitude scales on Mars. However, as shown throughout this thesis, large and distant craters require additional investigation. Seismic moment derived from observations of those impacts scales differently to smaller and more local impacts (Fig. 4.9), primarily due to a different relationship between impact momentum and crater size. Scaled wave amplitudes also do not follow the same trend as other impact events on Earth, Moon and Mars (Fig. 4.7). This effect could be explained partially by the large differences in wave propagation paths between nearby and distant events. However, this could also suggest that distant impacts follow a different amplitude-distance scaling relationship that that shown in Fig. 4.7, which can perhaps be generalised to other impact scenarios detected at large distances.

An interesting extension to the work presented in Chapter 4 would be to design an orbital imaging campaign, focusing on finding more craters corresponding to the VF events. Because the VF events do not have associated back-azimuth estimates, this would require searching very large areas around InSight. In addition, if a crater was found, a 'before' image may not be available to sufficiently constrain the impact date. However, even if a small number of fresh craters could be associated with VF events, this would provide a further evidence that the whole event family is likely to be impact related.

The work presented in Chapter 5 provided first insight into the dependence of the power spectrum of seismic signals generated by impacts on specific impact properties. However, the range of scenarios considered was limited by their computational expense and time constraints. Because the target size was kept constant in all simulations (1 km wide asteroid), the number of cells in the domain increases with decreasing impactor size. Using the same approach to produce spectra of such smaller impacts, more relevant for InSight, would result in prohibitively large simulation domains, which would need to be tracked for a long time after impact ($\sim$2 s). Whilst more simulations need to be performed in a more comprehensive study, which would focus on smaller and more common impacts, the simulations setup will need to be modified to achieve

this.

The amplitudes predicted for two of the impact events recorded by InSight in Chapter 5, using the scaling relationships derived in this chapter, are several orders of magnitude than those recorded by the lander. This could imply that a more complex attenuation model is required to correctly predict the amplitudes of events on Mars. An alternative approach to this problem is to focus on simulating smaller-scale impacts using iSALE, and combining the resulting elastic seismic wave record to a wave propagation code (such as SPECFEM). The iSALE simulation would need to continue until the generated wave is elastic, in which case a relatively large simulation domain (such as the ones used in Chapter 3) would be needed. At the end of the simulation, the ground motion could be extracted and coupled to the wave propagation software. This would allow for the seismic waves generated in iSALE impact simulations to be propagated across the planet and generate synthetic seismograms which can be compared with real data.

The overwhelming success of the InSight mission shows that more seismology-based space missions are needed in the future. InSight dataset is undoubtedly going to be used and analysed by scientists for the years to come and will form a basis of the future of planetary seismology. The mission clearly showed that seismology is a powerful tool not only for locating impacts which may have otherwise been missed by orbital imagery, but more generally for monitoring impact rates on planetary bodies. Collaborative efforts between the InSight team and the various orbital imaging teams resulted in the first dataset of its kind, containing both images of craters as well as seismic recording of meteorite impacts on Mars. The InSight team also worked with the Mars2020 mission team in efforts to record the landing of Perserverance on Mars. These examples will hopefully lead to more inter-mission collaborations in the future. Impacts have also proven to be extremely valuable as seismic sources for calibrating the distance and back-azimuth estimates for other events, as well as linking crater morphology to the seismic signals properties. The specific impact cases recorded by InSight provide unprecedented insight into the impact process. Now more than ever, there is need for further work to fully understand the process of generation of seismic waves during an impact.

Bibliography

Ackermann, H. D. et al. (1975). "A seismic refraction technique used for subsurface investigations at Meteor Crater, Arizona". In: *Journal of Geophysical Research* 80.5, pp. 765–775.

Ahrens, T. J. and D. M. Cole (1974). *Shock compression and adiabatic release of lunar fines from Apollo 17**. Tech. rep., pp. 2333–2345.

Aki, K and P. G. Richards (2002). *Quantitative Seismology*. University Science Books.

Amsden, A. A. et al. (1980). *SALE: A Simplified ALE computer program for fluid flow at all speeds*. Tech. rep. June. Los Alamos, NM (United States): Los Alamos National Laboratory (LANL), 101p.

Asphaug, E. (2008). "Critical crater diameter and asteroid impact seismology". In: *Meteoritics & Planetary Science* 43.6, pp. 1075–1084.

Banerdt, W. B. and C. T. Russell (2017). "Editorial on: Topical Collection on InSight Mission to Mars". In: *Space Science Reviews* 211.1-4, pp. 1–3.

Banerdt, W. B. et al. (2020). "Initial results from the InSight mission on Mars". In: *Nature Geoscience* 13.3, pp. 183–189.

Benz, W. and E. Asphaug (1999). "Catastrophic Disruptions Revisited". In: *Icarus* 142.1, pp. 5–20.

Böse, M. et al. (2017). "A probabilistic framework for single-station location of seismicity on Earth and Mars". In: *Physics of the Earth and Planetary Interiors* 262, pp. 48–65.

Böse, M. et al. (2021). "Magnitude Scales for Marsquakes Calibrated from InSight Data". In: *Bulletin of the Seismological Society of America* Xx.

Britt, D. T. and S. J. Consolmagno (2003). "Stony meteorite porosities and densities: A review of the data through 2001". In: *Meteoritics and Planetary Science* 38.8, pp. 1161–1180.

Brown, P. et al. (2008). "Analysis of a crater-forming meteorite impact in Peru". In: *Journal of Geophysical Research* 113.E9, E09007.

Brune, J. N. (1970). "Tectonic stress and the spectra of seismic shear waves from earthquakes". In: *Journal of Geophysical Research* 75.26, pp. 4997–5009.

Carroll, M. et al. (1972). "Suggested Modification of the P-α Model for Porous Materials". In: *JAP* 43.2, pp. 759–761.

Chapman, C. R. and W. B. McKinnon (1986). "Cratering of Planetary Satellites". In: *Satellites*, pp. 492–580.

Clinton, J. and F. Euchner (2021). *Mars Seismic Catalogue, InSight Mission.*

Clinton, J. F. et al. (2021). "The Marsquake catalogue from InSight, sols 0–478". In: *Physics of the Earth and Planetary Interiors* 310, p. 106595.

Collins, G. S. et al. (2011). "Improvements to the ϵ-α Porous compaction model for simulating impacts into high-porosity solar system objects". In: *International Journal of Impact Engineering* 38.6, pp. 434–439.

Collins, G. S. et al. (2022). "Meteoroid Fragmentation in the Martian Atmosphere and the Formation of Crater Clusters". In: *Journal of Geophysical Research: Planets* 127.7, e2021JE007149.

Collins, G. S. et al. (2002). "Hydrocode Simulations of Chicxulub Crater Collapse and Peak-Ring Formation". In: *Icarus* 157.1, pp. 24–33.

Collins, G. S. et al. (2004). "Modeling damage and deformation in impact simulations". In: *Meteoritics and Planetary Science* 39.2, pp. 217–231.

Dahmen, N. L. et al. (2021). "Resonances and Lander Modes Observed by InSight on Mars (1–9 Hz)". In: *Bulletin of the Seismological Society of America* 111.6, pp. 2924–2950.

Daubar, I. J. et al. (2013). "The current martian cratering rate". In: *Icarus* 225.1, pp. 506–516.

Daubar, I. J. et al. (2014). "New Dated Impacts on Mars and an Updated Current Cratering Rate". In: *LPICo* 1791, p. 1007.

Daubar, I. J. et al. (2015). "Measurement of the Current Martian Cratering Size Frequency Distribution, Predictions for and Expected Improvements from InSight". In: *Lunar and Planetary Science Conference*, p. 2468.

Daubar, I. J. et al. (2019). "Recently Formed Crater Clusters on Mars". In: *Journal of Geophysical Research: Planets* 124.4, pp. 958–969.

Daubar, I. J. et al. (2020). "A New Crater Near InSight: Implications for Seismic Impact Detectability on Mars". In: *Journal of Geophysical Research: Planets* 125.8.

Daubar, I. J. et al. (2022). "New Craters on Mars: An Updated Catalog". In: *Journal of Geophysical Research: Planets* 127.7, e2021JE007145.

Daubar, I. et al. (2018). "Impact-Seismic Investigations of the InSight Mission". In: *Space Science Reviews* 214.8, pp. 1–91.

Driel, M. van et al. (2021). "High-Frequency Seismic Events on Mars Observed by InSight". In: *Journal of Geophysical Research: Planets* 126.2, e2020JE006670.

Durda, D. D. et al. (1998). "Collisional Models and Scaling Laws: A New Interpretation of the Shape of the Main-Belt Asteroid Size Distribution". In: *Icarus* 135.2, pp. 431–440.

Elbeshausen, D. et al. (2009). "Scaling of oblique impacts in frictional targets: Implications for crater size and formation mechanisms". In: *Icarus* 204.2, pp. 716–731.

Fernando, B. et al. (2021a). "Listening for the Landing: Seismic Detections of Perseverance's Arrival at Mars With InSight". In: *Earth and Space Science* 8.4, e2020EA001585.

Fernando, B. et al. (2021b). "Seismic constraints from a Mars impact experiment using InSight and Perseverance". In: *Nature Astronomy 2021*, pp. 1–6.

Garcia, R. F. et al. (2022). "Newly formed craters on Mars located using seismic and acoustic wave data from InSight". In: *Nature Geoscience 2022* 10.11, pp. 1–7.

Giardini, D. et al. (2020). "The seismicity of Mars". In: *Nature Geoscience* 13.3, pp. 205–212.

Golombek, M. et al. (2017). "Selection of the InSight Landing Site". In: *Space Science Reviews* 211.1-4, pp. 5–95.

Golombek, M. et al. (2020). "Geology of the InSight landing site on Mars". In: *Nature Communications* 11.1.

Gudkova, T. V. et al. (2011). "Large impacts detected by the Apollo seismometers: Impactor mass and source cutoff frequency estimations". In: *Icarus* 211.2, pp. 1049–1065.

Gudkova, T. et al. (2015). "Impact cutoff frequency – momentum scaling law inverted from Apollo seismic data". In: *Earth and Planetary Science Letters* 427, pp. 57–65.

Güldemeister, N. and K. Wünnemann (2017). "Quantitative analysis of impact-induced seismic signals by numerical modeling". In: *Icarus* 296, pp. 15–27.

Hanks, T. C. and H. Kanamori (1979). "A moment magnitude scale". In: *Journal of Geophysical Research: Solid Earth* 84.B5, pp. 2348–2350.

Hartmann, W. K. (1964). "On the Distribution of Lunar Crater Diameters". In: *CoLPL* 2, pp. 197–204.

Hartmann, W. K. (1965). "Terrestrial and lunar flux of large meteorites in the last two billion years". In: *Icarus* 4.2, pp. 157–165.

Hartmann, W. K. (1966). "Martian Cratering". In: *Icarus* 5.1-6, pp. 565–576.

Hartmann, W. K. (1999). "Martian cratering VI: Crater count isochrons and evidence for recent volcanism from Mars Global Surveyor". In: *Meteoritics and Planetary Science* 34.2, pp. 167–177.

Hartmann, W. K. (2005). "Martian cratering 8: Isochron refinement and the chronology of Mars". In: *Icarus* 174.2 SPEC. ISS. Pp. 294–320.

Haskell, N. A. (1967). "Analytic approximation for the elastic radiation from a contained underground explosion". In: *Journal of Geophysical Research* 72.10, pp. 2583–2587.

Helmberger, D. V. and D. M. Hadley (1981). "Seismic source functions and attenuation from local and teleseismic observations of the NTS events jorum and handley". In: *Bulletin of the Seismological Society of America* 71.1, pp. 51–67.

Herrmann, W. (1969). "Constitutive equation for the dynamic compaction of ductile porous materials". In: *Journal of Applied Physics* 40.6, pp. 2490–2499.

Holsapple, K. A. (1993). "The scaling of impact processes in planetary sciences". In: *Annual Review of Earth & Planetary Sciences* 21.1, pp. 333–373.

Holsapple, K. A. and R. M. Schmidt (1982). "On the scaling of crater dimensions: 2. Impact processes". In: *Journal of Geophysical Research: Solid Earth* 87.B3, pp. 1849–1870.

Holsapple, K. A. (2008). "Porous material models for impact studies". In: *Lunar and Planetary Science 39th*, abstract #2257.

Housen, K. R. et al. (2018). "Impacts into porous asteroids". In: *Icarus* 300, pp. 72–96.

Ivanov, B. A. et al. (1997). "Implementation of dynamic strength models into 2D hydrocodes: Applications for atmospheric breakup and impact cratering". In: *International Journal of Impact Engineering* 20.1-5, pp. 411–430.

Kenkmann, T. et al. (2009). "The Carancas meteorite impact crater, Peru: Geologic surveying and modeling of crater formation and atmospheric passage". In: *Meteoritics & Planetary Science* 44.7, pp. 985–1000.

Khan, A. et al. (2021). "Upper mantle structure of Mars from InSight seismic data". In: *Science* 373.6553, pp. 434–438.

Knapmeyer-Endrun, B. et al. (2021). "Thickness and structure of the martian crust from InSight seismic data". In: *Science* 373.6553, pp. 438–443.

Koenig, B. et al. (1977). "Recent Lunar Cratering: Absolute Ages of Kepler, Aristarchus, TYCHO". In: *LPI* 8, p. 555.

Latham, G. et al. (1970a). "Seismic data from man-made impacts on the moon". In: *Science* 170.3958, pp. 620–626.

Latham, G. V. et al. (1970b). "Missile impacts as sources of seismic energy on the moon". In: *Science* 168.3928, pp. 242–245.

Le Feuvre, M. and M. A. Wieczorek (2011). "Nonuniform cratering of the Moon and a revised crater chronology of the inner Solar System". In: *Icarus* 214.1, pp. 1–20.

Le Pichon, A. et al. (2008). "Evidence for a meteoritic origin of the September 15, 2007, Carancas crater". In: *Meteoritics & Planetary Science* 43.11, pp. 1797–1809.

Lognonné, P. and C. L. Johnson (2015). "Planetary Seismology". In: *Treatise on Geophysics: Second Edition*. Vol. 10. Elsevier Inc., pp. 65–120.

Lognonné, P. et al. (2019). "SEIS: Insight's Seismic Experiment for Internal Structure of Mars". In: *Space Science Reviews* 215.1, p. 12.

Lognonné, P. et al. (2020). "Constraints on the shallow elastic and anelastic structure of Mars from InSight seismic data". In: *Nature Geoscience* 13.3, pp. 213–220.

Lognonné, P. et al. (2009). "Moon meteoritic seismic hum: Steady state prediction". In: *Journal of Geophysical Research E: Planets* 114.12, E12003.

Lundborg, N. (1968). "Strength of rock-like materials". In: *International Journal of Rock Mechanics and Mining Sciences and* 5.5, pp. 427–454.

Luo, H. et al. (2011). "Effect of Mass Density on the Compressive Behavior of Dry Sand Under Confinement at High Strain Rates". In: *Experimental Mechanics* 51.9, pp. 1499–1510.

Malin, M. C. et al. (2006). "Present-day impact cratering rate and contemporary gully activity on Mars". In: *Science (New York, N.Y.)* 314.5805, pp. 1573–1577.

Malin, M. C. et al. (2007). "Context Camera Investigation on board the Mars Reconnaissance Orbiter". In: *Journal of Geophysical Research: Planets* 112.E5, pp. 5–9.

McEwen, A. S. et al. (2007). "Mars Reconnaissance Orbiter's High Resolution Imaging Science Experiment (HiRISE)". In: *Journal of Geophysical Research: Planets* 112.E5, pp. 5–7.

McFadden, L. (2005). "Mitigation of Hazardous Comets and Asteroids". In: *Eos, Transactions American Geophysical Union* 86.21, p. 205.

McGarr, A. et al. (1969). "Meteoroid impacts as sources of seismicity on the moon". In: *J Geophys Res* 74.25, pp. 5981–5994.

McMullan, S. and G. S. Collins (2019). "Uncertainty quantification in continuous fragmentation airburst models". In: *Icarus* 327, pp. 19–35.

Melosh, H. J. (1989). *Impact cratering: a geologic process.*

Melosh, H. J. et al. (1992). "Dynamic fragmentation in impacts: hydrocode simulation of laboratory impacts". In: *Journal of Geophysical Research* 97.E9, pp. 14735–14759.

Morgan, P. et al. (2018). "A Pre-Landing Assessment of Regolith Properties at the InSight Landing Site". In: *Space Science Reviews* 214.6, p. 104.

Müller, G. (1973). "Seismic moment and long-period radiation of underground nuclear explosions". In: *Bulletin of the Seismological Society of America* 63.3, pp. 847–857.

Neukum, G. et al. (2001). "Cratering Records in the Inner Solar System in Relation to the Lunar Reference System". In: *Space Science Reviews 2001 96:1* 96.1, pp. 55–86.

Patton, H. J. and W. R. Walter (1993). "Regional moment:magnitude relations for earthquakes and explosions". In: *Geophysical Research Letters* 20.4, pp. 277–280.

Popova, O. et al. (2003). "Bolides in the present and past martian atmosphere and effects on cratering processes ". In: *Meteoritics & Planetary Science* 38, pp. 905–925.

Posiolova, L. V. et al. (2022). “Largest recent impact craters on Mars: Orbital imaging and surface seismic co-investigation”. In: *Science (New York, N.Y.)* 378.6618, pp. 412–417.

Prieto, G. A. et al. (2004). “Earthquake source scaling and self-similarity estimation from stacking P and S spectra”. In: *Journal of Geophysical Research: Solid Earth* 109.8.

Prieur, N. C. et al. (2017). “The effect of target properties on transient crater scaling for simple craters”. In: *Journal of Geophysical Research: Planets* 122.8, pp. 1704–1726.

Raducan, S. D. et al. (2019). “The role of asteroid strength, porosity and internal friction in impact momentum transfer”. In: *Icarus* 329, pp. 282–295.

Rajšić, A. et al. (2021). “Seismic Efficiency for Simple Crater Formation in the Martian Top Crust Analog”. In: *Journal of Geophysical Research: Planets* 126.2, e2020JE006662.

Richardson, J. E. and S. Kedar (2013). “An Experimental Investigation of the Seismic Signal Produced by Hypervelocity Impacts”. In: *44th Lunar and Planetary Science Conference, held March 18-22, 2013 in The Woodlands, Texas. LPI Contribution No. 1719, p.2863.* Vol. 44, p. 2863.

Richardson, J. E. et al. (2020). “Impact-produced seismic shaking and regolith growth on asteroids 433 Eros, 2867 Šteins, and 25143 Itokawa”. In: *Icarus* 347, p. 113811.

Rinehart, J. (1960). *On fractures caused by explosions and impacts.* Vol. 4. 4, pp. 331–332.

Schmerr, N. C. et al. (2019). “The Seismic Signatures of Recently Formed Impact Craters on Mars”. In: *Journal of Geophysical Research: Planets* 124.11, pp. 3063–3081.

Schultz, P. H. and D. E. Gault (1975). “Seismic effects from major basin formations on the moon and mercury”. In: *The Moon* 12.2, pp. 159–177.

Shishkin, N. I. (2007). “Seismic efficiency of a contact explosion and a high-velocity impact”. In: *Journal of Applied Mechanics and Technical Physics* 48.2, pp. 145–152.

Sidiropoulos, P. and J. P. Muller (2015). “On the status of orbital high-resolution repeat imaging of Mars for the observation of dynamic surface processes”. In: *Planetary and Space Science* 117, pp. 207–222.

Smith, S. K. et al. (1999). “The utilization of RADARSAT-1 imagery for the characterization of terrestrial impact landforms”. In: *Canadian Journal of Remote Sensing* 25.3, pp. 218–228.

Stähler, S. C. et al. (2021). "Seismic detection of the martian core". In: *Science* 373.6553, pp. 443–448.

Stöffler, D. and G. Ryder (2001). "Stratigraphy and Isotope Ages of Lunar Geologic Units: Chronological Standard for the Inner Solar System". In: *Space Science Reviews 2001 96:1* 96.1, pp. 9–54.

Tancredi, G. et al. (2009). "A meteorite crater on Earth formed on September 15, 2007: The Carancas hypervelocity impact". In: *Meteoritics & Planetary Science* 44.12, pp. 1967–1984.

Teanby, N. A. (2015). "Predicted detection rates of regional-scale meteorite impacts on Mars with the InSight short-period seismometer". In: *Icarus* 256, pp. 49–62.

Teanby, N. A. and J. Wookey (2011). "Seismic detection of meteorite impacts on Mars". In: *Physics of the Earth and Planetary Interiors* 186.1-2, pp. 70–80.

Thiel, M. van (1977). *Compedium of shock wave data*. Livermore: Lawrence Livermore Laboratory Report UCRL-50108, pp. 719–729.

Tillotson, J. H. (1962). "Metallic equations of state for hypervelocity impacts". In: *Report No. GA-3216, General Atomic, San Diego, CA*, p. 43.

Wagstaff, K. L. et al. (2022). "Using machine learning to reduce observational biases when detecting new impacts on Mars". In: *Icarus* 386, p. 115146.

Walker, J. D. (2003). "Loading sources for seismological investigations of asteroids and comets". In: *International Journal of Impact Engineering* 29.1-10, pp. 757–769.

Warner, N. H. et al. (2017). "Near Surface Stratigraphy and Regolith Production in Southwestern Elysium Planitia, Mars: Implications for Hesperian-Amazonian Terrains and the InSight Lander Mission". In: *Space Science Reviews* 211.1-4, pp. 147–190.

Werth, G. C. and R. F. Herbst (1963). "Comparison of amplitudes of seismic waves from nuclear explosions in four mediums". In: *Journal of Geophysical Research* 68.5, pp. 1463–1475.

Williams, J. P. et al. (2014). "The production of small primary craters on Mars and the Moon". In: *Icarus* 235, pp. 23–36.

Wójcicka, N. et al. (2020). "The Seismic Moment and Seismic Efficiency of Small Impacts on Mars". In: *Journal of Geophysical Research: Planets* 125.10.

Wójcicka, N. et al. (2021). "Seismic Source Time Function and Frequency Content of Impact-Generated Seismic Waves". In: *Lunar and Planetary Science Conference*. 2548, p. 2134.

Wójcicka, N. et al. (2022). "Frequency Content of Impact-generated Seismic Waves". In: *53rd Lunar and Planetary Science Conference*.

Wünnemann, K. et al. (2002). "Numerical modeling of impact-induced modifications of the deep-sea floor". In: *DSRII* 49.6, pp. 969–981.

Wünnemann, K. et al. (2003). "Numerical modelling of the impact crater depth-diameter dependence in an acoustically fluidized target". In: *P&SS* 51.13, pp. 831–845.

Wünnemann, K. et al. (2006). "A strain-based porosity model for use in hydrocode simulations of impacts and implications for transient crater growth in porous targets". In: *Icarus* 180.2, pp. 514–527.

Wünnemann, K. et al. (2016). "Impacts into quartz sand: Crater formation, shock metamorphism, and ejecta distribution in laboratory experiments and numerical models". In: *Meteoritics and Planetary Science* 51.10, pp. 1762–1794.

Yasui, M. et al. (2015). "Experimental study on impact-induced seismic wave propagation through granular materials". In: *Icarus* 260, pp. 320–331.

Young, J (1940). "A statistical investigation of diameter and distribution of lunar craters". In: *J. Brit. Astron. Assoc* 50.9, p. 309326.